# Ultrafast Dynamics from Quantum to Classical Regime

**Hui Li**

München 2016

# Ultrafast Dynamics from Quantum to Classical Regime

**Hui Li**

Dissertation
an der Fakultät für Physik
der Ludwig–Maximilians–Universität
München

vorgelegt von
Hui Li
aus Tianjin, China

München, den 4. Mai 2016

# Zusammenfassung

Die vorliegende Arbeit befasst sich mit der Wechselwirkung zwischen Wellenform-kontrollie -rten ultrakurzen Laserpulsen und verschiedene Molekülsystemen, von einfachen zweiatomigen Molekülen über Kohlenwasserstoffe und $C_{60}$-Fullerene bis hin zu nano-Clustern aus Silber. Mit Hilfe der phasenaufgelösten Einzelschuss Velocity-Map-Imaging-Methode kann die Winkelverteilung der ionischen Fragmente und Elektronen aufgelöst werden. Verschiedenste elektronische und molekulare Dynamiken können hierbei manipuliert werden, indem man zum Beispiel die Phase zwischen Träger und Einhüllenden (CEP), die Intensität und die Polarisation der ultrakurzen Laserpulse kontrolliert.

Vor allem werden die dissoziative Ionisation im molekularen Prototypsystem Deuterium $D_2$ und zweiatomigen Mehrelektronensystem DCl auf eine Abhängigkeiten von der CEP und der Laserintensität untersucht. In $D_2$ wird der Populationsmechanismus des hochangeregten $3\sigma$ Zustandes durch die Analyse der Asymmetrie in der Emission von $D^+$-Ionen ermittelt. Dabei stellt sich heraus, dass bei geringen Intensitäten (bis zu $2.0 \times 10^{14}$ W $cm^{-2}$) auf die Rekollisionsanregung eine Laserfeldanregung erfolgt und zu einer Population des $3\sigma$ Zustandes führen kann. Die direkte Anregung durch Elektronenrekollision ist vor allem bei hohen Intensitäten wichtig. Eine maximale Asymmetrie von ungefähr 44% wird bei Intensitäten um $1.3 \times 10^{14}$ W $cm^{-2}$ und einer Pulsdauer von 4 fs erreicht, was auf eine starke Kontrolle der Elektronenlokalisierung durch die CEP hinweist. Die dissoziative Ionisation von DCl wird für Intensitäten zwischen 1.3 - $3.1 \times 10^{14}$ W $cm^{-2}$ untersucht, wobei die $D^+$-Ionen mit Energien über 15 eV verstärkt bei hohen Intensitäten detektiert werden. Durch den Vergleich mit quantendynamischen Simulationen können wir die hohen kinetischen Energien auf Doppelionisation durch Elektronenrekollision zurückführen, welche eine starke CEP-Abhängigkeit aufweist. Neben der Elektronenlokalisation können auch molekulare Strukturen rearrangiert werden durch die CEP-kontrollierten Laserpulse. So wird zum Beispiel in Propadien und Toluol eine sub-Zyklus Kontrolle der Protonmigration demonstriert. Die quantendynamischen Berechnungen in Propadien zeigen, dass eine Kontrolle der Protonenmigration durch eine Überlagerung von verschiedenen Vibrationsmoden möglich wird. Wenn wir zu noch komplexeren Systemen gehen, wie zum Beispiel Fullerene, dann wird deutlich, dass eine kollektive Elektronenbewegung immer wichtiger wird, welche mit der CEP und der Polarisation variiert werden kann. Die quantendynamischen Berechnungen zeigen, dass der Asymmetrieparameter der Elektronenemission von $C_{60}$ die transiente Lokalisierung des kohärenten elektronischen Wellenpaketes zum Zeit-

punkt der Ionisation reflektieren kann. Andererseits kann in $C_{60}$ die Elektronenemission mit hoher kinetischer Energie durch eine zirkulare Polarisation der ultrakurzen Laserpulse erzeugt werden, welche dominiert wird durch eine mehrfache Kollision der Elektronen mit der $C_{60}$ Schale. Damit bildet diese Untersuchung eine Grundlage für die kollektive Elektronenbewegung in anderen komplexen Systemen. Für nano-Cluster aus Silberatomen wird die Winkelverteilung der Elektronenemission untersucht mithilfe zweier Laserpulse, wobei eine transiente resonante Plasmonenanregung beobachtet wird. Die Oszillation der Asymmetrie für geringe Elektronenenergien zeigt eine klare Abhängigkeit des Phasenversatzes von dem Zeitabstand zwischen beiden Pulsen. Diese Elektronen, welche ein charakteristisches spektrales Signal aufweisen, beinhalten vermutlich einen Beitrag vom korrelierten Elektronen Zerfallsprozess, welcher zwei Elektronen aus den Rydberg-Zuständen involviert.

Diese Arbeit trägt zur CEP-Kontrolle in verschiedensten Prozessen bei und ebnet dabei den Weg zu komplexen Systemen. Die Theorie reproduziert unsere Ergebnisse sehr gut für kleine Systeme, wohingegen komplexe Systeme noch immer eine Herausforderung darstellen.

# Abstract

This thesis presents work on the interaction of waveform controlled few-cycle pulses with various systems, from simple diatomic molecules through hydrocarbons and $C_{60}$ fullerene, to nano-sized silver clusters. By employing the single-shot phase-tagged velocity-map imaging (VMI) technique, the angular distributions of ionic fragmentations and electrons can be obtained. Various electronic and molecular dynamics can be manipulated by controlling, e.g. carrier envelope phase (CEP), laser intensity, and polarization of few-cycle pulses.

The dissociative ionization in the prototype molecular system $D_2$ and multi-electron diatomic system DCl are investigated as a function of CEP and laser intensity. In $D_2$, the population mechanism of highly excited $3\sigma$ state is identified by the analysis of the asymmetry in the emission of $D^+$ ions. We find that at low intensities (up to about $2.0\times10^{14}$ W $cm^{-2}$), recollisional excitation followed by laser-field excitation can lead to population of the $3\sigma$ states. Direct excitation by electron recollision plays a role at higher laser intensities. The maximum asymmetry of about 44% is obtained for the recollisional channel at an intensity of around $1.3\times10^{14}$ W $cm^{-2}$ for a 4 fs pulse which indicates strong CEP-control on the electron localization. The dissociative ionization of DCl in 4 fs laser fields is studied for an intensity range of $(1.3\text{-}3.1)\times10^{14}$ W $cm^{-2}$. $D^+$ ions with kinetic energies above 15 eV are obtained for higher laser intensities. By comparison to quantum dynamical simulations we identify the high kinetic energy signal to originate from double ionization induced by rescattered electrons, exhibiting a characteristic CEP-dependence. Besides electron localization, CEP-controlled few-cycle pulses can also manipulate the rearrangement of molecular structures. Sub-cycle control of proton migration is demonstrated in allene and toluene. Quantum dynamical calculations performed on allene show that a superpostion of vibrational modes can be created by waveform controlled few-cycle laser fields, which will result in a directionality of the hydrogen migration. As we move on to ever more complex molecular systems such as fullerenes, collective electron motion becomes important which can be controlled by tailoring the CEP and polarization. Quantum dynamical calculations show that the asymmetry parameter of electron emission from $C_{60}$ can reflect the transient localization of the coherent electronic wave packet at the time of ionization. On the other hand, electron emission with high kinetic energy can be obtained in $C_{60}$ with circularly polarized few-cycle pulses, which is dominated by multiple small-angle recolllision with the $C_{60}$ shell. This provides a solid example for the collective motion of electrons in other complex systems. For silver nano-clusters, the angular distribution of electron emission is

studied in dual-pulse laser fields and transient resonant plasmon excitation is observed at an optimal delay. The asymmetry oscillations show clear delay-dependent phase offsets for the low energy electron emissions. These electrons, which exhibit characteristic spectral features, may have a contribution from a correlated electron decay process involving two Rydberg state electrons.

The work in this thesis advanced the CEP-control on various processes towards complex systems. Theory for small systems is capable of reproducing the results. However, this is still a challenge for the more complex systems.

# Contents

# List of Figures

# Chapter 1

# Introduction

Control of ultrafast electronics and molecular dynamics has entered an exciting era with the development of intense ultrashort laser technology. The characteristic time scale for the motion of atomic nuclei in a molecule is tens to hundreds of femtoseconds, which is determined by the milli-electronvolt (meV) energy spacing of vibrational energy levels in molecules. Molecular structure rearrangements in this time scale have been explored using femtosecond laser pulses [1]. The motion of electrons on atomic scales occurs in sub-femtoseconds. Shorter temporal resolution is required for the investigation of electronic dynamics. With the development of laser technologies came the attosecond era at the beginning of 21st century. Attosecond pulse trains (APT) [2] as well as single attosecond pulses (SAP) [3, 4] can be generated from high-order harmonic generation (HHG). This gives rise to a new research field called 'attosecond science' which permits to watch the electrons move in real-time. Another approach to investigate laser-driven ultrafast dynamics with sub-femtosecond resolution is to alter the carrier envelope phase (CEP) of few-cycle pulses. An electric field can be expressed as $E(t) = E_0(t)\cos(\omega t + \varphi)$, where $E_0(t)$ is the envelope function, $\omega$ is the angular frequency of the driving field, and $\varphi$ is the CEP. For decreasing pulse duration the CEP plays an increasing role in the optical waveform. For few-cycle pulses, control over the CEP provides a tool to manipulate the force acting on the electrons with attosecond precision. The pulse durations correspond to the time scale of electron dynamics and the nuclei can be considered frozen. Since the first experimental work on manipulating electron localization in the dissociative ionization of $D_2$ in intense few-cycle laser fields [5], the CEP-dependence of the ultrafast dynamics has been widely studied using CEP-stabilized few-cycle near-infrared (NIR) [6, 7, 8, 9] and mid-infrared (mIR) pulses [10]. Recently, the CEP-tagging technique [11, 12] provided higher signal-to-noise ratio and less experimental complexity, and overcomes the bottleneck for measuring low probability processes with long term measuring stability [13]. Sub-cycle control can also be achieved with two-color synthesized femtosecond laser pulses [14, 15, 16], where two optical fields with different frequencies are synchronized in a controllable way, such that by adjusting the relative phase between the two frequency components, the resulting waveform can be well modified. Attosecond precision can also be reached with angular streaking with circular polarized pulses [17, 18]. With all these fascinating techniques and well-developed

theoretical models, ultrafast dynamics of electrons and nuclei have been widely explored. The ultimate goal is to observe and control the electron motion on atomic scales in real time, which requires a large amount of research work in various atomic, molecular and solid systems. As we move on from atoms to simple molecules, the molecular structure starts to play a role in the interaction with laser fields. Then people may ask, what will happen if molecules with more complexity are being exposed in a laser field? And how about for even larger targets such as nano-particles and solids? On the other hand, the recollision picture which leads to HHG has been understood in terms of the classical three step model [19] or simple man's model [20] qualitatively. For semi-quantitative calculations, strong-field approximation (SFA) theory [21] and some extension models have been introduced [22, 23] which applies for ionization of atoms and solids in intense laser fields. Quantitatively, numerical solution of the time-dependent Schrödinger equation (TDSE) is required. However, TDSE calculations are time-consuming and accurate results are difficult to obtain except for simple atoms and molecules within the single-active-electron (SAE) approximation. Simplified methods such as the time-dependent density functional theory (TDDFT) and time-dependent Hartree-Fock (TDHF) theory have been developed [24, 25]. The experimental data are usually obtained with a focusing laser beam, therefore the volume averaging effect has to be considered in the theoretical model. To generate theoretical results comparable to the experimental data requires calculations for a large number of laser intensities, which makes the simulation work impractical. TDDFT calculations which take the volume averaging into account became available only recently [26]. More efforts are needed to improve the accuracy of the theoretical models. This can be benefited by comparison to various experimental observations. To help solving these problems, we explored the ultrafast dynamics in several systems under few-cycle laser pulses. We first consider the simplest molecule and then move towards ever more complex systems, from molecular hydrogen to multi-electron diatomic molecule DCl, through hydrocarbons (e.g. allene and toluene) and $C_{60}$ fullerene, to finally a nano-system (silver clusters).

## 1.1 Theoretical background

Strong field physics mainly studies the interaction of intense lasers and matter. In 1964, L. V. Keldysh published an article named 'Ionization in the field of a strong electromagnetic wave' [22, 29]. The theoretical model in this pioneering paper has laid down the foundation for the whole field of intense laser atom interaction. A lot of effects that have been discovered in this field can be interpreted by the Keldysh theory, or within its modifications. However, the significance of this Keldysh paper has only been recognized by people several decades after its publication, when intense ultrashort laser pulses become available. When an atom interacts with a strong field, the bound electron can be ionized by absorbing multiple photons (multi-photon ionization [30] and above threshold ionization (ATI) [31]), or can be tunneling ionized [32, 33]. Strong field ionization mechanisms can be characterized
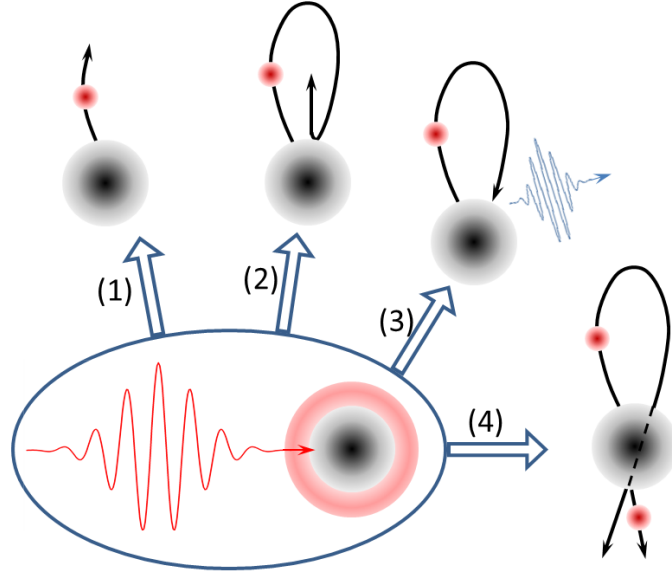
Figure 1.1: Possible consequences of intense laser-atom interaction. When an atom irradiated by a linearly polarized ultrashort laser pulse, the electron can be directly ionized (1) or return to the parental core and recollide (2-4). (2) Under elastic recollision, an energetic electron can be generated. (3) Or the electron can experience inelastic recollision with the parental core and emit an XUV photon. (4) It is also possible that the rescattered electron kicks off a subsequent electron (non-sequential double ionization).

quantitatively by the Keldysh parameter which is given as

$$\gamma = \sqrt{\frac{I_p}{2U_p}} \tag{1.1}$$

where $I_p$ is the ionization potential and $U_p$ is the ponderomotive energy, which is the cycle averaged energy of an electron in an oscillating optical field ($U_p = I/(4\omega^2)$ in atomic units). Multi-photon ionization dominates for $\gamma \gg 1$, while for $\gamma < 1$ tunneling ionization dominates. For a regime with $\gamma \approx 1$ both processes occur.

After being ionized, the subsequent possibilities for the freed electron are shown in Fig. 1.1. The electron can move away from the ionic core (Fig. 1.1, Process (1)), or can be driven back by the external field and recollide with the parent ion. Energetic electron emission can occure under elastic rescattering (Fig. 1.1, Process (2)). Or the returning electron can be inelastically recollide with the core and generate energetic photons with higher-order frequencies (HHG) (Fig. 1.1, Process (3)). Or another electron can be detached upon collision which is called non-sequential double ionization (NSDI) [34] (Fig. 1.1, Process (4)). Among all these possibilities, the mechanism that can generate attosecond pulses is HHG (Process (3)) which can be illustrated nicely by the 3-step model [19], as shown in Fig. 1.2 (a-d). Step 1: Ionization of an electron; Step 2: Movement of the freed
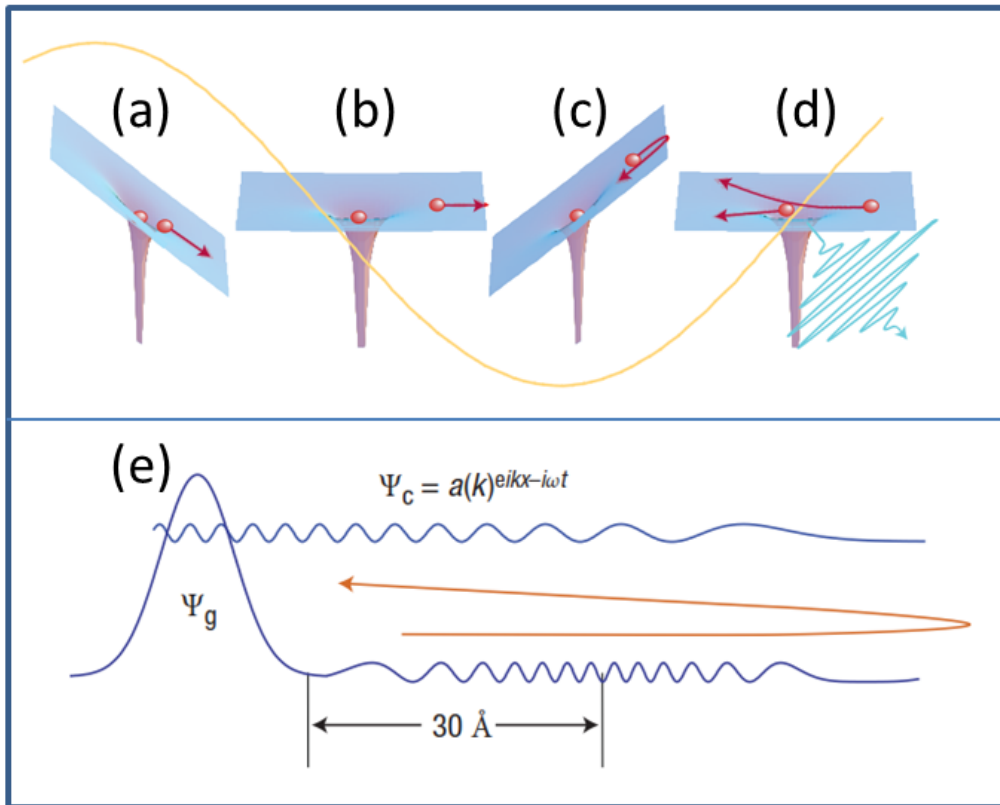
Figure 1.2: High harmonic generation (HHG) from classical and quantum perspectives. Classically, an intense laser pulse can extract an electron from an atom (a). The electron moves away from the atom (b) and is driven back towards the core in the external field (c). Then this electron can recollide with the parental ion inelastically and an energetic optical pulse can be emitted (d). (e) Quantum mechanically, ionization splits the electron wavefunction, one part being driven by the external field which can come back and interfere with the other fraction of the wavefunction. (Taken from Ref. [27])

electron in the external electric field; Step 3: Recollision with the ionic core and emitting an attosecond photon burst with high energy. From a quantum mechanical perspective, as shown in Fig. 1.2 (e), ionization splits the electron wavefunction. One portion stays in the original orbital, while the other part moves in the continuum which can be driven by the external electric field and return towards the core. When the two portions overlap, interference can transfer the kinetic energy, amplitude and phase from the recollision electron to the photon [27]. Generally, most of the key features of HHG can be calculated by the classical model. For instance, the yield of plateau electrons, the cutoff energy, the yield of electrons from direct ionization and recollision can be obtained. However, e.g. fine structures in the electron spectra from interference between two quantum states can only be obtained by solving the TDSE in a quantum model.
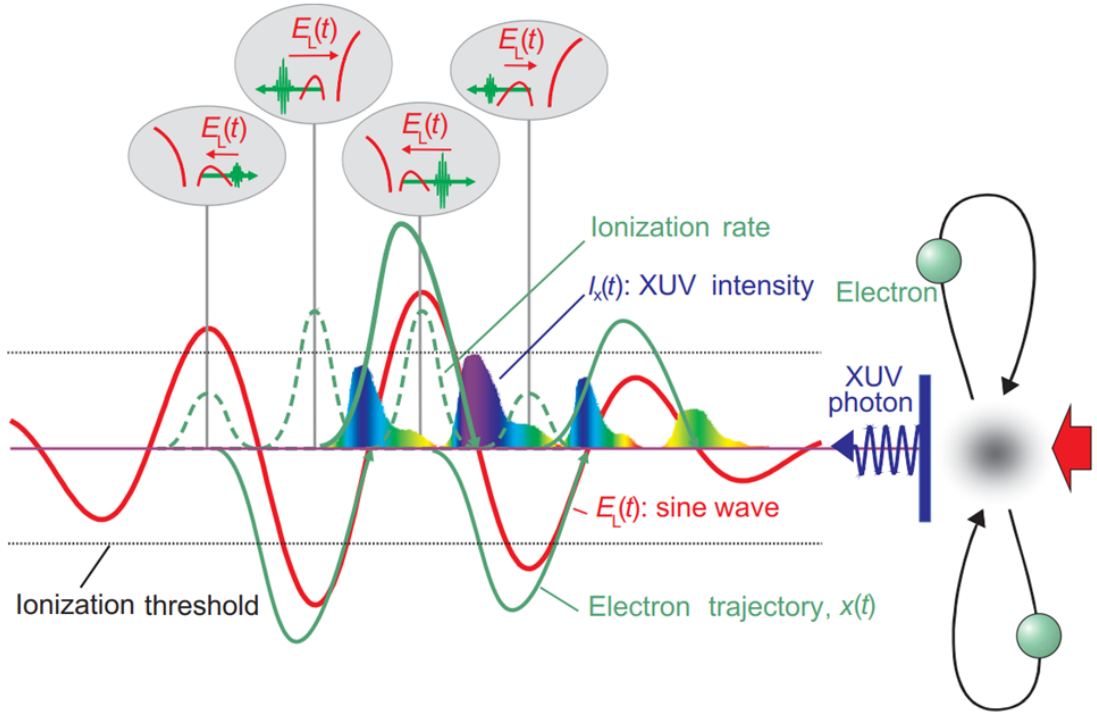
Figure 1.3: Electron trajectories (green solid curves) with the maximum kinetic energy in a 2-cycle laser field (red curve). The green dashed curves show the ionization rate. (Taken from Ref. [28])

**Three step model**

In this semiclassical model, the ionization rate is estimated from the instantaneous electric field strength derived by the Ammosov-Delone-Krainov (ADK) theory [35] which has also been adapted for molecules (the molecular orbital (MO)-ADK model) [36]. The electron is ionized and appears with zero initial velocity. The subsequent dynamics can be described by Newton's equation of motion.

The electric field of a few-cycle laser pulse can be written as

$$E(t) = E_0 f(t) \cos(\omega t + \varphi). \tag{1.2}$$

Here $E_0$ is the amplitude, $f(t)$ is the envelope, $\omega$ is the angular frequency of the driving electric field, $\varphi$ is the CEP. The relationship between electric field $E(t)$ and vector potential $A(t)$ is $E(t) = -dA(t)/dt$. Therefore the vector potential can be derived as

$$A(t) \approx -(E_0/\omega)f(t)\sin(\omega t + \varphi). \tag{1.3}$$

The equation of motion of the electron can be described as

$$\ddot{x}(t) = -E(t). \tag{1.4}$$

Then the electron velocity can be obtained by integrating Eq. 1.4.

$$\dot{x}(t) = v(t) = v(t_0) + A(t) - A(t_0). \tag{1.5}$$

In the tunneling model, we assume the electron is 'born' with zero velocity, therefore $v(t_0) = 0$. The electron final velocity is only related to the vector potential at the instants of ionization and recollision

$$v(t) = A(t) - A(t_0) \approx (E_0/\omega)f(t_0)\sin(\omega t_0 + \varphi) - (E_0/\omega)f(t)\sin(\omega t + \varphi). \tag{1.6}$$

Further integration yields the electron trajectory

$$x(t) \approx \quad x_0 + (E_0/\omega^2)f(t)\cos(\omega t + \varphi) - f(t_0)\cos(\omega t_0 + \varphi)$$
$$+ (E_0/\omega)f(t_0)\sin(\omega t_0 + \varphi)(t - t_0). \tag{1.7}$$

Fig. 1.3 shows an example with electron trajectories with maximum kinetic energy. These electrons are born at about $T_{osc}/20$ following the peak of the electric field and recolliding at about $2/3T_{osc}$ [27], where $T_{osc}$ represents the oscillating period of the driving field ($T_{osc} \approx 2.67$ fs for a wavelength of 800 nm). The ionization rate is also sketched in the figure which is exponentially dependent on the electric field strength. From the fact that the electron trajectories can be determined by the vector potential at the birth and rescattering times, the whole process can be manipulated at will if the waveform of the optical field is under control.

Since tunnel ionization depends on the electric field strength in a strongly nonlinear way, control over the optical waveform has opened the opportunity to manipulate ionization with a precision of hundreds of attoseconds. The electrons born in this narrow time slot are driven by the laser field, which in principle can be tailored at will. Adjusting the waveform is equivalent to changing the force exerted on the electron. On the other hand, steering the reaction of a molecule to a particular structure is the ultimate goal of photochemistry, which can be realized by steering electronic dynamics.

## 1.2   Organization of the thesis

This thesis is organized in the following way. First, the experimental techniques are introduced in detail in Chapter 2. From Chapter 3 to Chapter 5, a series of investigations on the electronic and molecular dynamics in various systems are presented. In Chapter 3, the CEP- and intensity-dependence of the dissociative ionization in $D_2$ and DCl are introduced, followed by sub-cycle steering of proton migration in hydrocarbons. In Chapter 4, the experimental and theoretical investigations on the transient electronic dynamics in $C_{60}$ are presented. Experimental research on the collective electron motion in silver nanoclusters is introduced in Chapter 5. In a word, we emphasize on the electrons in motion on attosecond time scales, both individual and collective, from atomic and molecular scales to high-density nano-systems.

# Chapter 2

# Experimental techniques

## 2.1 Generation of few-cycle laser pulses

Near single-cycle near-infrared (NIR) pulses are widely used in the experiments included in this work. The laser is generated at the front end of the Petawatt-Field Synthesizer (PFS) at the Max-Planck-Institute of Quantum Optics [37], which provides a beam of 25 fs NIR pulses centered at around 790 nm with a repetition rate of 1 kHz and pulse energy of 2 mJ. After passing a triggered Pockels cell and a Glan-Thompson prism, the beam can be split in two such that the laser can be operated for two working groups without lowering the pulse energy. One part of the laser beam is guided through beam tubes towards the AS-5 beamline which is located in the laboratory downstairs. The beamline layout of AS-5 is shown briefly in Fig. 2.1.
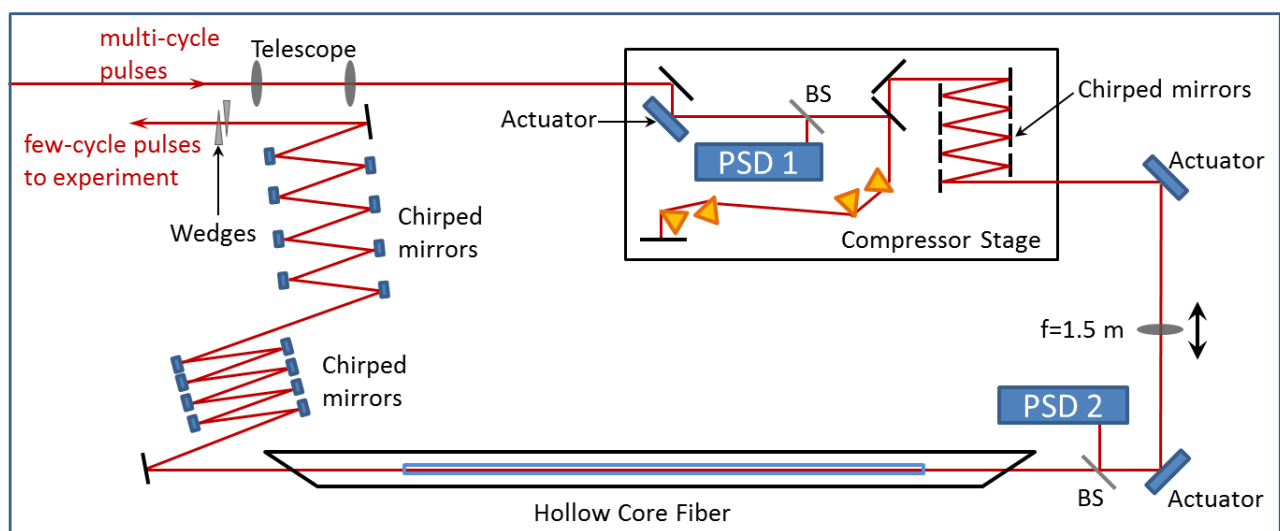


Figure 2.1: Overview of the AS-5 laser system (adapted from Ref. [38]).
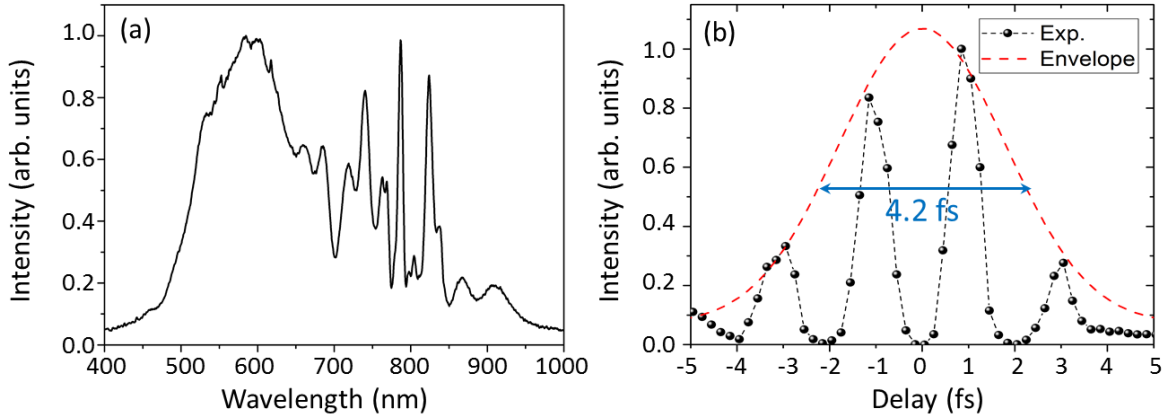
Figure 2.2: (a) Laser spectrum after the HCF. (b) Autocorrelation trace and the fitted envelope for the 4.2 fs laser pulse.

Due to the intrinsic divergence of Gaussian beams, the beam size at the entrance of AS-5 is about 2.5 cm after propagating over a long distance (>10 m). As shown in Fig. 2.1, a 1:2.5 telescope resizes the beam to around 1 cm in diameter. Then the laser is sent to a hybrid pulse compressor (HPC) which includes a double-prism pulse compressor and multi-pairs of high-dispersive chirped multilayer dielectric mirrors [39]. The double-prism is set such that there is some amount of positive dispersion left in the laser pulses before entering the chirped mirror sets. The high-dispersive mirrors (HDMs) provide negative dispersion therefore compressing the pulses to their Fourier transform limits, which is around 25 fs. Compared to traditional compressors based on prisms and/or diffraction gratings, the HDMs have several advantages. These includes simplicity, alignment-insensitivity, and higher efficiency. A commercial beam lock system (BeamLock 4D, TEM Messtechnik GmbH) is implemented in the HPC for stabilizing the pointing and position of the beam before entering the compressor stage. At the exit of the HPC, the laser spectrum centers at around 790 nm and extends from about 750 nm to 850 nm with a pulse energy at about 1.4 mJ. This beam is focused with a lens of 1.5 m focusing length into a hollow core fiber (HCF) filled with noble gas for spectral broadening. HCF is particularly suitable for ultrashort pulses of high energy due to its high damaging threshold and uniformity of the material [40]. Another beam stabilization system is placed before the HCF to insure a stable coupling of the laser beam into the fiber. The 1 m long HCF has an inner diameter of 275 $\mu$m. The fiber is kept straight in a V-groove, which is placed in a tube with Brewster windows on both the entrance and the exit sides. The tube is filled with Ne gas at a pressure of 2.8-3 bar. Due to the relatively high ionization potential of Ne, excessive ionization can be suppressed, thus reducing the ionization losses and the distortion of the incident laser pulses. Optical spectral broadening is achieved by self-phase modulation [41, 40]. For an ultrafast laser pulse, the intensity $I(t)$ is time dependent. When focusing a beam of such pulses in a medium, the refractive index (RI) of the medium will be modified due to optical Kerr effect [42], i.e. $n(t) = n_0 + n_2 I(t)$. Here the $n_0$ is the

RI in vacuum, and $n_2$ is the second-order nonlinear RI of the medium. As the pulse propagates, the intensity at a certain point in the medium will rise and fall as the pulse passes through. This will produce a time-varying RI and thus a nonlinear phase shift in the pulse ($\phi(t) = \omega_0 t - kz = \omega_0 t - \frac{2\pi}{\lambda_0}n(t)L$ with $\omega_0$ and $\lambda_0$ the carrier frequency and the wavelength of the pulse in vacuum, and $L$ the propagation length in the medium). The phase shift results in a change of the frequency in the optical spectrum. The instantaneous frequency $\omega(t)$ is given by $\omega(t) = \frac{\partial\phi(t)}{\partial t} = \omega_0 - \frac{2\pi L}{\lambda_0}\frac{dn(t)}{dt}$. In addition, self-steepening on the leading edge of the pulse makes the spectrum extend more to the blue side [43]. After the HCF, a transmission of 50% can be reached. The output pulses are linear polarized along the polarization direction of the incident beam. A focusing mirror behind the HCF was used to recollimate the beam after the fiber. Then the beam is sent to a set of broadband chirped mirrors [44] (8 pairs in our setup) which compensate for the positive dispersions induced by propagation through the HCF and optical elements and air. The dispersion can be precisely adjusted by a pair of fused silica wedges.

The spectum after the HCF covers a range from around 450 nm to 1000 nm (Fig. 2.2(a)). With the state-of-the-art double angle chirped mirrors, we can compensate the dispersion of such a broad spectrum and reach a pulse duration of about 4 fs, which is close to the single-cycle regime. The double-angle design of the chirped mirrors (5 ° and 19 °) [39] significantly reduces the group-delay dispersion (GDD) spectral oscillations as compared to single-angle broadband chirped multilayer mirrors. A delay-dependent total electron yield obtained from electron emission from He gas interacting with dual few-cycle pulses and the fitted Gaussian profile are shown in Fig. 2.2 (b), which show a laser pulse duration of about 4 fs (full width at half maximum, FWHM). However, there is still a lot of room for improvement. For instance, by splitting the spectrum into different spectral parts and compensating for the dispersions seperately, sub-cycle optical field can be obtained [45].

## 2.2   CEP-tagged single-shot velocity map imaging

Few-cycle laser pulses with a well defined waveform can steer the motion of electrons on a attosecond time scale. The electric field of the laser pulses can be expressed as $E(t) = E_0(t)\cos(\omega t + \varphi)$. Here, $E_0(t)$ is the envelope of the pulse, $\omega$ is the carrier frequency of the electric field, and $\varphi$ is the CEP, which is the phase offset between the carrier wave and the pulse envelope. Typically, the CEP is random from pulse to pulse due to the difference between the group and the phase velocity in the laser cavity. Among the control parameters, the CEP can significantly modify the pulse shape especially for the pulses approaching the single-cycle regime, as is shown in Fig. 2.3. To investigate the CEP-dependent processes, it is required that the CEP can either be stabilized or be measured shot to shot for an ultrashort laser system. However, with the best CEP-locking technique up to date, the stabilization can only last on the order of hours. In 2009, Wittmann et al. reported the first single-shot CEP measurement of few cycle laser pulses for a 3 kHz repetition rate [11]. In this work, the CEP is determined by detecting the ATI electrons using a single-shot stereo-ATI phase meter which consists of two opposing time of flight

(TOF) spectrometers. This opened a new route for CEP-tagging. By implementing the single-shot CEP measurement with other detection techniques, CEP-dependent phenomena can be explored. The first CEP-tagging experiment was realized with a reaction microscope (REMI) and a stereo-ATI phasemeter to investigate CEP-dependent processes in atoms [46]. Shortly after that, a single-shot CEP-tagged velocity map imaging (VMI) system was demonstrated at a repetition rate of 1 kHz at the AS-5 beamline in Max-Planck-Institute for Quantum Optics [12]. Most of the work presented in this thesis utilizes this system. Compared to the CEP-locking technique, a CEP-tagging measurement has many advantages. Firstly, measuring the CEP with a phase meter can attain a high accuracy around 100 mrad, which is significantly higher than the traditional CEP-locking method [13]. Secondly, CEP-tagging has the distinct advantage of being less complicated and more robust allowing continuous measurements for hours or days. This allows for studies of low-probability processes with increased signal-to-noise ratio. Thirdly, the conventional method for controlling the CEP requires movement of a silica wedge or a dispersive element (such as prism or grating) in a compressor. Together with CEP change, this movement also introduces a small change of the dispersion and laser peak intensity. If a CEP-dependent process is sensitive to laser chirp and/or intensity, it can be measured in a more precise way with the CEP-tagging technique.
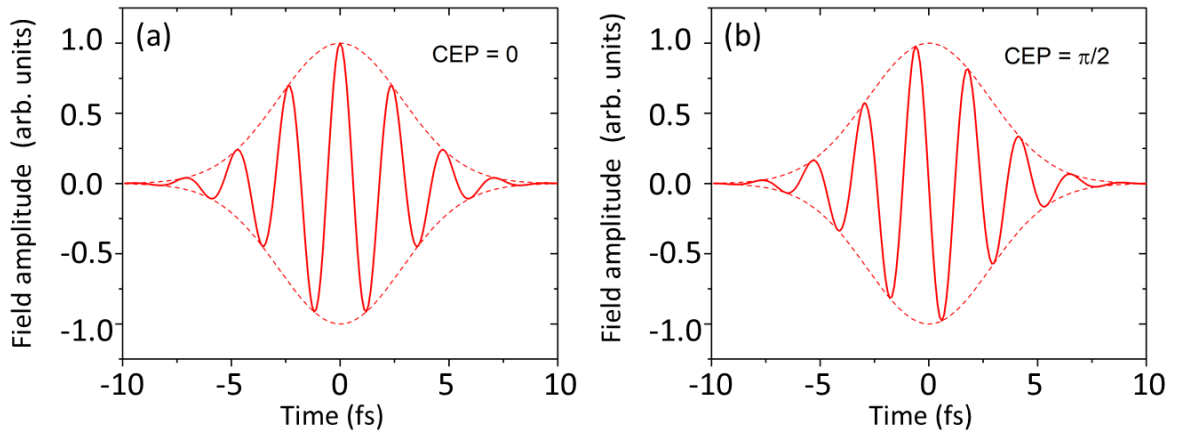


Figure 2.3: 4 fs pulses at 720 nm for (a) CEP=0 and (b) CEP=$\pi/2$.

## 2.2.1 Single-shot velocity map imaging

VMI spectrometers can provide a two-dimensional (2D) projection of the three-dimensional (3D) momentum distributions of charged particles [47, 48]. Both kinetic energy and emission direction of the products resulting from ionization, fragmentation, etc. are accessible in a single measurement.

Fig. 2.4 shows a typical design of an Eppink-Parker type VMI system [48]. The numerical simulations are performed with the SIMION software (SIMION 8.1). The electrostatic
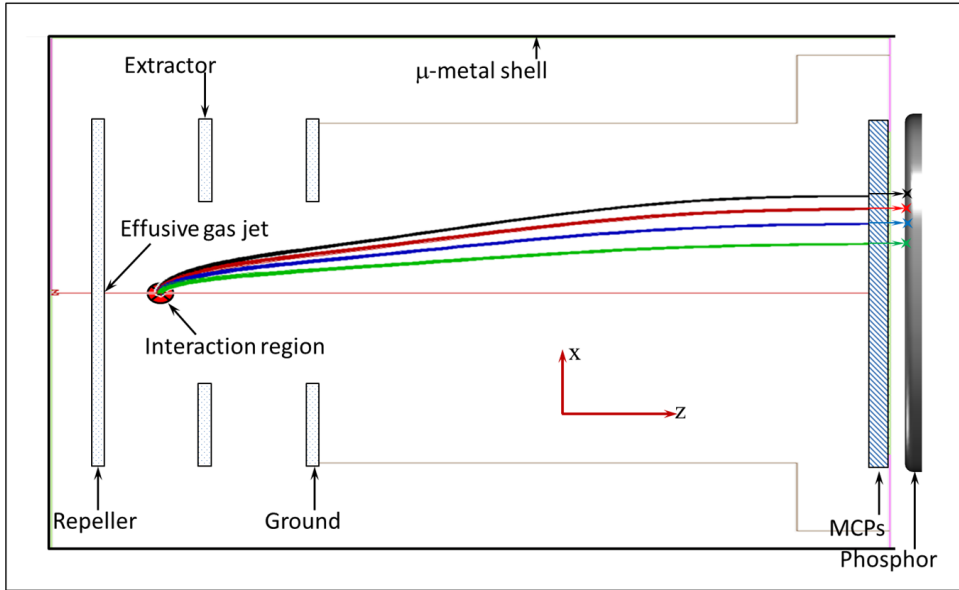
Figure 2.4: Design of a velocity map imaging (VMI) system. Electron trajectories at four different energies are calculated with SIMION software.

lens system contains a repeller, an extractor and a ground electrode. The position and geometry of these electrodes are designed such that by applying proper voltages on them, the charged particles with the same initial velocity at the interaction region will be focused onto the same point on the position-sensitive detector. There is a hole with a diameter of hundred microns at the center of the repeller plate for an effusive gas jet. The interaction region is located between the repeller and the extractor plates, where the laser beam is focused onto a beam of atoms, molecules or nano-particles. The resulting electrons or ions (depending on the polarity of the voltages applied on the electrodes) will fly towards the detector. The VMI spectrometer that was used in the experiments was designed and built at AMOLF [49]. The design in Ref. [49] used an integrated capillary on the repeller plate which extends closely to the interaction region. This is to maintain high target density for experiments especially with very low photon flux. Our VMI spectrometer simply has a flat repeller plate with a hole at the center for gas injection. The maximum voltages that can be applied to the ion optics electrodes are $V_{rep}$=15 kV and $V_{ext} \approx$12 kV. Electrons with kinetic energies up to about 100 eV can be detected. The detector consists of a pair of micro-channel plates (MCPs) and a phosphor screen (Hamamatsu F2226-24PX). A $\mu$-metal shell covers the whole spectrometer to block the stray magnetic field in the environment. Electron trajectories with 4 different initial momenta are shown in Fig. 2.4. Each color represents a momentum and includes 100 trajectories. Electrons emitted from the back surface of the MCP will be further accelerated towards the phosphor screen and generate photons that can be captured by an optical camera.

For charged particle distributions that possess cylindrical symmetry (which is typical for measurements in gases), Abel-transformation can be applied to the raw VMI images

to extract the original 3D distributions from the 2D projection [50]. Fig. 2.5 shows an example of electron emission from Xe gas when interacting with 4 fs NIR pulses at an intensity of $(6.5 \pm 0.5) \times 10^{13}$ W cm$^{-2}$.
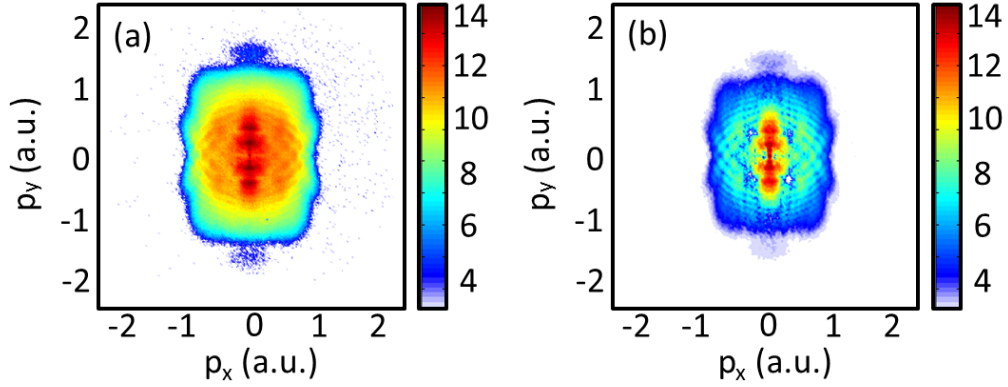


Figure 2.5: VMI images of electron emission from Xe with 4 fs linear polarized NIR pulses at an intensity of $(6.5 \pm 0.5) \times 10^{13}$ W cm$^{-2}$ before (a) and after (b) Abel-inversion. Laser polarization direction is along the y-axis.

For a single electron event on a VMI image, the radius with respect to the central point represents its momentum. The corresponding electron energy can be expressed as $E(r) = V_{rep}qr^2/k^2$. Here $V_{rep}$ is the repeller voltage in kV, $q$ is the charge quantity of the detected particles, $r$ is the radius in pixel, and $k$ is a scaling factor which is determined by the spectrometer geometry. It is well established that for ATI electron emission, the spectral spacing between consecutive peaks equals one photon energy. Thus it is used for energy calibration of the VMI spectrometer. Longer pulses, due to their narrower bandwidth, can provide higher energy resolution. Here, a beam of 25 fs NIR pulses at 790 nm is used. Fig. 2.6 shows the inverted VMI image and the spectra of electron emission from Xe. For a central wavelength of 790 nm, a spectral spacing of 1.57 eV is expected. The optimization results in $k = 56.15$.

The VMI spectrometer at AS-5 is adapted to single-shot mode by utilizing a high speed complementary metal-oxide semiconductor (CMOS) camera (GS-Vitec) at the full repetition rate of the laser. The camera is synchronized with the laser by a transistor transistor logic (TTL) trigger signal. The camera is connected with a high speed interface to a computer from which the camera can be controlled and single shot images can be stored. In the software (GS-Vitec Marathon Pro), a flat-field correction algorithm can reduce the inhomogeneous response of the CMOS chip. Then, a threshold intensity can be determined above which the pixel data are saved. The pixels below this threshold intensity will be discarded, as is shown in Fig. 2.7. After this processing, the signal-to-noise ratio can be enhanced dramatically by comparing Fig. 2.7(c) to (a). The above-threshold pixels will be saved by their position information (x and y) as well as intensity value (I). Each piece of information takes 2 bytes thus one pixel takes 6 bytes. At present, the limitation
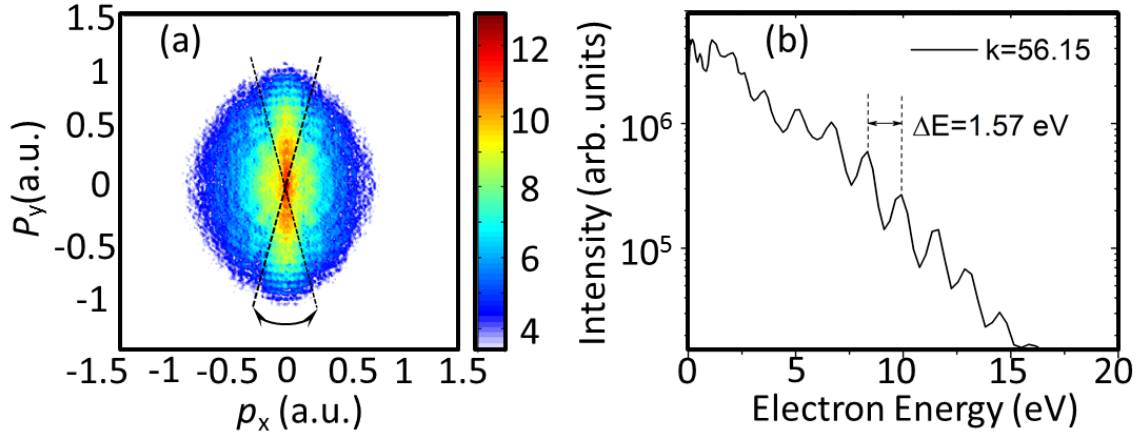
Figure 2.6: (a) An inverted VMI image of electron emission from Xe with 25 fs linear polarized NIR pulses at 790 nm. Laser polarization direction is along the y-axis. (b) The corresponding electron spectra obtained from (a) by integrating over an angle range of $\pm 15°$ with respect to the laser polarization.

of repetition rate is mainly restricted by the readout from the camera. With the camera controlling software a reduction of data rate is feasible and the processing can be handled by a standard desktop computer. In our setup, the camera chip and data bus to the host computer can record frames with 1 kHz repetition rate at a resolution of $800{\times}600$ pixels with 1024 'active' pixels (pixels that are above the threshold intensity) at the maximum.
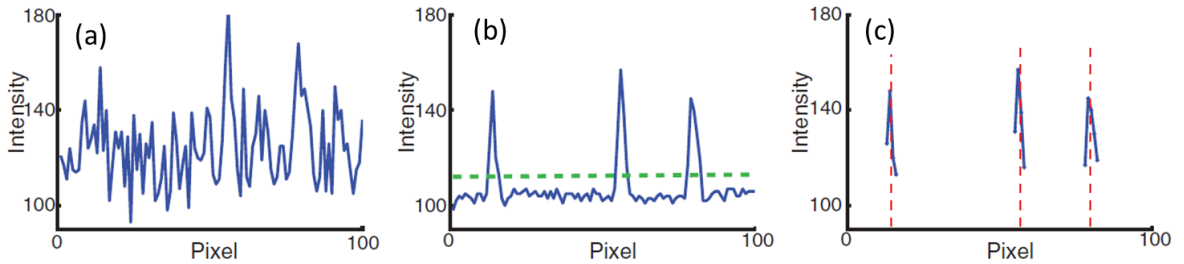


Figure 2.7: The CMOS line signal before (a) and after (b) flat-field correction. The green dashed line is the intensity threshold. (c) Signals above threshold. (Taken from Ref. [12])

## 2.2.2 Stereo-ATI phasemeter and phase tagging

Based on the strong CEP dependence of ATI photoelectrons, stereo-ATI detectors have been successfully used for measurements of the CEP of ultrashort laser pulses [51], even in the single-shot mode [11]. Fig. 2.8 displays a stereo-ATI phasemeter that consists of two time of flight (TOF) drift tubes with an MCP detector at each end [13]. The TOF drift
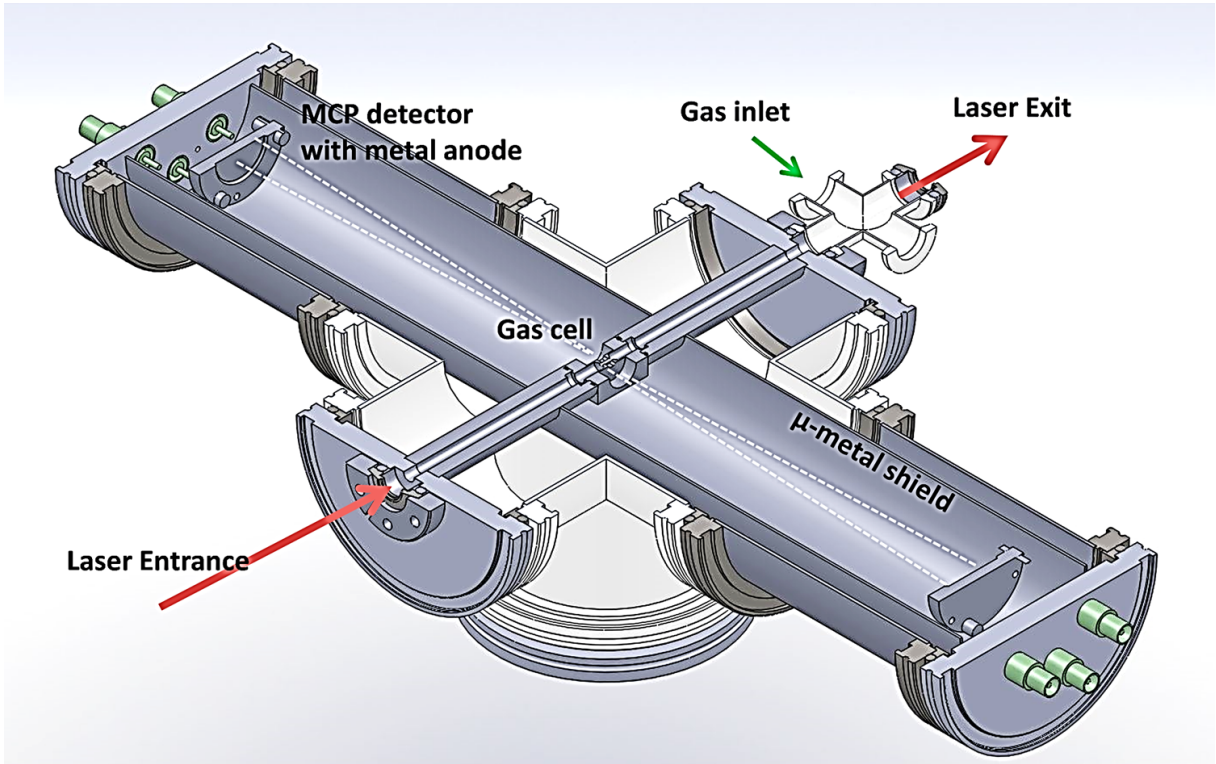
Figure 2.8: Schematic drawing of a stereo-ATI phasemeter. (Courtesy of Dr. Nora G. Kling)

tubes are surrounded by $\mu$-metal shells to keep them free of magnetic and electric field. The laser, at around 30 $\mu$J of pulse energy and polarizing along the detector axes, is focused in the middle of the gas cell with an $f = 250$ mm concave mirror where noble gas atoms are ionized. There are two slits on each side of the gas cell which allow the photoelectrons to travel to the detectors. These slits also perform as differential pumping apertures. Gouy-phase effects [52] can be neglected due to the small size of the slits. Typical photoelectron spectra from Xe obtained on both MCP detectors (marked as 'left' and 'right' detectors) are shown in Fig. 2.9 for two different CEPs. In the low energy regime (below 20 eV in Fig. 2.9), direct electrons are dominating. After being ionized, these electrons are driven by the laser field up to energies of 2 $U_p$, where $U_p$ is the ponderomotive energy. Direct electrons exhibit a higher yield but with a weaker CEP dependence. On the contrary, the higher energy electrons (above 20 eV) show a strong CEP dependence. These electrons are ionized and driven back towards the parent ion by the external laser field, and after rescattering gain more energy (up to 10 $U_p$) from the external field. They form the plateau in the high energy region with a small fraction of the total yield [53]. The higher sensitivity to the CEP is due to the fact that the recollision of electrons with the core is highly dependent on the shape of the electric field of few-cycle pulses [19]. Thus the rescattered electrons can be used for CEP measurement. To avoid saturation of the detector the direct electrons (which

comprise most of the yield) are suppressed by applying a low negative voltage (around -27 V) to a mesh located in front of the MCPs. This can also extend the lifetime of the MCPs.
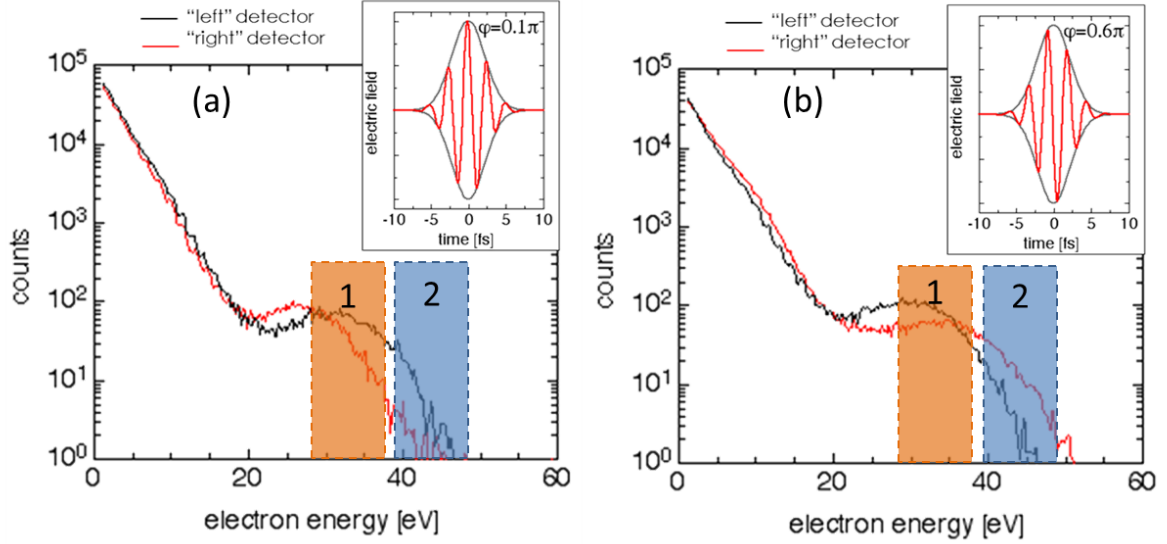


Figure 2.9: Recorded photoelectron energy spectra on both the "left" and the "right" detectors for two different CEPs, i.e. (a) CEP=$0.1\pi$ and (b) CEP=$0.6\pi$, with the two integration regions '1' and '2'. (Courtesy of Dr. Nora G. Kling)

During the measurement, the TOF signals are coupled out by an RC decoupling circuit connected to the detector anode. After amplification, the TOF signals are fed into a home-made processing electronics box designed by Mr. Horn at the Max Planck Institute of Quantum Optics. Signals within two distinct energy regions (marked by 1 and 2 in Fig. 2.9) on the ATI plateau are integrated. The resulting integrals $L_{1,2}$ and $R_{1,2}$ are used to calculate the two asymmetry parameters $A_{1,2}$ for each laser shot. The asymmetry parameter is defined as

$$A_{1,2} = \frac{L_{1,2} - R_{1,2}}{L_{1,2} + R_{1,2}}, \tag{2.1}$$

where $A_1$ and $A_2$ are readout by a peak-sensing analog-to-digital converter as voltage levels. These asymmetry parameters oscillate sinusoidally with respect to the CEP, and they are phase offset by about $\pi/2$ after optimizing the position and width of the two integration regions [13].

$$
\begin{aligned}
A_1 &\propto \sin(\varphi + \varphi_0), \\
A_2 &\propto \cos(\varphi + \varphi_0).
\end{aligned}
\tag{2.2}
$$

Here, $\varphi$ is the CEP and $\varphi_0$ is a constant phase offset with respect to the absolute CEP in the measurement. This offset can be calibrated by comparing the experimental data with theoretical simulations. From Eq. 2.2 we can see that the CEP can be derived as $\varphi = \arctan(A_1/A_2) - \varphi_0$. The two asymmetry parameter for each laser shot are plotted as a parametric asymmetry plot (PAP) and the result for many laser shots shows a 'phase potato', as shown in Fig. 2.10. Each point on the PAP represents a single laser shot. The angle $\theta$, which is defined starting at the positive x-axis, can be used to determine the CEP. The size of the PAP, i.e. $r$, is related to the pulse duration, since shorter pulses will result in a higher asymmetry thus a larger 'potato'. Besides, the thickness of the 'potato', $\Delta r$, represents the stability of the pulse duration.
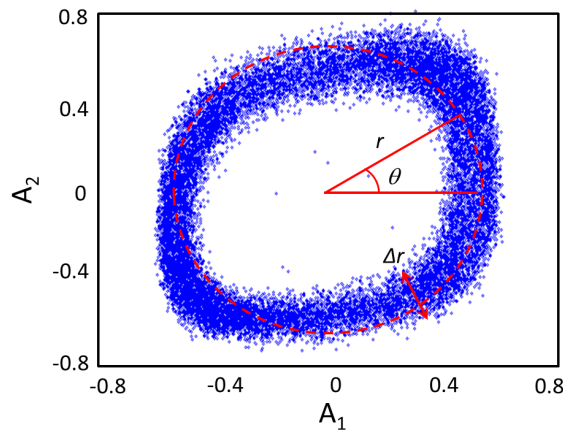


Figure 2.10: A parametric asymmetry plot (PAP) for about $10^4$ laser shots.

However, the PAP can never reach an ideal circular shape no matter how good the experimental parameters are optimized. To good approximation, the CEP from pulse to pulse can be assumed completely random for a free running CEP laser. And the resulting PAP should show a homogeneous count distribution over each phase [13]. Based on this, a rebinning process which redistributes the counts over each angle bin can make the measurement more accurate [38]. The conversion from $\theta$ to $\varphi + \varphi_0$ is obtained in this way.

The single-shot VMI spectrometer and the single-shot stereo-ATI phase meter are operated in a synchronized way to realize phase-tagged measurements. The two parts are controlled by the same trigger signal which is given by a TTL pulse generated by a constant fraction discriminator fed by a fast photodiode. As mentioned in Section 2.2.1, the bottleneck for this technique is solved by dramatically reducing the data amount for the VMI measurement by only recording the 'bright' pixels in single-shot mode. For each laser shot, an image is recorded by the VMI spectrometer together with a point on the PAP from the phase meter. In the post analysis process, the image data is assigned with the corresponding value of $\varphi$ for each laser shot. The PAP is divided into 20 equal angle ranges. The corresponding VMI images within the same angle bin are summed up, resulting in 20 images for the CEP range from 0 to $2\pi$. Higher CEP resolution can be obtained by using

a larger number of bins.

The typical setup for phase-tagged VMI measurements is shown in Fig. 2.11 (a) [12]. A beam of 4 fs NIR pulses are divided into two parts by a broadband 20/80 beam splitter. The small portion is sent to the stereo-ATI phase meter to detect the CEP for each laser shot. The main part of the laser beam is focused into a single-shot VMI spectrometer where it interacts with a beam of atoms, molecules [54, 55, 56], or nano-particles [57, 58, 59]. Each path contains a pair of fused silica wedges for fine adjustment of the laser dispersion. These wedges are set such that the pulses in the interaction regions are Fourier transform limited for both the VMI spectrometer and the phase meter, therefore leaving a constant CEP offset between them. The absolute phase is then determined from reference data measurements of electron emission from Xe gas under the same experimental conditions [54, 55].
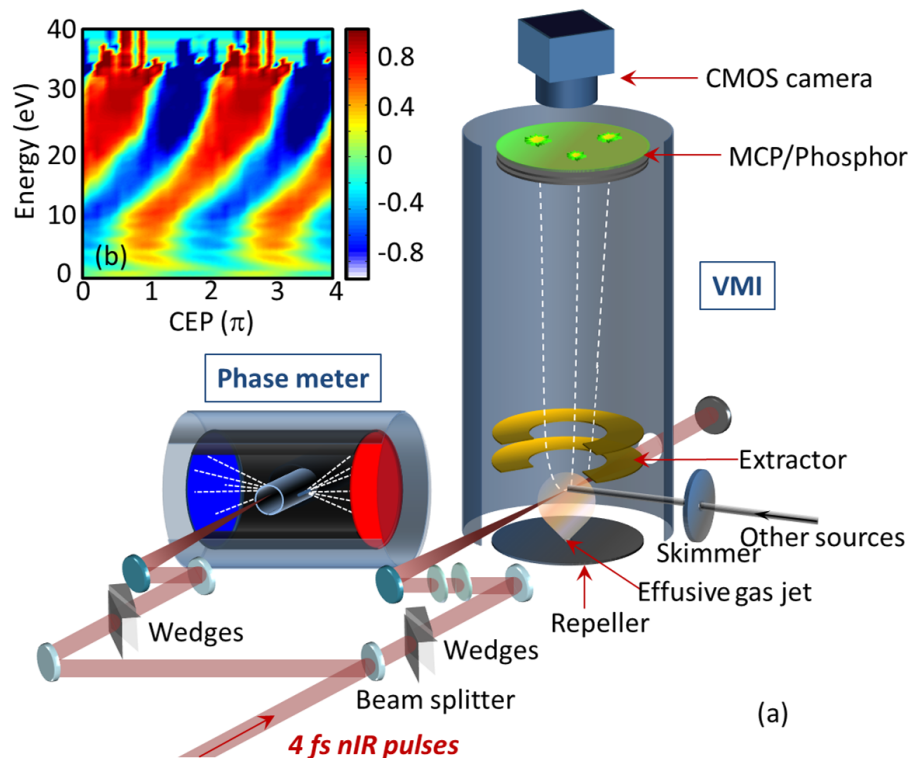


Figure 2.11: (a) A schematic drawing of a CEP-tagged single-shot VMI system. (b) The asymmetry map as a function of CEP and kinetic energy for electron emission from Xe gas with 4 fs NIR pulses.

As an example, an asymmetry map as a function of CEP and electron kinetic energy from Xe is shown in Fig. 2.11 (b). Large oscillation on the asymmetry parameter represents strong control on the directional electron emission using 4 fs laser pulses.

## 2.3    Sources

For studies of atomic and molecular gases, injection through an opening (hundred micron in diameter) in the center of the repeller plate was utilized. This opening is used for an diffusive gas jet. For studies of ultrafast electron dynamics in complex molecules and nanoclusters, special sources were designed. In this section, the generation of an effusive gas beam of $C_{60}$ molecules and metal nano-clusters will be described.

### 2.3.1    $C_{60}$ molecular beam source

A simple method to generate effusive neutral $C_{60}$ molecules is by heating purified $C_{60}$ powder in an oven. A vacuum compatible $C_{60}$ oven used in the experiments presented in Chapter 4 was designed in the group of Prof. Dr. Karl-Heinz Meiwes-Broer at Rostock University. The inch size oven is of a cylindrical shape as shown in Fig. 2.12. A piece of vacuum compatible cable heater is coiled around the oven body which is made of stainless steel. A thermocouple is attached to the oven to monitor the operating temperature. $C_{60}$ powder with high purity (usually above 98%) can be filled in the oven reservoir and exit from a millimeter hole at the end of the cylinder when heating up. This oven is installed on the side of the VMI chamber. A pair of movable slits lie in front of the oven, which can help to collimate the $C_{60}$ beam and adjust the beam size (around 1-2 mm in our experiment). The generating $C_{60}$ beam intersects with the laser beam orthogonally and the resulting electrons or ions can be detected by the VMI spectrometer.
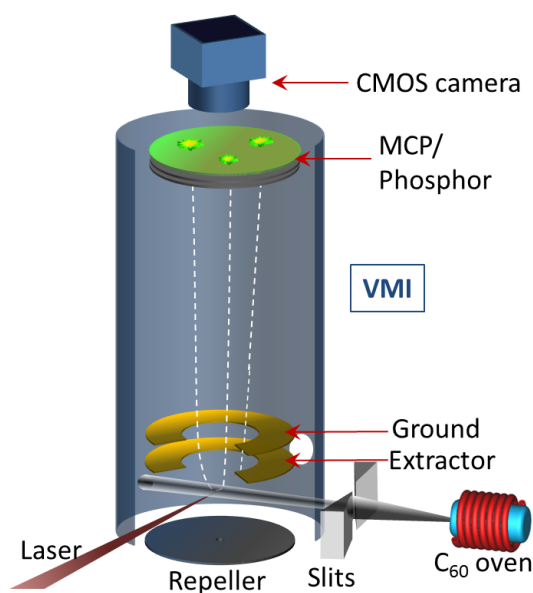


Figure 2.12: A schematic drawing of a $C_{60}$ oven adapted to the VMI setup.

The vapor pressure of $C_{60}$ under different temperatures has been well studied [60]. To

maintain a reasonable signal level, the oven was operated under a temperature of 500-600°C [55, 61]. To operate a device with such high temperature in a vacuum chamber, the heat radiation has to be taken into account. The performance of other devices may be affected by the temperature change. Therefore, the oven has to be put in a distance far enough to suppress the temperature influence on the VMI spectrometer but maintain a high enough target density at the interaction region. In our experiment, the $C_{60}$ oven was installed in a separate chamber that helped to reduce the heat transfer to the VMI spectrometer and other sensitive elements. The average particle densities in the laser focusing region can be estimated to be about $10^6$ molecules/cm$^3$ at an oven temperature of 500 °C. The density can be increased to one order of magnitude higher by increasing the temperature to about 550 °C [60]. In principle, higher target densities of $C_{60}$ can be realized by moving the oven closer to the interaction point and/or operating at a higher temperature. For example, a cooling enclosure of the oven can dramatically reduce the heat radiation thus allowing closer distance to the interaction region.

## 2.3.2 Nano-cluster source

The generation of nano-structures draws significant interest in the field of both research and industry. Among these nano-scale materials, nano-clusters are used as models to investigate fundamental properties when transiting from atoms and molecules to bulk materials. Based on Ref. [62], we designed a nano-cluster setup which can generate size-controlled metal clusters in ultra-high vacuum environment utilizing a magnetron sputtering source.

**Overview of the nano-cluster source setup**

The experimental setup for the nano-cluster source which includes several vacuum chamber stages is shown in Fig. 2.13. A magnetron sputtering source is attached to the main chamber via a manipulator with the adjustment in x and y directions which can help to align the cluster beam with respect to the experimental setups. During the operation of the source, large amounts of rare gases will be put into the vacuum chamber, therefore the main chamber is pumped by two turbo pumps (total pumping capacity > 3000 L/s) to maintain high vacuum. The source is electrically isolated from the rest of the apparatus which allows for applying a bias voltage. The generated nano-cluster beam is collimated by an aerodynamic lens [63] located at the end of the magnetron sputtering source, which is designed based on the work in Ref. [64, 65, 66]. As shown in Fig. 2.14, the aerodynamic lens is comprised of a series of apertures at certain distances. The geometry of this device is mainly determined by the size of the particles and the operating gas pressures at different stages. For our use, the opening from left to right are set to be 6.5, 5.0 and 4.0 mm for nano-clusters with the size of a few nanometers. Opposite to the exit of the cluster source, a skimmer cone with an opening of 2 mm is installed on the other side of the main chamber. This skimmer can help to get rid of the diffusive clusters, leaving only a small portion to propagate to the following vacuum chambers. On the other hand, the skimmer is the aperture towards the 1st differential pumpming chamber, which can support a pressure

reduction of about 2 orders of magnitude in the 1st differential stage when the source is operated. In the 1st differential pumping chamber (pumped by a 300 L/s turbo pump), ion optics including an einzel lens (EL) and a quadrupole mass spectrometer (QMS) are installed for particle analysis. The ionized clusters can be focused by the EI and deflected by about 90 ° in the QMS, and finally be detected by a home-made Faraday cup. A Pico-amperemeter (Keithley 6485) is used to measure the resulting current. The size of the particles can be estimated from the applied voltages on the QMS. Then the cluster beam is sent into the 2nd differential chamber (pumped by a 300 L/s turbo pump) and the experimental chamber (with a VMI or TOF spectrometer), which is shown in Fig. 2.13. A 2D adjustable slit was installed in front of the experimental chamber to confine the size and position of the cluster beam.
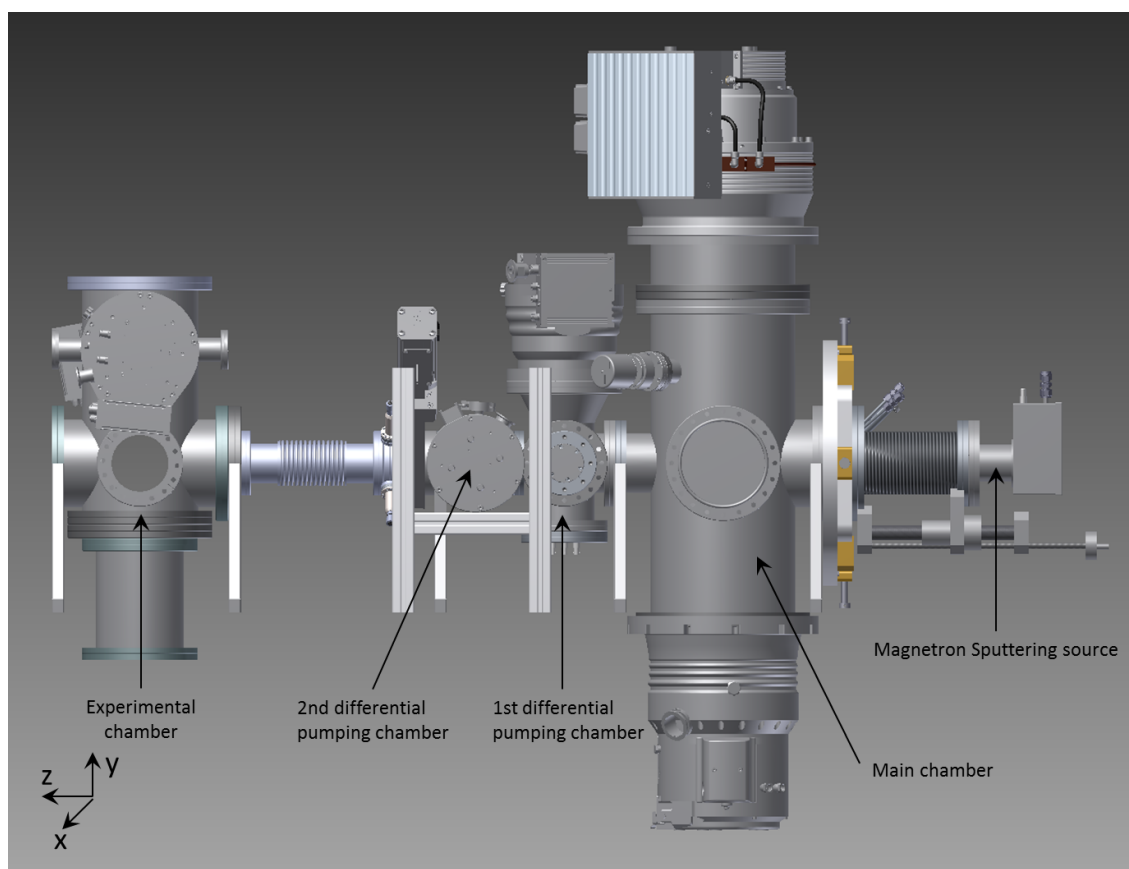


Figure 2.13: A schematic drawing of the vacuum system for the nano-cluster experiment.

### The magnetron sputtering source

Magnetron sputtering has been first utilized for generation of nano-clusters in the 90's [69]. In our setup we used a commercially available source (NC200U-B from Oxford Applied Research Ltd.) operated in DC mode to generate size-controlled nano-clusters from
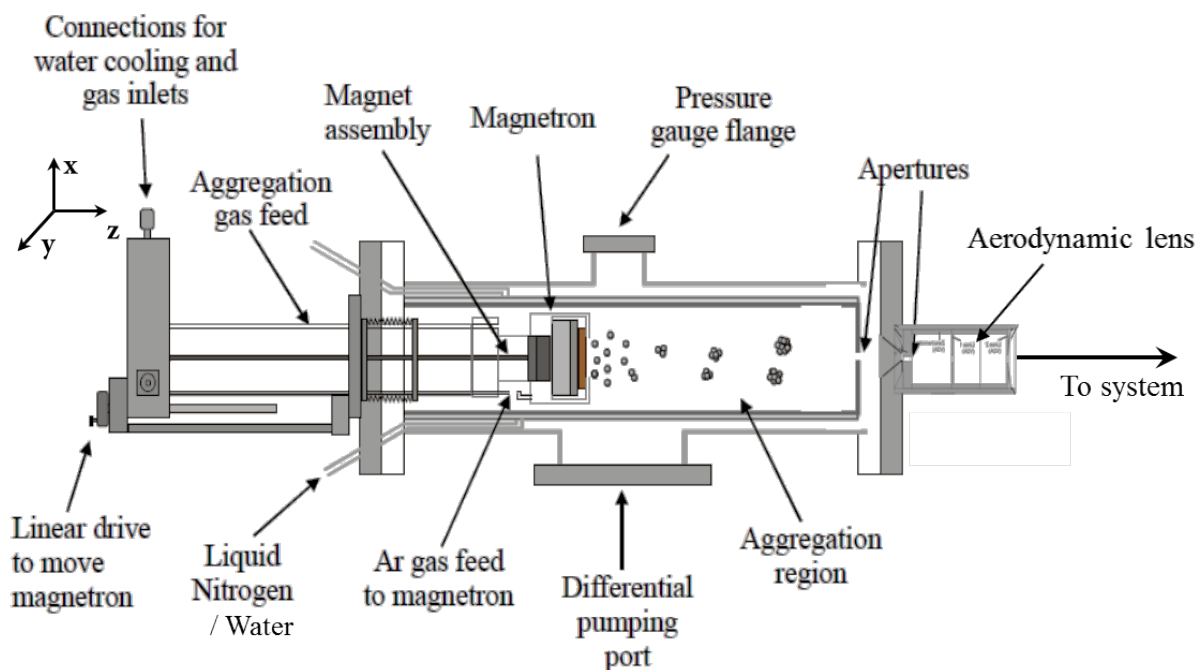
Figure 2.14: A schematic drawing of the magnetron sputtering source. (Adapted from [67])

conductive targets. Fig. 2.14 shows the structure of the source. In our experiments, a conducting target (Silver sputtering target, 99.99% purity, from Kurt J. Lesker Company) with a diameter of 2 inch and a thickness of about 6 mm is used. The target material is sputtered into an aggregation region where the clusters are formed. The distance between the magnetron gun and the exit of the aggregation region can be varied by the linear drive in a range within 100 mm allowing to vary the residual time of the clusters in the aggregation region, and hence the cluster size. Two kinds of rare gases, i.e. argon and helium, are used as sputter and aggregation gases. Argon is feed to the magnetron for discharge, while helium is used in the aggregation region to cool and sweep the atoms and clusters towards the exit of the source. The gas flows are regulated by two gas flow controllers (Type GE50A013500MAV020 from MKS). A mechanical manometer is installed to monitor the pressure in the aggregation tube. Typical operation pressure is on the level of a few mbar. The sputtering head and the aggregation tube were water cooled during the operation of the source.

An important problem when operating a magnetron sputtering source is to increase the deposition rate. The fundamental mechanism of sputtering (which is schematically shown in Fig. 2.15) is that the Argon ions from the plasma hit the surface of the sputtering target, transferring their energy to the target atoms through collisions, and some of the target atoms are ejected. The number of atoms leaving the target for each ion that hits it
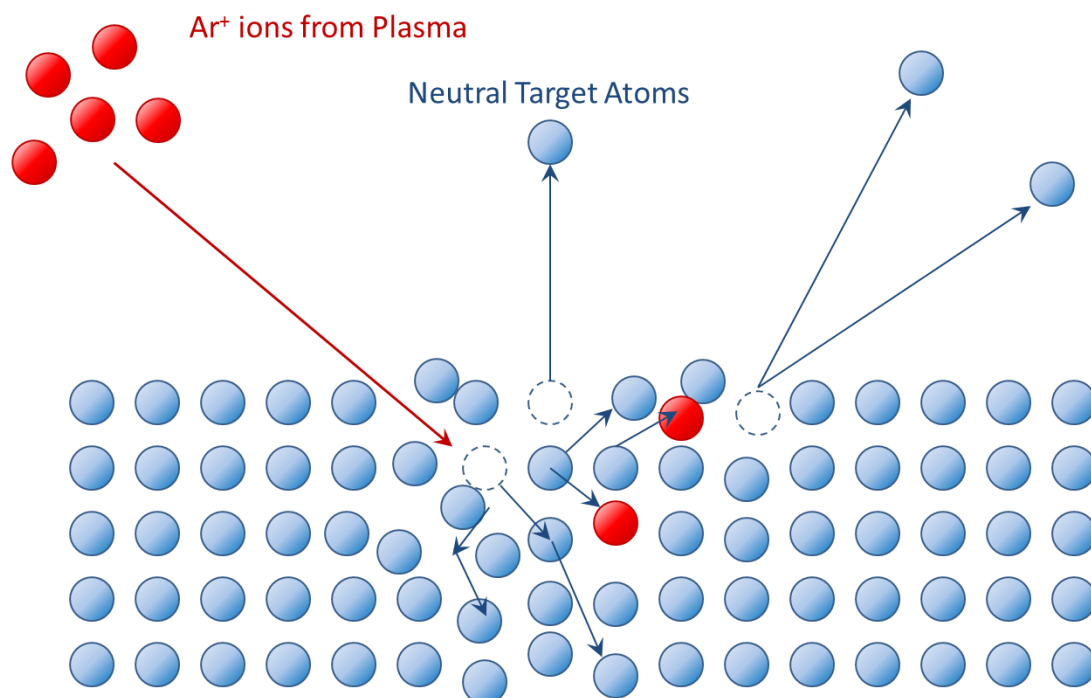
Figure 2.15: A schematic drawing of the basic mechanism of sputtering. (Adapted from Ref. [68])

is represented by sputter yield. This quantity depends on several parameters, such as the material, the mass of the incoming ion, the voltage through which the ion is accelerated, and its angle of incidence on the target. In principle, the likely approaches for enhancing the sputter yield include reducing the throw distances (target-to-interaction distance), increasing the magnetron power, optimizing the sputtering gas pressures, or even increasing target size. But each method has its own limit or drawback. For instance, reducing the throw distance is a simple way to increase the target density at the interaction point. However, the shorter distance will reduce the uniformity of the target density. And the sputtered particles will exhibit higher energy due to less collisions on the way. Besides, more stray electrons, more plasma ions and 'hot' neutrals, and higher thermal radiation heat transfer from the plasma have to be taken into account. Another simple way is to increase the power. But there are many adverse effects by arbitrarily increasing the power. The major part of the power applied to the gun will dissipate in the environment. If too much thermal energy deposited in the target cannot efficiently dissipate in time, or in other words, the thermal expansion of the target exceeds its maximum mechanical stress, or the temperature generated by the applied power goes over its melting point, the target will melt or crack. Each kind of material has its own maximum power. The critical quantity is the power density, which is the power applied divided by the surface area of the target. The maximum power density level for the highly conductive target (e.g., Al, Cu, Ag)

is about 15 W cm$^{-2}$ [68]. Based on this, with a certain maximum power density, it is possible to obtain higher sputtering yield from increasing target size. However, this is not easily accomplished since it requires a new design for a sputter gun and the corresponding apparatus. Lastly, lowering the sputter gas pressure can increase the deposition rate. The sputtered atoms leaving the target will undergo fewer thermal collisions. They are less likely to scatter 'sideways' thus a larger part will move to the interaction region. However, one potential side-effect of lowering the gas pressure is a change in target density uniformity. And another aspect is the likelihood of arcs occuring near the target when the gas pressure is too low.

**Ion optics**
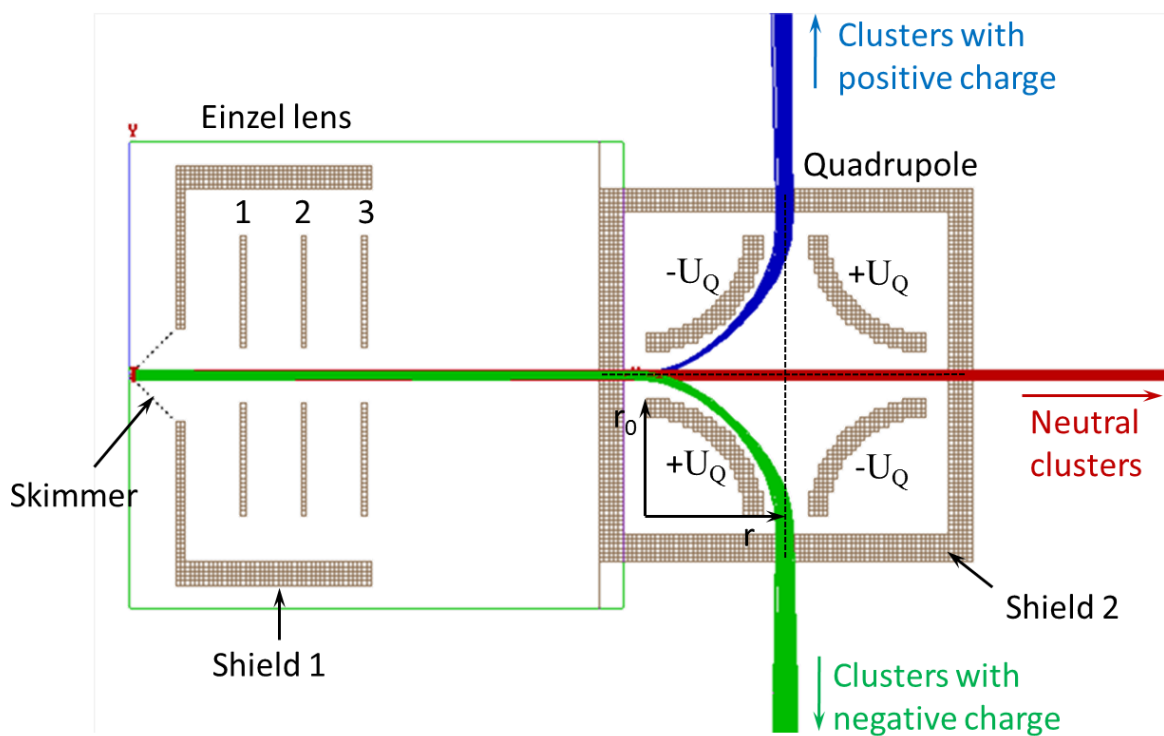


Figure 2.16: Design of the einzel lens(EL) and the quadrupole mass spectrometer(QMS) with trajectories for positive, negative and neutral nano-clusters, respectively.

During the generation of the clusters, multiple collisions with the He atoms result in an uniform distribution of the velocity of the particles. Thus the kinetic energy mainly depends on the cluster size, i.e. the number of atoms per particle. According to this, the size of the nano-clusters can be analyzed by a QMS which is installed in the 1st differential pumping chamber. To focus the charged cluster beam an EL was installed in front of the QMS.

The design of the EL and the QMS is based on the calculation of charged particle trajectories performed by SIMION, which is shown in Fig. 2.16. The EL consists of three ring-shape plane electrodes with a spacing of 12 mm between each plate. Depending on the kinetic energy of the charged particles to be focused, plate 1 and 2 will be set to the same voltage $V_0$, while the applied voltage on plate 3 is (75-80)% of $V_0$.

QMS is widely used as an energy analyzer and as an achromatic deflector of ionized beams [70]. Here, we use four pieces of quarter cylinders as the electrodes. The electrodes are biased with voltages of equal magnitude but different polarities ($\pm U_Q$) as shown in Fig. 2.16. An important parameter in the geometry is the ratio of $r/r_0$. In our setup, $r/r_0 = 1.2$. Based on this design, for a given applied voltage $V_Q$, the particles which can be deflected by about 90 ° and leaving the QMS through the exit should exhibit a kinetic energy of $(1.72 \pm 0.19)qU_Q$ [62]. Here $q$ is the charge of the particle. In Fig. 2.16, trajectories for positive, negative and neutral silver clusters with a diameter of about $8 \pm 1$ nm are shown. Each color represents a kind of particle and contains 100 trajectories. The beam divergence comes from the mass distribution. At typical operational parameters (power of the sputtering source at about 80 W, gas flow for Ar at 50 sccm and He at 10 sccm, the linear stage of the source at about 100 mm) the average cluster size of around 3-4 nm was obtained with the QMS (at an average applied voltage of about $\pm 140$ V). Large uncertainty of around 20% can be attributed to uncertainty of the velocity distribution, the beam divergence, and the low detected current. However, this simple design is enough for a rough detection of the cluster size for our use.

# Chapter 3

# Control of ultrafast molecular dynamics by tailored few-cycle pulses

## 3.1 Introduction

What processes can be studied by controlling the CEP for few-cycle (or even near single-cycle) laser pulses? Due to the high degree of asymmetry of the electric field, directionality of the fragment ion emission can be observed, which might originate from the following mechanisms. First, changing the CEP can manipulate the coupling of electronic states in molecules, which leads to electron localization and creates a CEP-dependent asymmetry. Experimental examples include the sub-cycle control of the ionization and dissociative ionization of hydrogen and its isotopes [5, 6, 7], and some diatomic molecules such as CO [71, 72, 73, 74]. Second, an asymmetric laser field can selectively ionize a subset of randomly oriented molecules, and the ionization of molecules with orientation dependent ionization rates can lead to an asymmetry. This mechanism has been discussed for the dissociative ionization of DCl [56] and CO [72, 74]. Third, recollisional excitation or ionization of the molecular ion induced by CEP-controlled pulses can result in directional fragment ion emission [75]. Fourth, laser induced coupling of vibrational states can lead to an asymmetry in molecular reactions. It was demonstrated recently that the directional control of the deprotonation process in hydrocarbons is based on the manipulation of the phases of vibrational wavepackets in superposition by the CEP of the few-cycle laser fields [76]. Another interesting dynamical process occurring in hydrocarbons when interacting with intense laser field is the hydrogen migration. Ultrafast hydrogen migration has been widely studied in various molecular systems using ultrashort pulses with tens of femtoseconds pulse durations [77, 78, 79, 80] and it was revealed that the hydrogen migration process occurred within about 40 fs [80]. The above mentioned mechanism leads to the possibility of manipulating much slower dynamics with ultra-short pulses, which only initiate the process and leave the system evolve without presence of the laser field.

In the first two sections of this chapter, we will discuss the intensity dependence of the

sub-cycle control on the dissociative ionization in simple molecular systems, i.e. $D_2$ and DCl, where $D_2$ is the isotope for molecular hydrogen and has been widely studied as a prototype and DCl is an interesting target for strong-field physics due to its large dipole moment [56, 81]. In the last section, the manipulation of proton migration in allene using few-cycle pulses will be discussed. We demonstrated recently that the hydrogen migration process can be steered in hydrocarbons utilizing few-cycle pulses by adjusting the CEP and laser intensity [82, 83, 84].

# 3.2   Intensity dependence of the sub-cycle control of the dissociative ionization in $D_2$

As a prototype system, molecular hydrogen and its isotopes have been attractive systems for the ultrafast community. The influence of the CEP on molecular dynamics has been widely studied for molecular hydrogen [7, 6, 5, 10] and molecular hydrogen ions [85, 86, 87]. Typically, the strongly driven electron-nuclear dynamics in intense laser fields needs to be described by quantum dynamical models beyond the Born-Oppenheimer approximation, which is still challenging for multi-electron systems. In this work, deuterium ($D_2$) molecules were chosen as the candidate for investigating the dissociative ionization in a 4 fs NIR laser field as a function of CEP and laser intensity [54]. Since only two electrons are involved, it is possible to access the system numerically with high accuracy [88]. Utilizing the phase-tagged single-shot velocity map imaging technique, the angular resolved momentum distribution of $D^+$ ions was obtained as a function of CEP. The intensity range we explored was around $(1.0\text{-}3.5)\times 10^{14}$ W cm$^{-2}$. Within this range, $D^+$ ions with high kinetic energies (above 8 eV) were observed and were assigned to the dissociation from higher excited states of $D_2^+$ by comparing the experimental data to quantum dynamical simulations.

## 3.2.1   Theoretical model
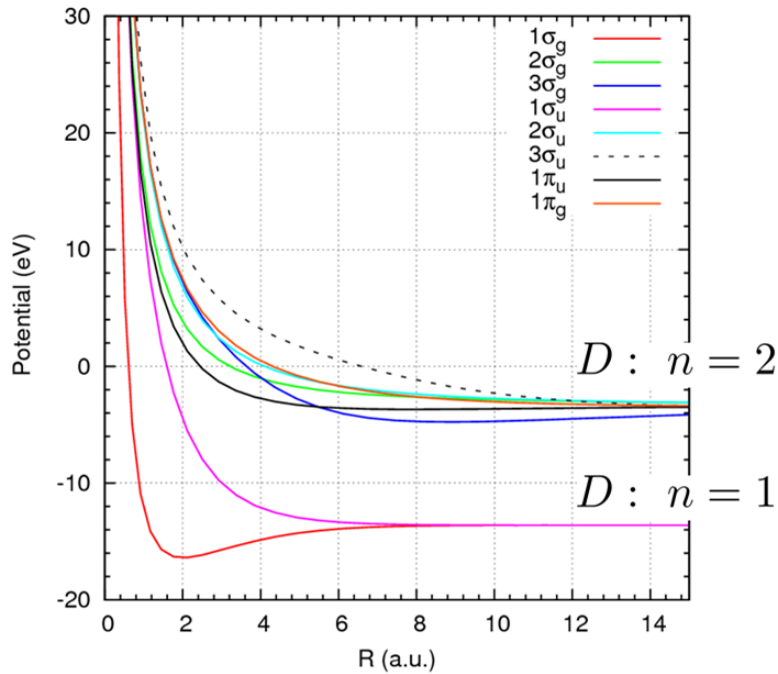


Figure 3.1: The first eight potential curves of $D_2^+$ used in the simulation. These curves are calculated as detailed in [89]. (Courtesy of Prof. Xiao-Min Tong)

The simulation work for the $D_2$ and DCl projects was carried out by Prof. Xiaomin Tong from the Institute of Material Science and the Center for Computational Sciences in the University of Tsukuba, Japan. In the simulation, the creation of $D^+$ ions in the intense laser field was treated in two steps. First, $D_2$ can be tunnel ionized near the local maximum of the electric field. The tunneling ionization rate is calculated according to the molecular orbital Ammosov-Delone-Krainov (MO-ADK) theory [36]. An electron is released into the laser field at time $t_0$. Meanwhile, a vibrational wave packet is created on the potential curve of $D_2^+$. Secondly, $D_2^+$ dissociates in the remainder of the laser field either directly from the ground state of $D_2^+$ or from excited electronic states that are populated through recollisional excitation when the ejected electron returns at a later time $t_r$ and collides with the $D_2^+$ ion. The returning time $t_r$ and the returning energy $E_r$ were obtained by a semi-classical simulation [90]. The time dependent nuclear wave packet (NWP) evolution of $D_2^+$ in the laser field was obtained by solving the coupled channel TDSE, which is shown below.

$$i\frac{\partial}{\partial t}\Psi_{i,g}(R,t) = H_{i,g}(R)\Psi_{i,g}(R,t) + \sum_{j,u} V_{i,g}^{j,u}(R,t)\Psi_{j,u}(R,t) \qquad (3.1)$$

Here the index $i$ or $j$ stands for the $1\sigma$, $2\sigma$, $3\sigma$ and $\pi$ states and $g/u$ stands for the gerade/ungerade or even/odd states. As shown in Fig. 3.1, the first eight potential curves of $D_2$ are included in this simulation. The Hamiltonian $H_{i,g}(R) = -\bigtriangledown^2/2 + U_{i,g}(R)$, is associated with a given potential curve $U_{i,g}(R)$. And $V_{i,g}^{j,u}(R,t)$ is the interaction between the $i,g$ and the $j,u$ states which are coupled by the laser field.

For a given initial state created at the time $t_r$, the NWP is propagated in the NIR field by Eqn. 3.1. When the NIR field is over, the NWP can be expressed as

$$\Psi(R) = \sum_i \int [C_{i,g}(E)\chi_{i,g}(R,E) + C_{i,u}(E)\chi_{i,u}(R,E)]dE. \qquad (3.2)$$

The NWP depends on the initial condition, the laser parameters and the alignment angle between the NIR field and the molecular axis [88]. Here $\chi_{i,g}(R,E)$ is the energy normalized continuum nuclear wave function for a given dissociative energy $E$, and $C_{i,g}$ is the amplitude.

For linearly polarized pulses polarized in the up-down direction, the electron (with the dissociation energy $E$) localization to the 'up' or 'down' direction is expressed by

$$C_{up}(E,t_0) = \frac{1}{2}\sum_i |C_{i,g}(E)exp[i\delta_{i,g}(E)] + C_{i,u}(E)exp[i\delta_{i,u}(E)]|,$$

$$C_{down}(E,t_0) = \frac{1}{2}\sum_i |C_{i,g}(E)exp[i\delta_{i,g}(E)] - C_{i,u}(E)exp[i\delta_{i,u}(E)]|, \qquad (3.3)$$

where $\delta_{i,g}(E)$ and $\delta_{i,u}(E)$ are the phase offsets for the gerade and the ungerade states at a certain dissociation energy $E$. With the potential curves included here, $D_2^+$ ion will finally dissociate to D(n=1,2) states, and result in $D^+$+D. Here n is the principle quantum number of hydrogen atoms.

**Dissociation from the NIR field**

If the D$_2$ molecule is ionized by the laser field at the time $t_0$, then the initial condition for Eq. 3.1 is

$$\Psi_{1\sigma_g}(R, t_0) = \sqrt{W(R, t_0)}\chi_g(R), \tag{3.4}$$

where $W(R, t_0)$ is the molecular tunnelling ionization rate [36] at a given nuclear separation $R$ and time $t_0$ with the over-barrier correction [91], $\chi_g(R)$ is the vibrational ground state wave function of D$_2$. The dissociation probability is calculated from Eq. 3.1, then the dissociation of the D$_2^+$ ion to the up/down direction is expressed as

$$P^{dis}_{up/down}(E) = \int |C_{down/up}(E, t_0)|^2 dt_0. \tag{3.5}$$

This formula indicates the probability of the directionality of the remaining electron left in the system. The D$^+$ goes to the opposite direction of the localized electron.

**Dissociation from recollisional excitation**

For recollision-induced dissociation, we assume that the D$_2$ is ionized by the laser field at the time $t_0$ and the electron returns to the parental core at the time $t_r$, then the initial condition for Eq. 3.1 is

$$\Psi_{j,g}(R, t_0 + t_r) = \sqrt{P_{j,g}(R, t_r)}exp(-iH_{1\sigma_g}t_r)\sqrt{W(R, t_0)}\chi_g(R), \tag{3.6}$$

where $P_{j,g}(R, t_r)$ is the electron impact excitation probability to the $j, g$ states at the position $R$ and $H_{1\sigma_g}$ is the vibrational Hamiltonian associated with the D$_2^+$ ground electronic state. The dissociation of D$^+$ to the up/down direction is expressed as

$$P^{res}_{up/down}(E) = \int |C_{down/up}(E, t_0, t_r)|^2 dt_0 dt_r. \tag{3.7}$$

Whether the D$^+$ ions are emitted to the up or down direction depends on CEP and their kinetic energy $E$. Here, we define an asymmetry parameter, $A_{th}$, which indicats the directionality of the emission.

$$A_{th}(\varphi, E) = \frac{P_{up}(\varphi, E) - P_{down}(\varphi, E)}{P_{up}(\varphi, E) + P_{down}(\varphi, E)}. \tag{3.8}$$

**The origin of the directionality of the D$^+$ ion emission**

As shown in Eq. 3.8, the asymmetry parameter is both CEP and kinetic energy dependent. The underlying physics can be expressed further. The time dependent NWP in the asymptotic region can be written as
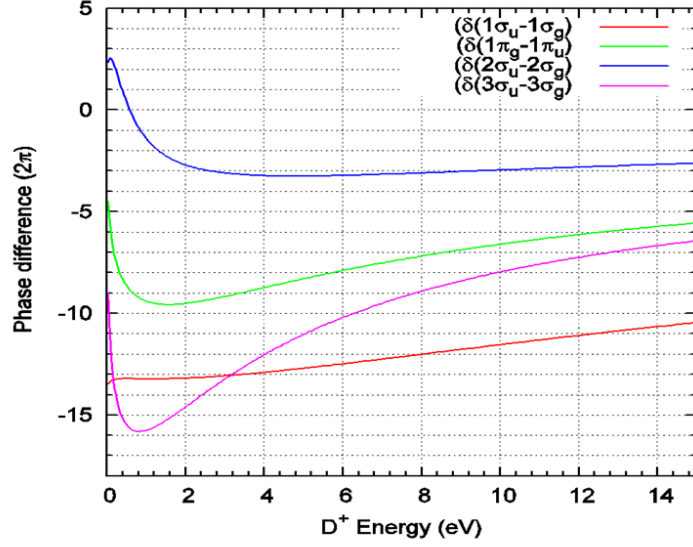
Figure 3.2: Phase difference between four groups of coupled excited states of $D_2^+$. (Taken from Ref. [54])

$$
\begin{aligned}
\Psi &= \Psi_g + \Psi_u = C_g e^{ikR} e^{i\delta_g} (\psi_{up} + \psi_{down})/\sqrt{2} + C_u e^{ikR} e^{i\delta_u} (\psi_{up} - \psi_{down})/\sqrt{2} \\
&= e^{ikR} \psi_{up} (C_g e^{i\delta_g} + C_u e^{i\delta_u})/\sqrt{2} + e^{ikR} \psi_{down} (C_g e^{i\delta_g} - C_u e^{i\delta_u})\sqrt{2} \\
&= \bar{C}_{up} \psi_{up} + \bar{C}_{down} \psi_{down}.
\end{aligned}
\tag{3.9}
$$

From this we can obtain

$$
\begin{aligned}
\chi_{i,g}(R,E) &\rightarrow exp[ikR + i\delta_{i,g}(E)] \\
\chi_{i,u}(R,E) &\rightarrow exp[ikR + i\delta_{i,u}(E)]
\end{aligned}
\tag{3.10}
$$

where $k = \sqrt{2\mu E}$, $\mu$ is the effective mass, $\delta_{i,g}(E)$ and $\delta_{i,u}(E)$ are the phase shifts for the gerade and the ungerade state pairs. Therefore the directionality of the electron localization depends on both the CEP and the difference between the paired phase shifts. The CEP-dependence results in an asymmetry oscillation with a period of $2\pi$. On the other hand, the phases of the NWP give rise to the energy dependence of the asymmetry. Fig. 3.2 shows the phase difference between four groups of coupled states as a function of the dissociation energy $E$. For the $1\sigma$ states, the phase changes by $\pi$ per 2 eV near the energy of 6 eV. For a high energy channel which originates from the dissociation via the $3\sigma$ states, the phase shift changes by $\pi$ in less than 1 eV energy range. This will be discussed further in Section 3.2.3.

### 3.2.2 Intensity dependence of the momentum distributions and the kinetic energy spectra of D$^+$ ions
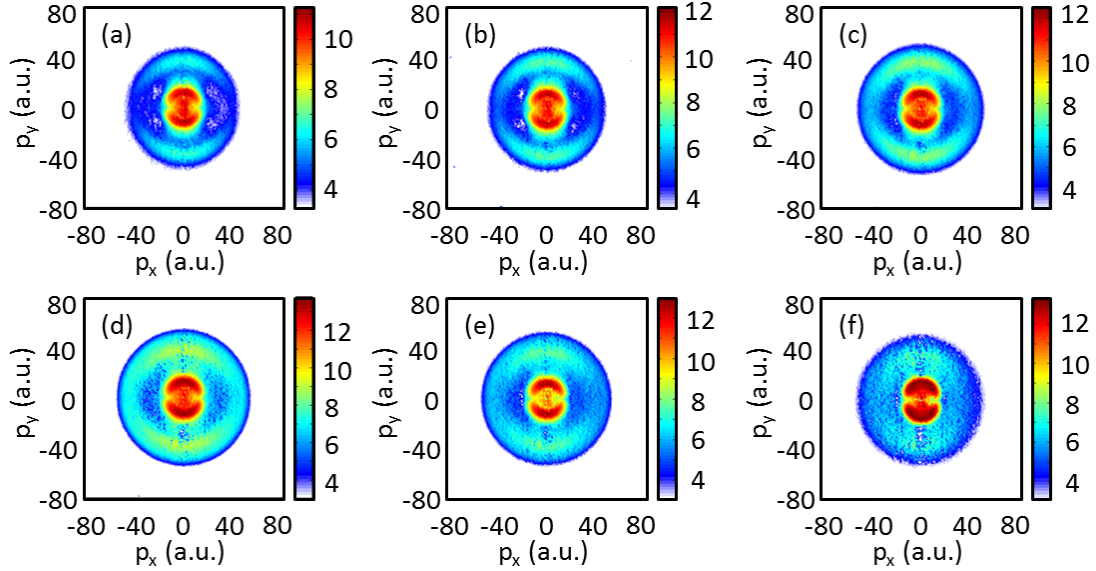


Figure 3.3: CEP-averaged inverted VMI images for D$^+$ ions in a 4 fs laser field at intensities of (a) $(1.0\pm0.3)\times10^{14}$ W cm$^{-2}$, (b) $(1.3\pm0.3)\times10^{14}$ W cm$^{-2}$, (c) $(1.8\pm0.3)\times10^{14}$ W cm$^{-2}$, (d) $(2.5\pm0.3)\times10^{14}$ W cm$^{-2}$, (e) $(2.8\pm0.3)\times10^{14}$ W cm$^{-2}$ and (f) $(3.5\pm0.3)\times10^{14}$ W cm$^{-2}$, respectively.

Fig. 3.3 shows the Abel-inverted VMI images of D$^+$ ion from D$_2$ in a 4 fs laser field at the central wavelength of 720 nm for laser intensities in the range of $(1.0\text{-}3.5)\times10^{14}$ W cm$^{-2}$. The laser was linearly polarized along the $p_y$ axis. The VMI images are CEP-averaged and show equivalent distributions in the up and the down directions. Two main contributions are visible: a strong peak at lower momentum (around 12 a.u. for the radial momenta $p_r = \sqrt{p_x^2 + p_y^2}$) with a relatively narrow angular distribution and a contribution at higher momenta (above 25 a.u.) with a broad angular distribution. There is another channel located between the above two channels at around 18-24 a.u. with even narrower angular distribution. The signal close to the center of the images (below 7 a.u.) might be contaminated by the H$_2^+$ which is ionized from the hydrogen molecules in the background. These two species can not be distinguished by the VMI spectrometer due to the same mass to charge ratio. Therefore the signal below 7 a.u. on the momentum map (corresponding to about 0.2 eV in kinetic energy) is not discussed. The corresponding kinetic energy spectra obtained from Fig. 3.3 by integration over the whole solid angle are shown in Fig. 3.4 (a), with the simulated spectra shown in Fig. 3.4 (b). The calculated spectra can reproduce the main features which are observed experimentally. The following reaction pathways lead to the observed features.
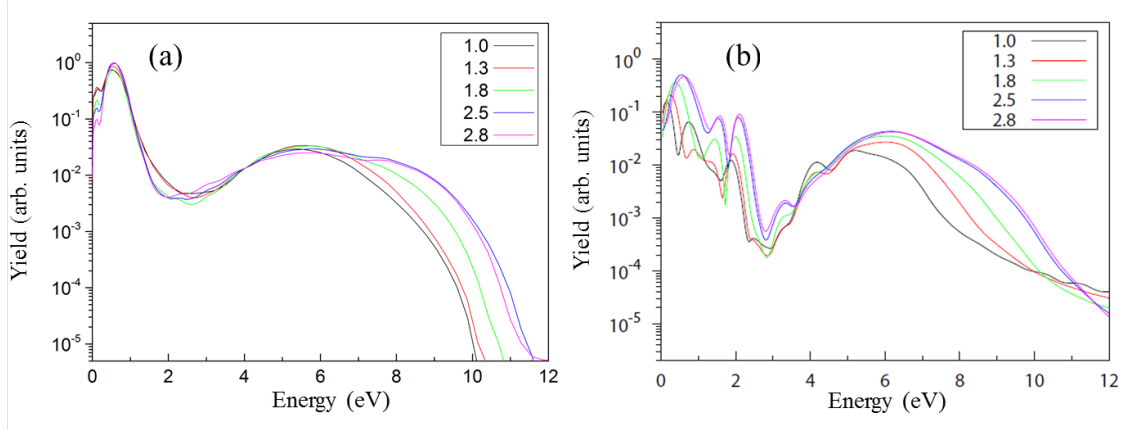
Figure 3.4: Energy spectra for $D^+$ ions from $D_2$ obtained for the laser intensities indicated in the legend (in units of $10^{14}$ W cm$^{-2}$) for (a) experiments and (b) simulations, respectively. The spectra from simulations are normalized to their values at 4 eV for better visibility of the high energy tails. (Adapted from Ref. [54])

- The strong peak around 0.7 eV in the spectra, corresponding to the signal on the momentum map around 12 a.u., arises from dissociation of the $D_2^+$ ground state via bond-softening (BS) [92]. BS requires that the cation streches to the crossing point for a one-photon transition from the ground state to the $1\sigma_u$ excited state. Actually, BS should not be expected for 4 fs pulses, since there is already not enough laser field left for the coupling when the wave packet moves to the proper region (this usually takes half the vibrational period, which is around 12 fs for $D_2$ [93]). The BS channel is mainly from the pedestal of the laser pulses, which are around 25 fs and are used to generate the few-cycle pulses. The intensity of this pedestal can be up to about 10% compared to that of the few-cycle pulses.

- The higher energy contribution above 3 eV (above 25 a.u. for the momentum) with a broad angular distribution can originate from the dissociation of the excited states of $D_2^+$ that are populated by either the laser field directly or recollision of the electron or both. This region becomes broader and extends to the higher energy region as the laser intensity increases, as shown in Fig. 3.3 and 3.4. Earlier studies have shown that the $D^+$ ion yield disappears in the high kinetic energy range when interacting with circularly polarized few-cycle pulses, as shown in Fig. 3.5 [8]. These indicate that recollisional excitation (RCE) is the dominating mechanism for the high energy yield.

- A contribution at around 2-3 eV located between the peaks for BS and the RCE channel, is assigned to a combination of above threshold dissociation (ATD) [7] and enhanced ionization (EI) [94].

As the laser intensity increases, the recollisional peak extends to above 8 eV. This high energy channel has been observed in studies on $D_2$ with few-cycle pulses at 760 nm [5] and
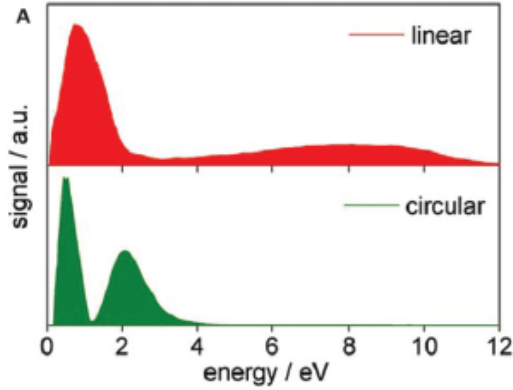
Figure 3.5: Kinetic energy spectra for D$^+$ (D$_2$) when D$_2$ interacts with 5 fs linear and circular polarized laser pulses at $10^{14}$ W cm$^{-2}$ without phase stabilization. (Taken from Ref. [8])

at 2.1 $\mu$m (mIR) [10]. But the directional ion emission was not discussed. We will further investigate the asymmetric ion emission and its intensity dependence in this high energy range.

The simulated contributions from different excited states of D$_2^+$ for three selected laser intensities are plotted in Fig. 3.6 (a-c). It is shown that for the lowest intensity, i.e. $1.0 \times 10^{14}$ W cm$^{-2}$, the ion yield is dominated by the dissociation from the 1$\sigma$ state. The maximum yield peaks at about 6 eV, which is in good agreement with the observed energy spectra. As the laser intensity increases to about $1.8 \times 10^{14}$ W cm$^{-2}$, the ion yield starts to arise from other highly excited states and their contributions increase with the laser intensity. The 1$\pi$, 2$\sigma$ and 3$\sigma$ are the main contributions right after the 1$\sigma$ state. At the intensity of $2.8 \times 10^{14}$ W cm$^{-2}$, the yield from dissociation from the 3$\sigma$ state extends to the high kinetic energy region above 8 eV. From this we reach the conclusion that the lower energy peak (below 8 eV) in the D$^+$ kinetic energy spectra mainly comes from dissociation involving the 1$\sigma$, 2$\sigma$, and 1$\pi$ states. The high energy peak above 8 eV comes from the 3$\sigma$ states when the laser intensity increases above $2 \times 10^{14}$ W cm$^{-2}$ for 4 fs pulses at 720 nm. On the other hand, Fig. 3.6 (d) shows that the yield of 3$\sigma$ states maximizes at about 15 degree alignment angle, while the yield of 1$\pi$ states changes almost oppositely. Based on the molecular tunnelling ionization theory [36], the tunnelling ionization rate weakly depends on the alignment of the molecule, and the electron impact dissociation is isotropic if there is no influence of an external field. The dissociation from a single state always results in a zero asymmetry due to conservation of parity. To obtain asymmetric emission, an external field is required for coupling of the gerade and the ungerade states [95]. The total dissociation probability weakly depends on the CEP. Thus, when the 1$\pi$ states (low kinetic energy on the potential curves) are excited to the 3$\sigma$ states (high kinetic energy on the potential curves), the yield of D$^+$ ions from the 1$\pi$ states is reduced while the one for dissociation via 3$\sigma$ states is increased. This can be further demonstrated in the following section where the angular distribution of the asymmetric emission of D$^+$ is analyzed.
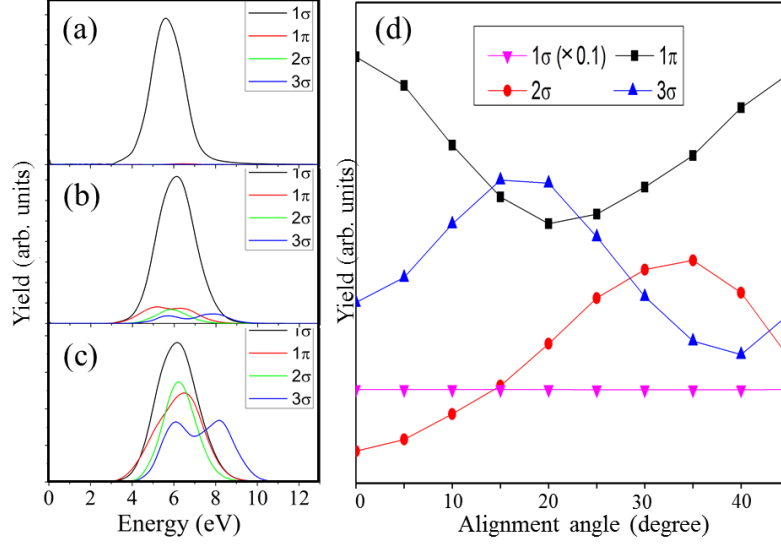
Figure 3.6: Simulated contributions in the $D^+$ kinetic energy spectra from different $D_2^+$ states at the intensities of (a) $1.0{\times}10^{14}$ W cm$^{-2}$, (b) $1.8{\times}10^{14}$ W cm$^{-2}$, and (c) $2.8{\times}10^{14}$ W cm$^{-2}$, respectively. The data are volume and alignment angle averaged. (d) Simulated dissociation yields through different states as a function of molecular alignment angle for a laser intensity of $1.8{\times}10^{14}$ W cm$^{-2}$. (Adapted from Ref. [54])

### 3.2.3 Intensity dependence of the directionality of the $D^+$ ion emission

The CEP- and energy-dependence of the directionality of the $D^+$ ion emission from the dissociative ionization of $D_2$ in the few-cycle laser field can be analyzed by the experimental asymmetry parameter $A_{exp}$, which is defined as

$$A_{exp}(\varphi, E) = \frac{Y_{up}(\varphi, E) - Y_{down}(\varphi, E)}{Y_{up}(\varphi, E) + Y_{down}(\varphi, E)}, \tag{3.11}$$

where $Y_{up/down}(\varphi, E)$ represents the ion yields in the up/down direction (along the laser polarization direction) obtained by integration within a certain angular range. An integration range of $\pm 45°$ is used for the following analysis. All the experimental data are CEP calibrated by comparing to the measurement on electron emission from Xe gas under identical experimental conditions.

The comparison between the experimental and simulated asymmetry maps as a function of ion kinetic energy and CEP are shown in Fig. 3.7 for three selected laser intensities. Volume averaging is taken into account in the theoretical simulation for better comparison with the experimental data. As expected, the asymmetry parameter oscillates with respect to the CEP with a period of $2\pi$. The asymmetry parameter reaches about 40% for the loweset intensity investigated here, which indicates a strong control on the directional ion
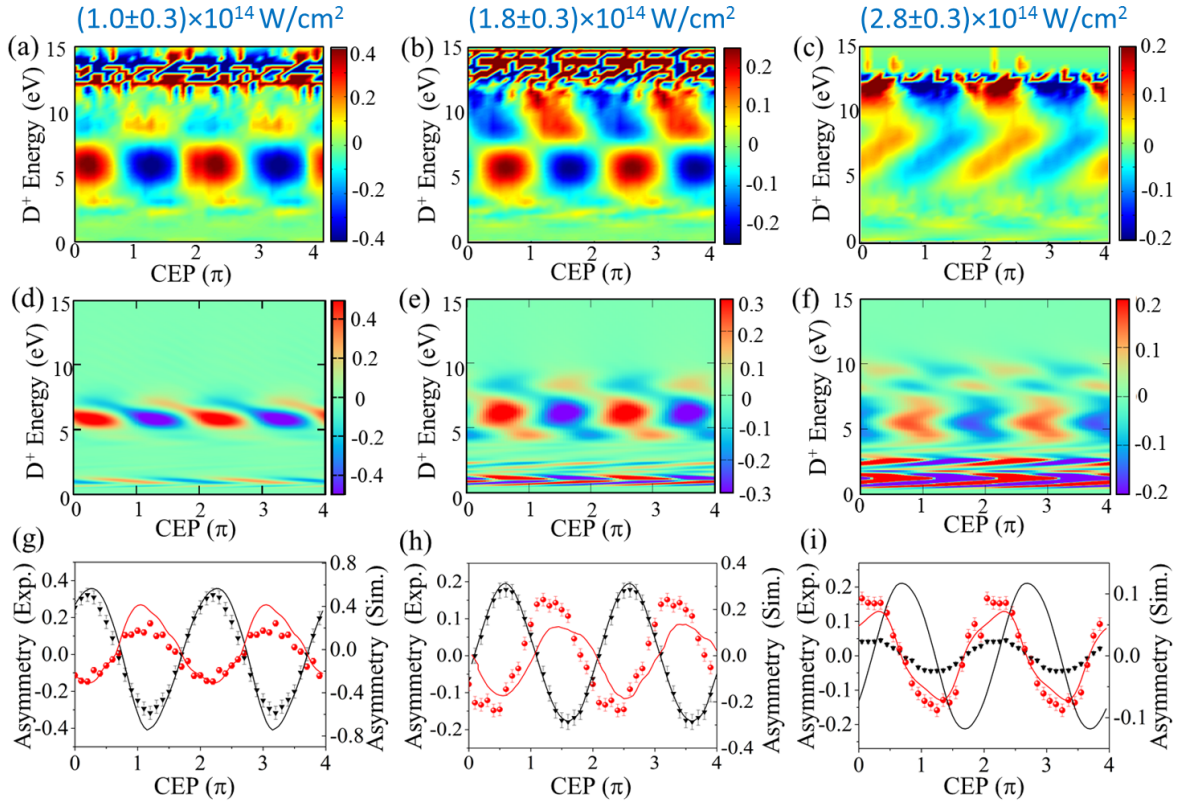
Figure 3.7: Experimental (a-c) and simulated (d-f) asymmetry maps of the D$^+$ ion from D$_2$ as a function of kinetic energy and CEP at the intensities of (1.0±0.3), (1.8±0.3) and (2.8±0.3)×10$^{14}$ W cm$^{-2}$, respectively. (g-i) Asymmetry oscillations integrated over the energy regions of RCE-I(black data) and RCE-II(red data) for both experiment (scattered triangles and bullets) and simulation results (solid lines). (Taken from Ref. [54])

emission with 4 fs laser pulses. The asymmetry maps also show very complex intensity dependent behaviors for the whole kinetic energy range. Asymmetric D$^+$ ion emission with high kinetic energy up to 12 eV is observed for higher laser intensities.

First, we focus on the high energy channel (above 3 eV) which exhibits higher asymmetry amplitudes. And, as inferred by the asymmetry oscillation shown in Fig. 3.7 (a-c), we divide it into two parts. The first channel, referred to as the RCE-I, is centered around 6 eV for the intensities of (1.0±0.3) and (1.8±0.3)×10$^{14}$ W cm$^{-2}$ and around 7 eV at the higher intensity of (2.8±0.3)×10$^{14}$ W cm$^{-2}$. The second contribution with even higher kinetic energy above 8 eV and exhibiting a clear phase shift with respect to the RCE-I channel is referred to as the RCE-II region. This phase shift is about $\pi$ at (1.0±0.3)×10$^{14}$ W cm$^{-2}$ and changes as the laser intensity increases. The phase relation can be better illustrated in the kinetic energy integrated asymmetry plots shown in Fig. 3.7 (g-i). The energy regions for the RCE-I and RCE-II channels are intensity dependent and are slightly deviated for the simulation results. They are listed in detail in Table 3.1.

Table 3.1: Integrated kinetic energy ranges for the RCE-I and RCE-II regions.

| Intensity(W cm$^{-2}$) | | $(1.0\pm0.3)\times10^{14}$ | $(1.8\pm0.3)\times10^{14}$ | $(2.8\pm0.3)\times10^{14}$ |
|---|---|---|---|---|
| RCE-I | Exp. | 4-7.5 eV | 3.7-7.3 eV | 4-9 eV |
| | Sim. | 5-6.5 eV | 5-7 eV | 4-7.5 eV |
| RCE-II | Exp. | 8-9.5 eV | 7.5-11.3 eV | 9.5-11.8 eV |
| | Sim. | 6.5-8 eV | 7-10 eV | 9-10 eV |

The selected energy regions are slightly lower for the simulations. One potential reason for the discrepancy in the kinetic energy between measured and calculated data is that the energy shift due to the screening effect from the ionized electrons [96] is not taken into account in the simulation. Assuming that the screening parameter (the Debye lengh) is $\lambda_d = 20 + 5 \times R^2$, the resulting kinetic energy of D$^+$ ions can be shifted by about 1 eV.

As shown in Fig. 3.7 (g-i), clear asymmetry oscillations are obtained for the RCE-I and RCE-II region and their phase shifts with respect to each other are laser intensity dependent. For the lowest intensity, an asymmetry as high as 40% was obtained for the RCE-I region. The experimental conditions used here are close to what was used by Kling *et al* [5] when the CEP-dependent ion emission of D$^+$ ion from deuterium molecules in few-cycle laser fields was first investigated experimentally. They used 5 fs NIR pulses at an intensity of about $1.3\times10^{14}$ W cm$^{-2}$. We used a similar laser intensity $((1.0\pm0.3)\times10^{14}$ W cm$^{-2})$ with a shorter pulse duration. The overall feature of the asymmetry map is comparable for both results. However, the asymmetry oscillation we obtained is about two times higher in amplitude compared to what reported in Ref. [5]. This can be attributed to the difference in the pulse duration and laser intensity. As shown in Fig. 3.8, a series of simulations are performed on D$_2$ and the resulting asymmetries show strong dependence on both the laser intensity and pulse durations.

As shown in Fig. 3.7 (a), the relative phase shift between the RCE-I and the RCE-II region is around $\pi$ at $(1.0\pm0.3)\times10^{14}$ W cm$^{-2}$. The simulation results show nice agreement for both the overall asymmetry pattern and the integrated oscillations at this laser intensity in Fig. 3.7 (d) and (g). However, the asymmetry amplitude from the simulated results are higher than what was obtained from experiment. This is from the large deviation of the simulation results for the low laser intensities which will be discussed in detail later in this section. Here the CEP for both the experimental data and the quantum dynamical simulation were processed seperately. The surprising nice agreement on the phase for the lowest intensity further verified our method for CEP calibration. The asymmetry oscillation near the spectral cutoff in the RCE-II region is selected as a reference for CEP.

As the laser intensity increases, the asymmetry pattern extends to higher energy regions and the relative phase relation between the two RCE channel changes. Particularly, the directional emission of the RCE-II region reaches to around 12 eV for intensities above $1.8\times10^{14}$ W cm$^{-2}$. The simulation results can qualitatively reproduce the evolution of the asymmetry behavior for the increasing laser intensities, but with some deviations, especially for higher intensities. Despite this, the general tendency can be reproduced. First, compared to the RCE-II region, the phase of the RCE-I region moves towards larger CEP values with higher laser intensities. This can be clearly seen in the energy integrated
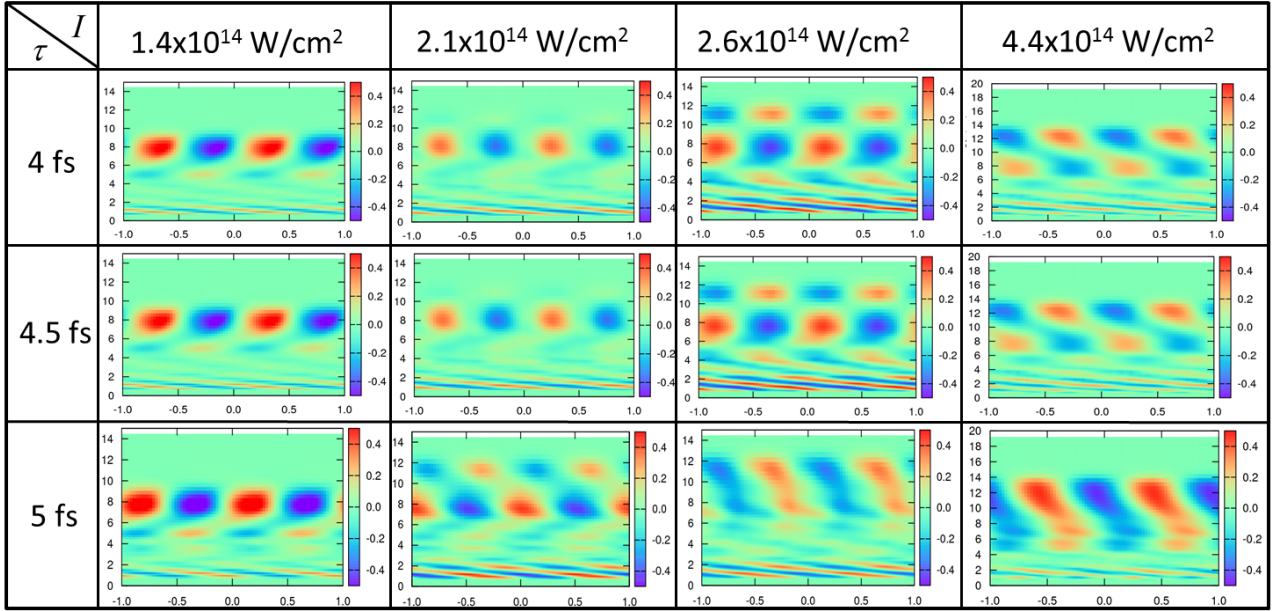
Figure 3.8: Simulated asymmetry maps of D$^+$ ion as a function of kinetic energy and CEP for different pulse durations and laser intensities as indicated. For all the asymmetry maps, the y-axis is the D$^+$ energy in unit of eV and the x-axis is the CEP in unit of $2\pi$. Volume averaging is not taken into account here. (Courtesy of Prof. Xiaomin Tong)

asymmetry curves shown in Fig. 3.7 (g-i). Secondly, the RCE-I region show no notable energy dependence at the intensity up to about $1.8 \times 10^{14}$ W cm$^{-2}$. This also agrees with the previous study [5]. As the laser intensity increased above $2.0 \times 10^{14}$ W cm$^{-2}$, the asymmetry pattern becomes more complicated compared to the results at lower laser intensities.

For intensities below $2.0 \times 10^{14}$ W cm$^{-2}$, the returning electron is not energetic enough to excite the ground state of D$_2^+$ to $3\sigma$ states. Thus the $3\sigma$ state is populated by laser-field-induced excitation. The field-induced transition results in a dipole-like angular distribution in the high energy part which is visible on the momentum maps shown in Fig. 3.3 for the low intensities. On the other hand, we have mentioned that the molecular alignment dependence of the dissociation yield for different excited states (Fig. 3.6 (d)) showed that the $3\sigma$ state can be excited from the $1\pi$ state by the laser field. When this takes place, the yield of D$^+$ ions from the $1\pi$ state drops while the one for the dissociation via the $3\sigma$ state increases. This transition result in a $\pi$ phase offset between the RCE-I and RCE-II regions. As the intensity increases, electrons with a higher returning energy are obtained which can directly excite the D$_2^+$ from its ground state or lower lying excited states to the $3\sigma$ states. The recollisional induced transitions to the high excited states can be in phase with each other. Therefore, for the case of high laser intensities, the two kinds of processes which are out-of-phase and in-phase compete with each other and result in a complex phase relationship for the two RCE regions on the asymmetry maps.
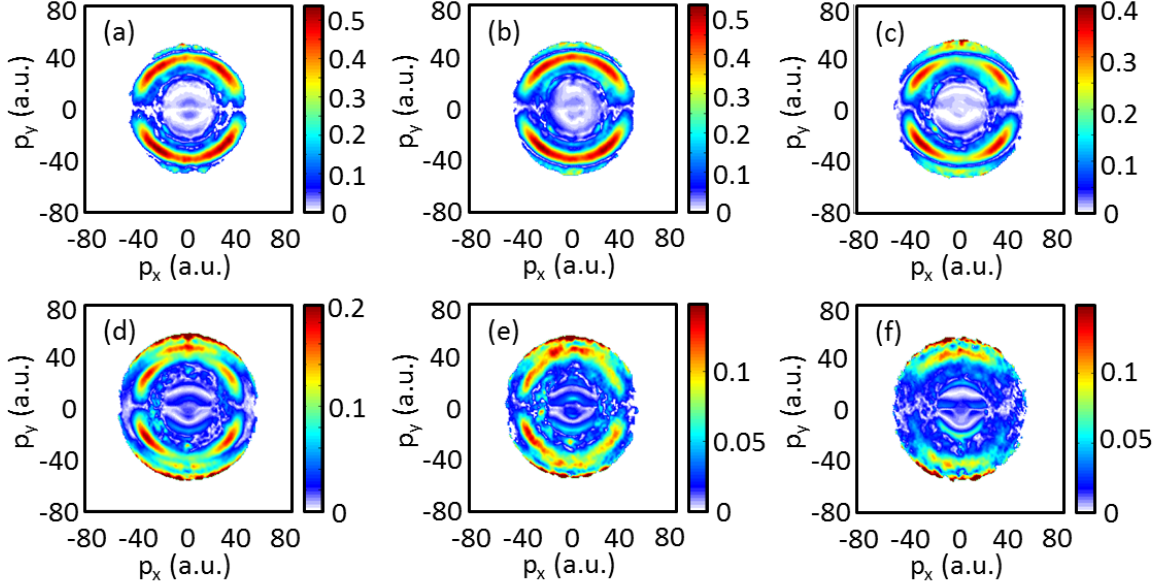
Figure 3.9: Momentum maps for the amplitude of the CEP-dependent part of the $D^+$ ion emission at the laser intensities of (a) $(1.0\pm0.3)\times10^{14}$ W cm$^{-2}$, (b) $(1.3\pm0.3)\times10^{14}$ W cm$^{-2}$, (c) $(1.8\pm0.3)\times10^{14}$ W cm$^{-2}$, (d) $(2.5\pm0.3)\times10^{14}$ W cm$^{-2}$, (e) $(2.8\pm0.3)\times10^{14}$ W cm$^{-2}$ and (f) $(3.5\pm0.3)\times10^{14}$ W cm$^{-2}$.

In addition, our further analysis on the angular distribution of the CEP-dependent $D^+$ emission can help to support the above mechanisms. For each position in the momentum space, the CEP-dependent $D^+$ yield can be fitted with a cosine function expressed below:

$$A_{exp}(p_x, p_y, \varphi) = A_0(p_x, p_y)\cos(\varphi + \Delta\varphi(p_x, p_y)), \qquad (3.12)$$

where $p_x$ and $p_y$ are the coordinates in momentum space. $A_0$ and $\Delta\varphi$ are the amplitude and the phase shift of the yield for the CEP-dependent part of the ion emission. $\varphi$ is the phase measured by the stereo-ATI phase meter and has a constant offset with respect to the absolute CEP. The momentum images shown in Fig. 3.3 are binned with $2\times2$ pixels in the fitting process for the improvement of the signal to noise ratio. The resulting momentum maps for the amplitudes ($A_0$) and the phase shifts ($\Delta\varphi$) are shown in Fig. 3.9 and 3.10, respectively. Combined with Fig. 3.3, the angular distributions of the CEP-dependent part of the $D^+$ emission show clearly the different excitation mechanisms. The contributions around 12 a.u. in radial momenta are from the BS channel. The RCE channel occupies the region above 25 a.u. and centers around 40 a.u.. The asymmetry observed for the BS channel is very weak at the low intensites (as shown in Fig. 3.9 (a-c)). As the intensity increases, a weak asymmetry contribution for the low momentum region shows up from about $2.5\times10^{14}$ W cm$^{-2}$. This is assigned to ATD. The RCE channel shows very wide angular distribution for up to around $3.0\times10^{14}$ W cm$^{-2}$. A small depletion along the polarization axis is observed and is the most visible in Fig. 3.9 (d). The depletion
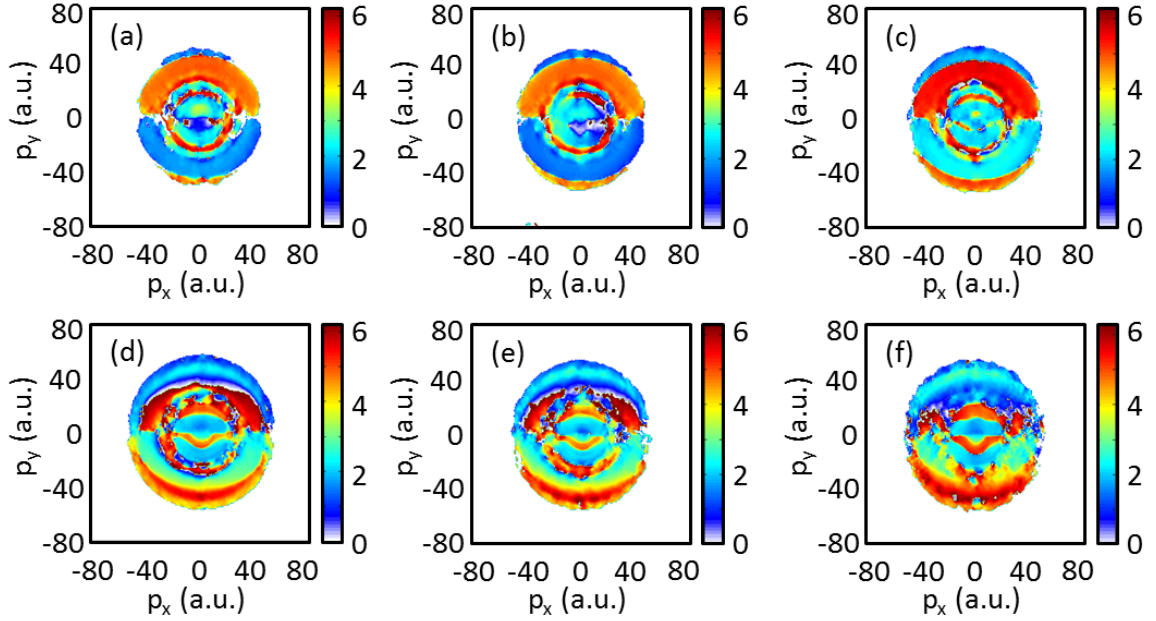
Figure 3.10: Momentum maps for the phase offsets of the CEP-dependent part of the D$^+$ ion emission at the laser intensities of (a) (1.0±0.3)×10$^{14}$ W cm$^{-2}$, (b) (1.3±0.3)×10$^{14}$ W cm$^{-2}$, (c) (1.8±0.3)×10$^{14}$ W cm$^{-2}$, (d) (2.5±0.3)×10$^{14}$ W cm$^{-2}$, (e) (2.8±0.3)×10$^{14}$ W cm$^{-2}$ and (f) (3.5±0.3)×10$^{14}$ W cm$^{-2}$.

goes along with the formation of an asymmetry contribution at higher radial momenta with narrower angular distribution along the laser polarization axis and is assigned to a sequential process of recollisional excitation from the $1\pi$ to the $3\sigma$ state which is induced by the laser field. For the highest intensity investigated here, i.e. around $3.5\times10^{14}$ W cm$^{-2}$, the depletion becomes too strong and the contribution from the higher momenta region is predominant. As a matter of fact, the dissociation energies of the $1\sigma$, $2\sigma$ and the $1\pi$ state are very close to each other thus cannot be distinguished in kinetic energy. However, by comparing the angular dependence of the oscillation amplitude and the alignment behavior shown in Fig. 3.6 (d), we can reach the conclusion that the ring-shaped contribution (RCE-I) are mainly from the dissociation via the $1\pi_g$, while the outer rings in the RCE-II region are from dissociation via the $3\sigma_u$ and $3\sigma_g$ states. The phase changes between the RCE-I and RCE-II regions on the momentum maps of the phase offsets shown in Fig. 3.10 further support the conclusion of the different mechanisms. Another aspect is that the asymmetry amplitude goes to zero in the direction perpendicular to the laser polarization, as shown in Fig. 3.9. This is due to the fact that the asymmetric ion emission requires the laser coupling of two states with opposite parities. There is no coupling for the perpendicular direction to the laser polarization.

Last, the intensity dependence of the asymmetry amplitude for the two RCE regions is compared between simulation and experiment and is shown in Fig. 3.11. The simulation
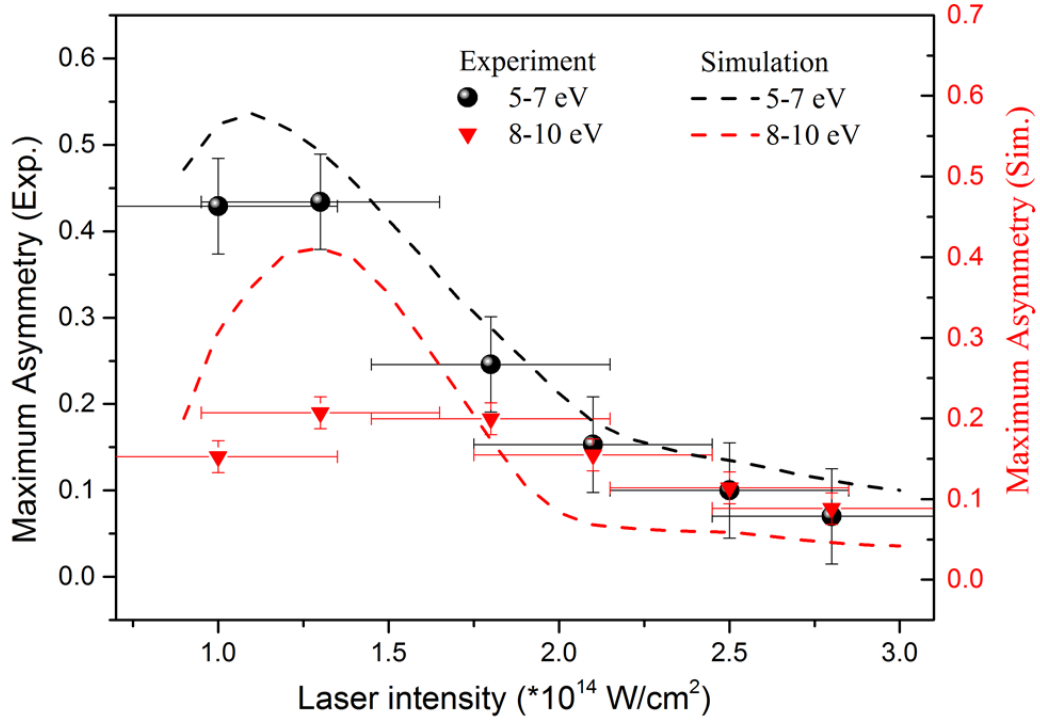
Figure 3.11: Intensity dependence of the amplitudes of the asymmetry oscillations for the RCE-I (black data) and RCE-II (red data) regions obtained from experiments (scattered bullets and triangles) and simulations (dashed lines). (Taken from Ref. [54])

can reproduce the observed tendency qualitatively with slightly higher amplitudes. The main features of the intensity dependence are as follows.

- The optimal intensity for the highest asymmetry to occur for the two RCE channels is slightly above $1.0 \times 10^{14}$ W cm$^{-2}$ in a 4 fs NIR laser field, as indicated by both experiment and theory.

- As the laser intensity goes away from the 'optimal intensity', the asymmetry amplitude decreases for both lower and higher laser intensities.

- Within the intensity ranges that are explored here, the asymmetry amplitude for the RCE-I region is higher than that for the RCE-II region.

An interpretation for the trend of the asymmetry amplitude as a function of laser intensity is as follows. The asymmetry of the dissociation mainly associates with the time at which the dissociative states are created in the laser field. In the case of low intensity, some excited states of $D_2^+$ can only be populated when the returning energy is high enough. And this occurs only within a narrow CEP window, which results in a large asymmetry. For higher intensities, the returning energies for almost all the CEPs are higher than the excitation energy thus are enough to create the excited states. The yields of the excited

states at different CEPs are identical due to the fact that the yield depends on the energy of the returning electron [97]. This leads to the vanishing of the asymmetry which agrees with the decreasing of the asymmetry amplitude for higher laser intensities.

Despite the nice agreement on the general tendency, large discrepancies exist between the simulation and the experimental results. The semi-classical simulation we used here underestimates the electron returning energy, especially in the lower intensity region, and in turn underestimates the yield of the recollisional induced dissociation from the higher excited states. The maximum return energy used in our simulation is 3.2 $U_p$, where $U_p$ is the ponderomotive energy. However, a quantum simulation can obtain an returning energy around 5-6 $U_p$ [98, 99], which is much higher than the semi-classical results. In the simulation, the dissociation mainly comes from the $1\sigma$ states at the lowest intensity. The smaller asymmetry parameter is due to the large energy gap between the two $1\sigma$ states (as shown in Fig. 3.1). This results in a large mismatch between the maximum asymmetry in experiments and simulations at the lower intensities.

## 3.3    Intensity dependence of the sub-cycle control of the dissociative ionization in DCl

HCl and its isotope DCl are interesting targets for the study of strong-field ionization due to their large dipole moment. It is possible to isolate the tunneling contribution of the highest occupied molecular orbital (HOMO) from that of the next-highest-energy orbital (HOMO-1). In a recent study, Akagi *et al.* studied the dissociative ionization of HCl in circularly polarized laser fields, where the ground X-state is produced by tunnel ionization from the HOMO, and the A-state from the HOMO-1 [81]. Theoretical studies suggested that due to the influence of the permanent dipole moment, CEP-controlled linearly polarized few-cycle pulses can induce directionality in the fragment emission in the laser-induced dissociation of the DCl$^+$ ion [100]. Investigations also show strong asymmetric D$^+$ ion emission from DCl$^+$ at long laser wavelengths [101]. An experimental report on the dissociative ionization of DCl with few-cycle pulses at 720 nm at a peak intensity of $1.3\times10^{14}$ W cm$^{-2}$ has shown that the kinetic energy independent directionality of D$^+$ ion emission was from an orientation dependence of the tunnel ionization [56]. We conducted extended experimental studies on DCl using 4 fs NIR pulses at several intensities [102]. The angular distribution as a function of CEP provides insight into the population mechanisms of the excited states of the molecular ion.

### 3.3.1    Theoretical model

A simple semi-classical model is used to investigate the underlying dynamics when deuterium chloride interacts with a strong field. SAE approximation is utilized for such a complex system with many electrons. The Hamiltonian can be expressed as

$$H = T + V_{Cl}(r_1) + V_D(r_2) + V_C(r),$$                (3.13)

Here $T$ is the kinetic energy operator, $V_{Cl/D}(r_{1/2})$ is the potential of the active electron interacting with the Cl/D ions and $r_{1/2}$ is the distance of the electron to the Cl/D nucleus. $V_C(r) = Erf(\alpha r)/r$ is introduced for compensation of the spurs Coulomb interaction when the DCl is in the united atom limit with $r$ being the distance from the electron to the geometrical center. Here $\alpha = 0.48$ is chosen [103, 104]. $V_{Cl}(r_1)$ is calculated from density functional theory with self-interaction correction [105]. With the diatomic molecular model potential the ionization probabilities of DCl in a 5 fs laser field (static field) is calculated by solving the TDSE in spheroidal coordinates [106, 107] with the Cl atom being located in the positive direction of the molecular axis. The orientation dependent ionization probability mimics the $\pi$ orbital electron density with minimum along the molecular axis and maximum in the perpendicular directions. Due to the unbalanced interaction of the electron with the nuclear core, the ionization probability maximizes at about $\theta = 60°$, as shown in Fig. 3.12.

Assuming that the orientation dependent tunneling ionization rates can be expressed as

$$R(\theta, E) = R_1(\theta)R_2(E).$$                (3.14)
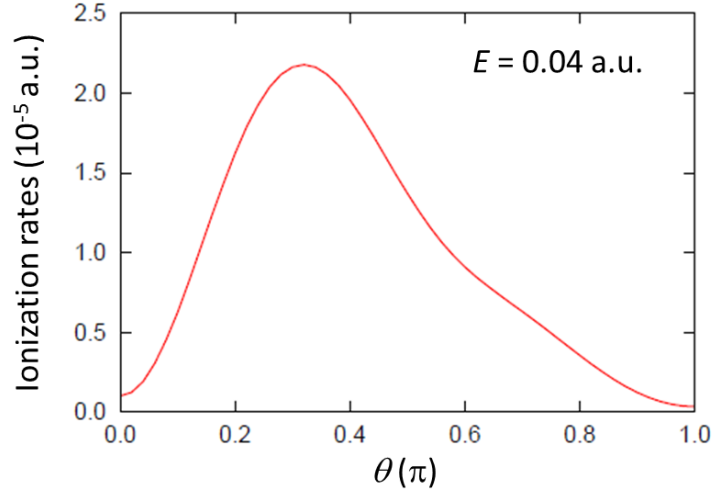
Figure 3.12: The ionization probability of DCl molecule in a 5 fs Gaussian pulse as a function of the angle between the static field and the molecular axis.

Here $R_1(\theta)$ is the orientation dependent part, which is proportional to the ionization probability and $R_2(E)$ is the field strength dependent part, which is calculated by the modified atomic tunneling ionization model [91]. The orientation dependent ionization rates also depend on the laser peak intensity. Thus the total ionization probability of DCl in an oscillating field can be expressed as

$$P(\theta, \varphi) = \int_{-\infty}^{+\infty} R_1(\theta) R_2(E(t)) dt|_{E(t)>0} + \int_{-\infty}^{+\infty} R_1(\pi - \theta) R_2(E(t)) dt|_{E(t)<0}. \qquad (3.15)$$

In this expression, the laser intensity and CEP information is included in $E(t)$, which can be expressed as $E(t) = E_0 f(t) \cos(\omega t + \varphi)$. From a symmetry point of view, the dissociation $DCl^+ \rightarrow D + Cl^+$ occurs through a $\sigma$ orbital, or the HOMO-1 orbital. Since the dissociation is not sensitive to the CEP [56], the dissociation yield on the up/down half-sphere can be calculated as

$$
\begin{aligned}
Y_{up}(\varphi) &= \int_0^{\pi/2} P(\theta, \varphi) \cos^2(\theta) \sin\theta d\theta, \\
Y_{down}(\varphi) &= \int_{\pi/2}^{\pi} P(\theta, \varphi) \cos^2(\theta) \sin\theta d\theta.
\end{aligned}
\qquad (3.16)
$$

Since the major dissociation channel correlates with the HOMO-1, a $\sigma$ state, we assume the dissociation rate is proportional to $\cos^2\theta$. The asymmetry parameter is defined as

$$A(\varphi) = \frac{Y_{up}(\varphi) - Y_{down}(\varphi)}{Y_{up}(\varphi) + Y_{down}(\varphi)}. \qquad (3.17)$$

The rescattering induced double ionization probability can be also estimated as

$$P^{++}(\theta, \varphi) = \int_{-\infty}^{+\infty} R_1(\theta)R_2(E(t))P_{res}(E(t))dt|_{E(t)>0}$$
$$+ \int_{-\infty}^{+\infty} R_1(\pi - \theta)R_2(E(t))P_{res}(E(t))dt|_{E(t)<0}. \tag{3.18}$$

Here $P_{res}$ is the rescattering electron impact ionization probability. The asymmetry parameters from rescattering induced double ionization can be obtained from $P^{++}(\theta, \varphi)$.

## 3.3.2   Experimental results and discussions
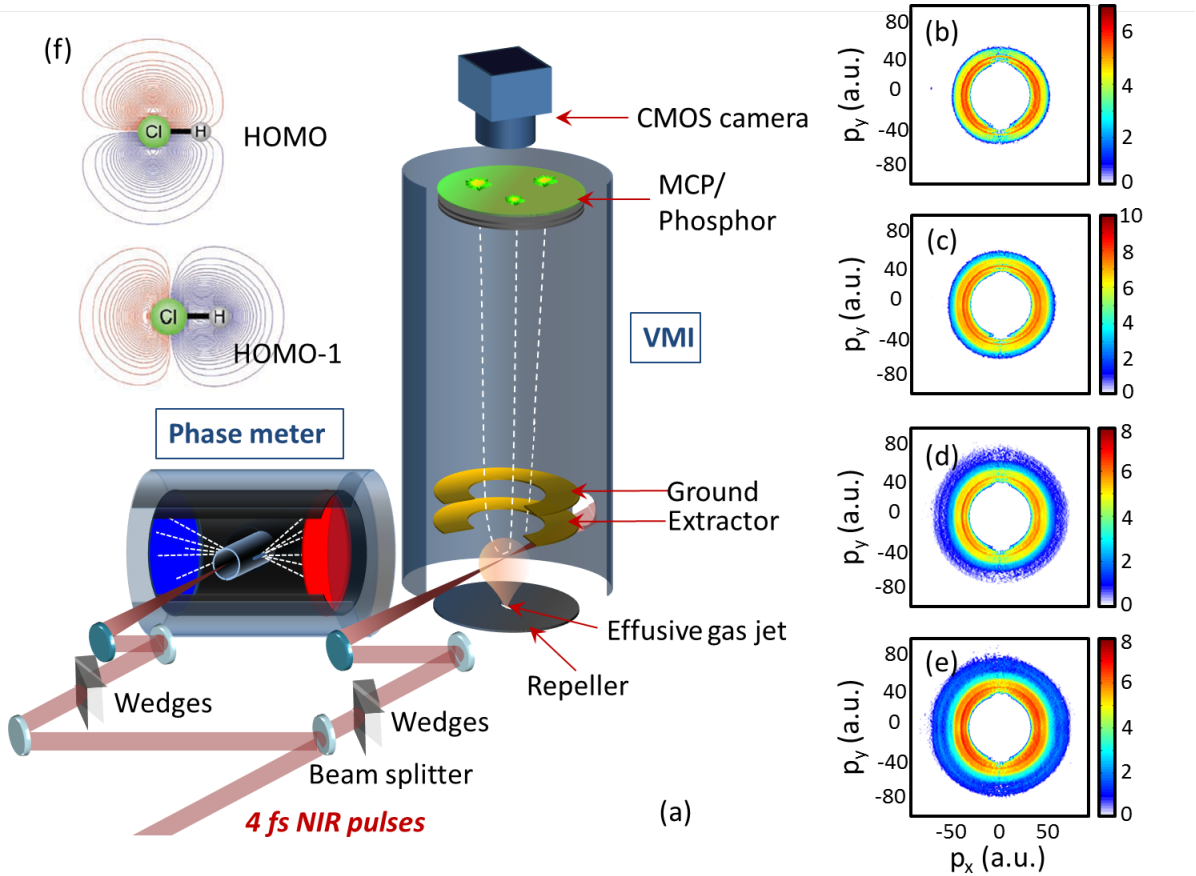


Figure 3.13: (a) A schematic drawing of the experimental setup (a CEP-tagged single-shot VMI system). (b-e) CEP-averaged momentum distributions of $D^+$ ions from the dissociative ionization of DCl with 4 fs pulses at 720 nm at intensities of (1.3, 1.9, 2.5 and 3.1)$\times 10^{14}$ W cm$^{-2}$, respectively. Note that the intensity uncertainty is about $\pm 20\%$. (f) The 2D representations of the HOMO and HOMO-1 of DCl (taken from Ref. [81]).
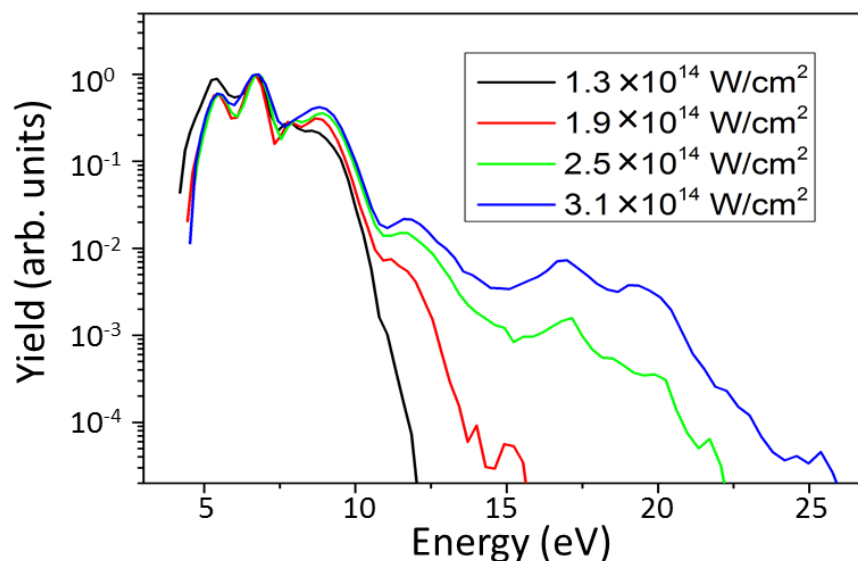
Figure 3.14: The kinetic energy spectra for $D^+$ (DCl) for the intensities of (1.3, 1.9, 2.5 and 3.1)$\times 10^{14}$ W cm$^{-2}$, respectively. The spectra are normalized to the peak at 6.8 eV, which is the strongest peak observed. (Adapted from Ref. [102])

The experimental setup is shown in Fig. 3.13 (a). An effusive molecular beam of DCl was injected into the VMI chamber through a hole at the center of the repeller plate and interacted with a beam of 4 fs NIR pulses. The laser intensity was adjusted by a rotatable neutral density filter and the peak intensities were estimated from measuring the ATI electron emission from Xe gas under identical experimental conditions. By rotating a neutral density filter, the focusing geometry can be fixed and the influence on the CEP is negligible. The $D^+$ ions resulting from the laser-target interaction were detected by the single-shot VMI spectrometer and were sorted by the corresponding CEPs obtained from the steoro-ATI phase meter. Fig. 3.13 (b-e) show the CEP-averaged momentum maps for $D^+$ ions obtained at intensities of (1.3, 1.9, 2.5 and 3.1)$\times 10^{14}$ W cm$^{-2}$, respectively. These images are Abel-inverted [50] and show the momentum distributions at the plane of $p_z = 0$.

On the momentum maps, the signal below 8 a.u. (about 0.2 eV in kinetic energy) was mainly from the neighboring $H^+$ signal due to the close time of flight, therefore was discarded from the images. Our results at the lowest intensity, i.e. $1.3 \times 10^{14}$ W cm$^{-2}$, was similar to what was observed in a previous study [56] under similar experimental conditions. A few sharp rings are visible in the momentum maps as shown in Fig. 3.13 (b-e), which indicate contributions from different excited states of DCl$^+$. The 2D representations of the HOMO and the HOMO-1 of HCl molecule are shown in Fig. 3.13 (f). The orbitals of DCl are similar to that of HCl. The HOMO represents a $\pi$-orbital with its maximum perpendicular to the molecular axis. While the HOMO-1 represents a $\sigma$-orbital which maximizes along the molecular axis. The angular distribution of $D^+$ peaks at around 60°
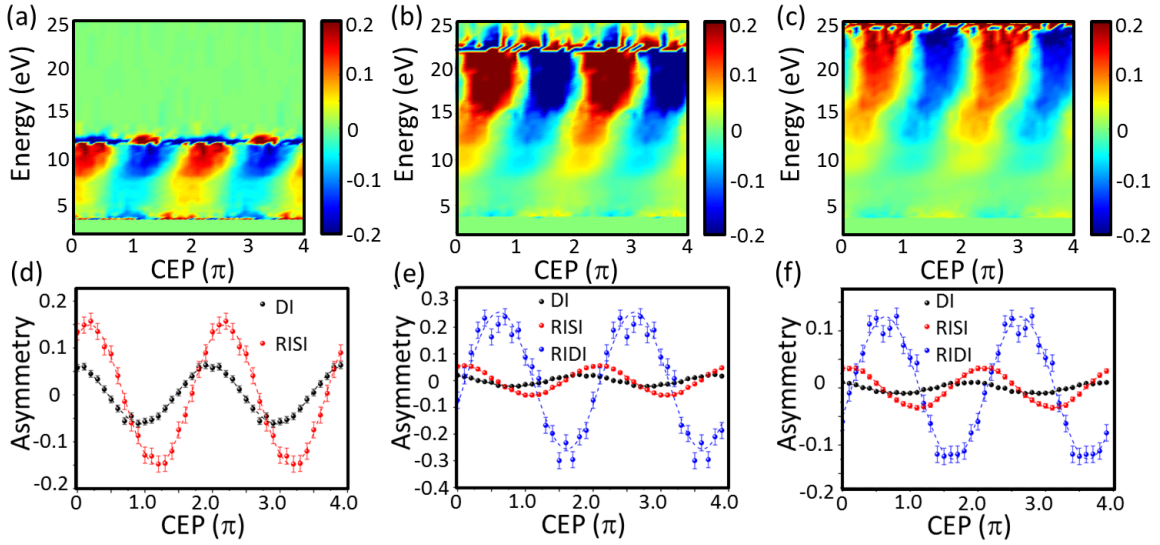
Figure 3.15: (a-c) Asymmetry maps of $D^+$ ions as a function of CEP and kinetic energy at intensities of (1.3, 2.5 and 3.1)$\times 10^{14}$ W cm$^{-2}$, respectively. (d-f) The corresponding kinetic energy integrated asymmetry parameters at the above laser intensities as a function of CEP for the direct ionization (DI), the rescattering induced single ionization (RISI), and the rescattering induced double ionization (RIDI) regions, respectively. The bullets are experimental data while the dashed curves are the fitting results to a cosine function. (Adapted from Ref. [102])

with respect to the laser polarization direction, which agrees nicely with the expectations for the tunneling ionization from the degenerate HOMOs of DCl (which is shown in Fig. 3.12). With increasing laser intensities, $D^+$ ions with higher momenta (above 60 a.u.) are obtained.

By integrating the ion signal within an angular range of $\pm 20°$ with respect to the y-axis, kinetic energy spectra are obtained and are shown in Fig. 3.14. The ion yield extends to higher kinetic energy for higher laser intensities and the peak height for the high energy region (above 15 eV) increases with intensity. For strong field interaction, highly excited dissociative states of the molecular ion can be populated by recollisional excitation. The maximum recollision energy can be estimated as 3.17 $U_p$ from classical calculation. For the intensity range we explored, a maximum recollision energy of about 20 eV (1.3$\times 10^{14}$ W cm$^{-2}$) to 47 eV (3.1$\times 10^{14}$ W cm$^{-2}$) can be obtained which is efficient for the population of the excited states of DCl$^+$.

Similar to the analyzing approach for the case of $D_2$, the directional emission of $D^+$ ion from DCl was investigated by the experimental asymmetry parameter $A_{exp}(\varphi, E)$. The asymmetry maps as a function of CEP and kinetic energy are shown in Fig. 3.15. In contrast to the previous results reported in Ref. [56], the oscillation of the asymmetry parameter is kinetic energy dependent at the intensity of 1.3$\times 10^{14}$ W cm$^{-2}$ shown in
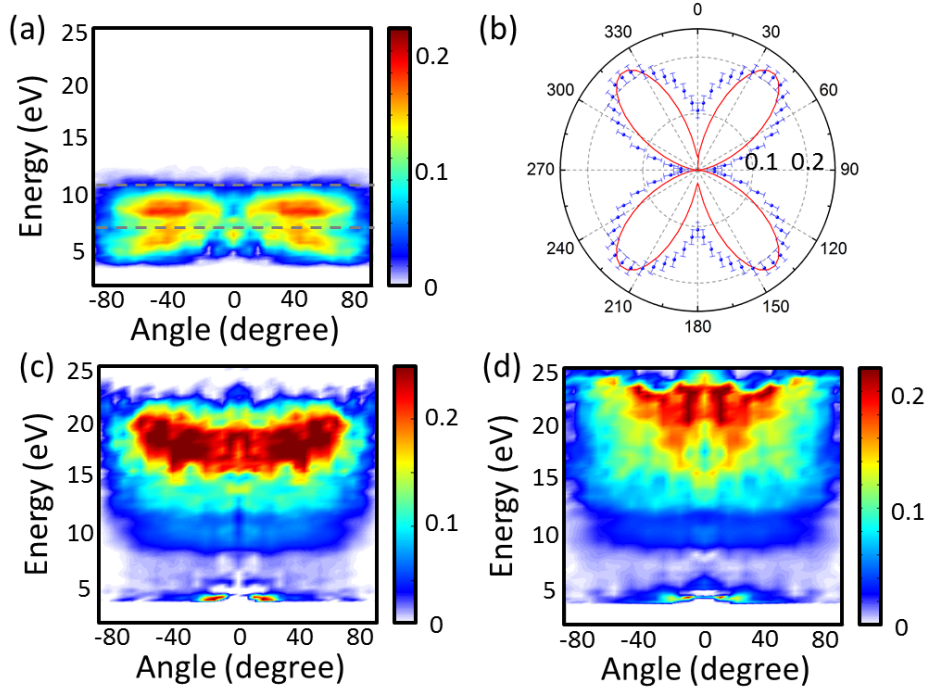
Figure 3.16: (a, c, d) Distribution of the absolute value of the asymmetry amplitude as a function of angle and kinetic energy at intensities of (1.3, 2.5 and 3.1)$\times 10^{14}$ W cm$^{-2}$, respectively. (b) Polar plot of the energy integrated asymmetry (the integration range is indicated by the grey dashed lines in (a)) derived from (a)(blue scattered bullets) and the calculated ionization probability (red solid curve) from the HOMOs of DCl. (Adapted from Ref. [102])

Fig. 3.15 (a). Two regions can be distinguished, i.e. 5-7 eV and 7-11 eV, with different asymmetry amplitudes and a phase offset between them. This can be clearly seen in the kinetic energy integrated asymmetry parameters shown in Fig. 3.15 (d). We assign the first region (5-7 eV) to dissociation involving the X-state of DCl$^+$, which is populated through direct ionization (DI) with the laser field. The asymmetry oscillation in this region peaks at around CEP=0. The second region (7-11 eV) might originate from dissociation involving the A-state of DCl$^+$, populated by rescattering induced single ionization (RISI). With the intensity increasing, a third region with higher kinetic energy (above 12 eV) is observed for the intensities of 2.5 and 3.1$\times 10^{14}$ W cm$^{-2}$ as shown in Fig. 3.15 (b,c). This region exhibits higher asymmetry amplitude up to about 30% and maximizes at around CEP=$2\pi/3$. This specific phaseshift is an indication of a rescattering induced double ionization (RIDI) process [108, 109, 110].

For better understanding, the angular distributions of the asymmetry amplitude as a function of kinetic energy are ploted in Fig. 3.16 (a,c,d). The three regions mentioned above can be differentiated in these plots with characteristic angular distributions. For the

lowest intensity, the angular distribution within an energy range of 7-11 eV is integrated and plotted in Fig. 3.16 (b) for comparison with the earlier study [56]. This butterfly shape resembles the orientation-dependent ionization probability of the HOMOs of DCl and generally agrees with what was reported in Ref. [56].

As shown in Fig. 3.15 (d-f), the amplitude of the asymmetry oscillation for the DI region becomes smaller as the intensity increases, and the maximum is shifted towards smaller CEPs. Our simulation can reproduce a similar trend for the amplitude, but with smaller absolute values [102]. Similar to the mechanism mentioned for the case of $D_2$ in Section 3.2.3, for efficiently high laser intensities, the molecular ion can be dissociated at any CEP, thus the asymmetry amplitude will decrease for higher intensities. The higher asymmetry parameters obtained from the experiment might originate from the processing of the experimental data by removing a large background signal.

As estimated by the simulation, the probability of rescattering-electron-induced double ionization compared to that of the dissociative single ionization for the intensities of 1.3, 1.9 and $2.5 \times 10^{14}$ W cm$^{-2}$ are 7, 5 and about 2-3 orders smaller, respectively. Thus the RIDI channel for intensities below $2 \times 10^{14}$ W cm$^{-2}$ is negligible. For higher intensities above $2 \times 10^{14}$ W cm$^{-2}$, the contribution of the RIDI channel to the asymmetry is dominating for the high energy region. As indicated in Ref. [102], the simulation can reproduce the tendency for the asymmetry amplitude for this channel but with some discrepencies on the phase offset. The main reason is that the theory model is too simple for this complex system. In our simulation, the average return time and return energy were calculated with semi-classical trajectories. For low intensities, the return time and energy are sharper thus can be estimated with higher accuracy. However, for high intensities, the returning electrons exhibit a broad distribution in energy and reliable cross section information is required to model the process accurately, which was not available.

# 3.4 Sub-femtosecond Steering of proton migration in hydrocarbons

When interacting with an intense laser field, the geometrical structure of molecules can be strongly deformed and resulting in a variety of characteristic dynamical processes. Among them, controlling the motion of a hydrogen atom, or proton, has attracted much attention in the field of physics and chemistry. Hydrogen migration which causes chemical bond rearrangement can open new reaction pathways and can help to develop new techniques for controlling chemical-bond breaking and formation. A lot of studies on the proton migration processes in many hydrocarbons using ultrashort laser pulses have been carried out in recent years, such as the work presented in Ref. [77, 78, 79, 80]. The laser pulses being utilized were mostly multi-cycle NIR pulses and the characteristic time scale for hydrogen migration to occur was demonstrated to be tens of femtoseconds. A recent study on the attosecond steering of deprotonation process in acetylene using CEP-resolved few-cycle pulses, showed that the underlying mechanism is due to the control over the superposition of vibrational modes, rather than the control over the electronic degrees of freedom [76]. We expect this control mechanism to be a general scheme. Even though the proton migration process occurs on a much longer time scale compared to the duration of few-cycle pulses, it is still possible to manipulate the migration by initiating the process and letting the system evolve in a field-free environment afterwards. Here, we demonstrate the control of hydrogen migration in allene and toluene using tailored few-cycle NIR laser pulses. Allene is selected as a candidate due to its large $H_3^+$ yield in ultrashort intense laser fields [111]. Toluene serves as a prototype system for asymmetric aromatic hydrocarbons. For both hydrocarbon molecules, the fragment ions which are generated through proton migration are monitored using single-shot VMI spectroscopy and the resulting asymmetry maps show clear CEP-dependent control on their directional emission. The results can be interpreted by a quantum dynamical model [76], which can be generalized to both deprotonation and isomerization processes in complex molecules.

## 3.4.1 Theoretical approach

Quantum dynamical simulations was conducted for allene by the group of Prof. Regina de Vivie-Riedle. This theory model has been successfully applied for acetylene and interpreted that the steering of deprotonation from acetylene by changing the CEP of a few cycle pulse is from the novel femtosecond control on the superposition of vibrational degrees of freedom [76]. In a recent work, the theorerical model introduced in Ref. [76] has been generalized to calculate both deprotonation and isomerization, and has been applied to the more complex allene molecule [82, 83]. Acetylene is a molecule with linear geometry, thus the simulation of the nuclear motion on a 2D potential energy surface (PES) has been proven to be sufficient. However, the situation is more complicated for allene. There are two consecutive carbon double bonds in allene and the four hydrogen atoms are lying in different planes, as shown in Fig. 3.17. The two hydrogen atoms on one end are on a

plane which is perpendicular to that of the other two hydrogens on the other end. This leads to the necessity of conducting the calculation in 3D, which dramatically increases the difficulty for the modelling. For the case of toluene, the required computations are beyond the present theoretical capabilities.

The quantum dynamical behavior of allene is calculated on an *ab initio* PES. The neutral ground state $X^1\Sigma$, the cation ground state $X^2\Pi$ and first excited state $A^2\Pi$, the dication ground state $X^3\Sigma$ and first excited state $A^3\Pi$, and even the second excited state of the dication $B^3\Pi$ have been included. The PESs, the dipole moments, and transition dipole moments have been computed at the CASSCF [4,4], [3,4], and [2,4] level of theory for neutral, cationic and dicationic states, respectively. The 6-31++G** basis set was used. Three dimensions were needed for allene, including the HCH rocking mode, the symmetric and anti-symmetric HCH bending modes. The 3-D PES was interpolated to a $128 \times 128 \times 128$ grid with a step size of 0.05 a.u..
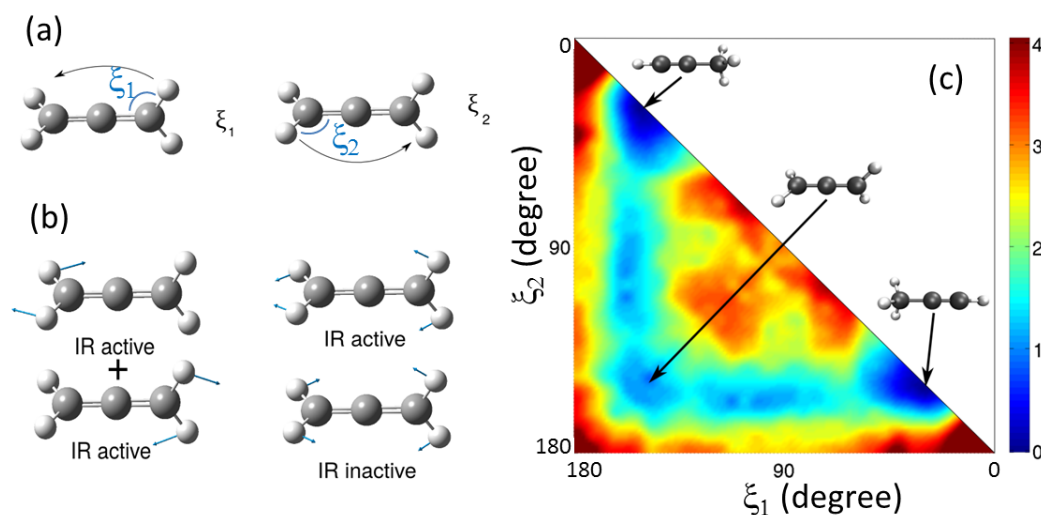


Figure 3.17: (a) Definition of the reactive coordinates ($\xi_1$ and $\xi_2$) and (b) normal modes used in the theoretical investigation of the hydrogen migration in allene. (c) The potential energy surface (PES) for the $B^3\Pi$ state of the allene dication. The binding energy is plotted as a function of the two reactive coordinates. (Courtesy of Robert Siemering.)

It is possible to describe the isomerization dynamics in the excited dicationic states on the 2D PES for allene, which makes the theory part feasible. The PES was represented along two reactive coordinates, i.e. $\xi_1$ and $\xi_2$, which describe the pathway towards isomerization (see Fig. 3.17 (a)). $\xi_1$ illustrates the H migration from right to left, and $\xi_2$ is for the opposite direction. To calculate the isomerization, the wavepacket $\Phi_{modes}$ expressed in normal modes (see Fig. 3.17 (b)) is projected onto the wavepacket $\Phi_{reac}$ expressed in reaction coordinates. The projection is performed via the respective eigenfunctions of the

dication groundstate, and can be expressed as

$$\varphi_{reac} = \sum_{i,j} \langle \Phi_{modes} \mid \Phi_i \rangle \langle \Phi_i \mid \varphi_j \rangle \mid \varphi_j \rangle \qquad (3.19)$$

with $\Phi_i$ the eigenfunctions in normal modes and $\varphi_j$ the eigenfunctions in reactive coordinates. The final excited state is the $B^3\Pi$ for allene and the PES is shown in Fig. 3.17 (c). This state has no global minima in the Franck-Condon region. A very shallow local minimum can be reached. From the isomerization minima, dissociation can take place. The kinetic energy of the wavepacket is enough to overcome the small barrier. The calculation is very complex for allene since the reactive coordinates ($\xi_1$ and $\xi_2$) are a linear combination of eight normal modes. But the stretching modes are not relevant for the initial part of the isomerization, only four bending modes are considered for the formation of the initial wavepacket in the laser field. Among these four modes, two of them are degenerate, therefore the calculation can be dramatically reduced. In this configuration, the laser pulse populates the two IR active modes $\mid n_1 00 \rangle$ and $\mid 0n_2 0 \rangle$ and imprints the CEP on them. The last mode $\mid 00m \rangle$ will be populated in the cation by the first ionization step forming a wavepacket $\mid 00m \rangle + e^{-i\theta}(\mid n_1 00 \rangle + \mid 0n_2 0 \rangle)$. This wavepacket provides the possibility for the directional control of the isomerization, which occurs on the reactive $B^3\Pi$ state in the dication.

The interaction of the molecule with the external laser field is calculated by solving the TDSE using the Chebychev propagator. The TDSE for the neutral molecule can be expressed as

$$(H_n + \mu_{nn}\varepsilon(t))\Psi_n(t) = \Psi_n(t) \qquad (3.20)$$

with $H_n$ the Hamiltonian of $X^1\Sigma_g^+$, $\mu_{nn}$ the associated dipole moment and $\varepsilon(t)$ the near-single cycle laser field. The light field is $\varepsilon(t)$ was included in the dipole approximation:

$$\varepsilon(t) = E_0 \exp\left[-\left(\frac{t - t_1}{FWHM/\sqrt{2ln2}}\right)^2\right]\cos[\omega_0(t - t_1)]. \qquad (3.21)$$

Here a pulse with 4 fs full width at half maximum (FWHM) was used. The light field was discretized with a time step of 0.024 fs. The part of the laser interaction experienced by the neutral molecule has a duration of 4.8 fs corresponding to the time when the intensity maximum is reached and the system is ionized. During this period the initial superposition is formed. All the ionization steps are approximated by setting the vibrational wavepacket onto the corresponding ionic state.

In the first ionization step, the vibrational wavepacket of the neutral molecules is transferred to the lowest cationic states. The first two electronic states ($X^2\Pi$ and $A^2\Pi$) of the cation are very close in energy, thus an equal population of both states during the first ionization step is assumed. The TDSE for the cation reads:

$$\begin{pmatrix} H_1 + \mu_{11}\epsilon(t) & 0 \\ 0 & H_2 + \mu_{22}\epsilon(t) \end{pmatrix} \begin{pmatrix} \Psi_1(t) \\ \Psi_2(t) \end{pmatrix} = \begin{pmatrix} \Psi_1(t) \\ \Psi_2(t) \end{pmatrix}, \qquad (3.22)$$

where $H_1$ and $H_2$ are the Hamiltonians of the $X^2\Pi$ and $A^2\Pi$ states of the cation, $\mu_{11}$ and $\mu_{22}$ are the associated dipole moments. The isomerization of the wavepacket in the respective excited triplet state of the dication was propagated for 480 fs with a time step of 0.24 fs. The part of the wavepacket corresponding to the left/right isomerization is quantified by the integration over the propagation time. Subsequent dissociation is assumed to be proportional to the part of the wavepacket at the isomerization minimum with the same dissociation probability.

## 3.4.2   Experimental results and discussion

Experimentally, the momentum distribution of $H_3^+$ fragments from allene and $CH_3^+$, $H_2^+$, $H_3^+$ fragments from toluene interacting with intense few-cycle pulses are measured utilizing the CEP-tagged single-shot VMI system. The generation of $H_3^+$ from allene and $H_2^+$, $H_3^+$ from toluene indicate proton migration to happen without the necessity of a coincidence measurement. For allene, we found clear CEP-dependence of the directional emission of $H_3^+$ which demonstrates control over proton migration with 4 fs pulses. Similar measurements are carried out for toluene and the results also show asymmetry in the directional fragment emission. Our experimental work indicates the general importance of the control mechanism for larger molecules.

**Allene**

The experimental setup is similar to what was introduced in Section 3.2 and 3.3. The allene gas (from Sigma Aldrich, Model 294985, 97% in purity) was injected through the diffusive gas jet into the VMI chamber. We used a decoupling box connecting to the MCPs to get the TOF signal, which is shown in Fig. 3.18. A series of fragments can be distinguished as marked in the figure. Among them, we focus on $H_3^+$, which can be formed mainly through hydrogen migration. Actually, propyne (or named methylacetylene, with the chemical formula $CH_3C{\equiv}CH$) exists in equilibrium with allene at room temperature. It is in principle possible that the $H_3^+$ is formed from the $CH_3$ moiety in the isomer without proton migration. However, studies on the deuterium tagged isomer methyl-d₃-acetylene ($CD_3CCH$) in intense laser fields showed that it is more probable for migration to occur when the multi-hydrogen fragment ions are formed [112, 113]. We also conducted a coincidence measurement utilizing a REMI or COLTRIMS (COLd-Target Recoil-Ion-Momentum Spectroscopy) [114, 115]. The results show clear coincidence lines and indicate that the formation of $H_3^+$ from our sample after interaction with 4 fs pulses is mainly through the reaction pathway $C_3H_4 \rightarrow H_3^+ + C_3H^+$ (shown in Fig. 3.19 (a)). Based on this, we studied the hydrogen migration in allene with 4 fs NIR pulses by detecting the $H_3^+$ ions without coincidence using phase-tagged single-shot VMI.

Since the count rate is very low for $H_3^+$, as can be seen in the TOF spectrum in Fig. 3.18, a configuration with high target density and low laser intensity (around $0.8 \times 10^{14}$ W cm$^{-2}$) was used to maintain enough signal statistics and to avoid space charge effects. Besides, a long acquisition time up to several hours is required. An asymmetry oscillation
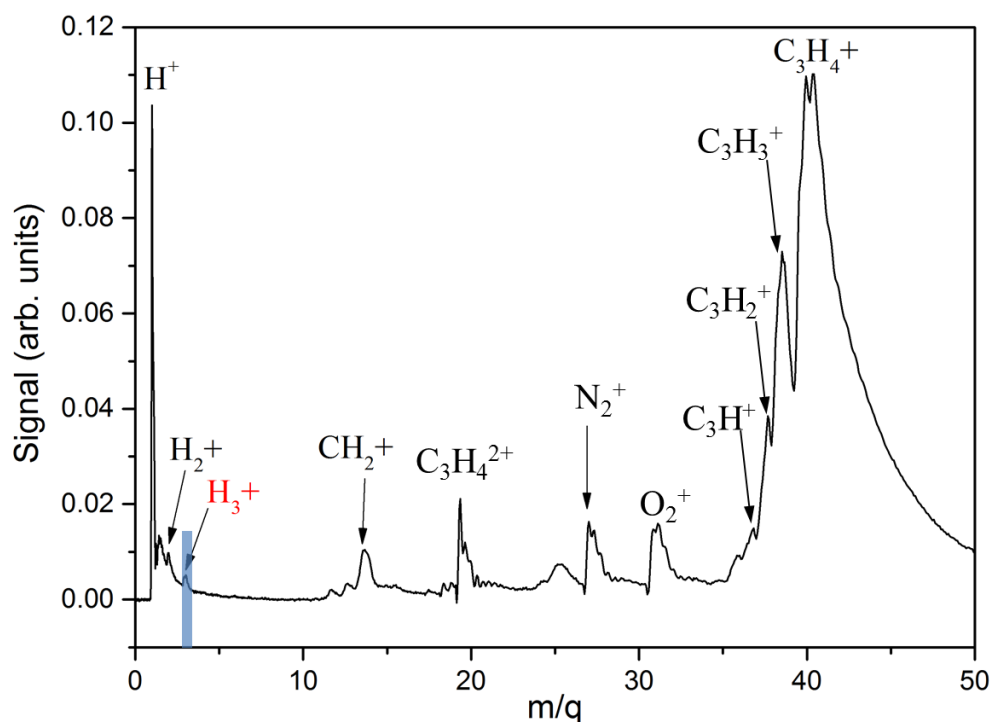
Figure 3.18: Time of flight (TOF) spectrum from allene when interacts with 4 fs NIR pulses at an intensity about $1 \times 10^{14}$ W cm$^{-2}$.

is obtained for $H_3^+$ for a certain kinetic energy range and is shown in Fig. 3.19 (c). The oscillation can be seen more clearly in the kinetic energy integrated asymmetry parameters plotted in Fig. 3.19 (d). This indicates ultrafast control of hydrogen migration in allene with few-cycle pulses. The kinetic energy spectrum (shown in Fig. 3.19 (b)) shows a single peak structure and the maximum at around 3.5 eV, which agrees well with former studies [112] and a comparing measurement using COLTRIMS in our group [82, 83]. The CEP-dependent ion emission maximizes around the peak of the energy distribution. The energy integrated asymmetry oscillation is fitted with a cosine function and an amplitude of about 2.5% is obtained. There are several reasons for such a small amplitude. First, without coincidence measurement, the $H_3^+$ signal from many fragmentation pathways may lead to smearing of the asymmetry oscillation. Second, we have found that the oscillation of the asymmetry parameter is highly dependent on laser intensity [83]. Actually, the phase of the asymmetry oscillation could rapidly vary by slightly changing the laser intensity. Therefore, the results obtained from VMI measurement can be washed out easily due to the focus volume averaging effect. Nevertheless, our results demonstrate the ultrafast control of hydrogen migration in allene with few-cycle pulses.

Theoretically, the isomerization of allene is investigated for double ionization processes. In sequential double ionization, the second step takes place at the global intensity maximum and the first ionization happens either at the same maximum, a half-cycle or a full cycle earlier. For recollision induced double ionization the first ionization occurs at the intensity
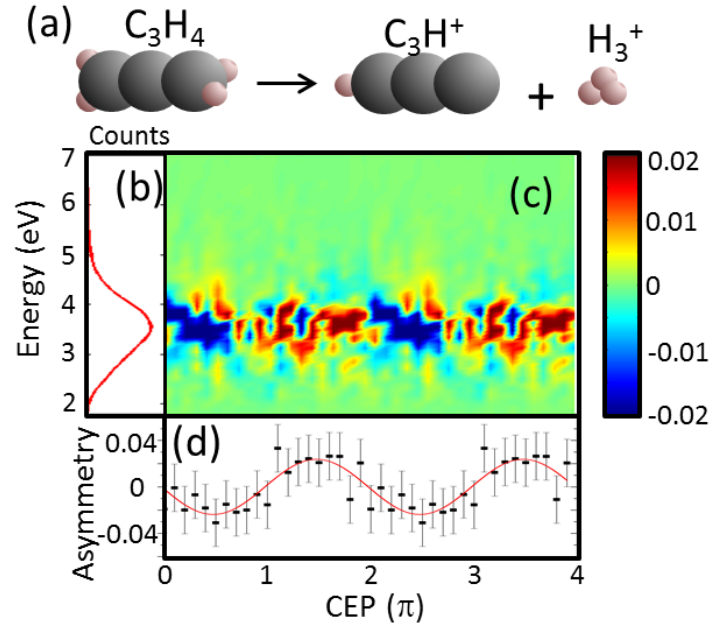
Figure 3.19: (a) An illustration of the formation process of $H_3^+$ from allene. (b) The kinetic energy spectrum for $H_3^+$ from allene when interacting with 4 fs NIR pulses at an intensity of $(0.8\pm0.2)\times10^{14}$ W cm$^{-2}$. (c) The asymmetry parameter of $H_3^+$ emission as a function of kinetic energy and CEP for the above experimental condition. (d) Energy integrated asymmetry parameter (black bullets) and the fitting result (red solid curve) to a cosine function.

maximum and the second ionization occurs about a three quarter period later. Simulation results show clear asymmetry oscillation for $H_3^+$ in a 4 fs laser field and indicate that the different emission time of the first and the second electron will affect the phase of the resulting asymmetry oscillations [83].

Since the observed asymmetry parameter exhibits very small amplitudes, a statistical test was performed to demonstrate that the observed asymmetric oscillation is not an artifact [76]. The basic idea is to check the asymmetry curves after reordering the single shot VMI images with respect to the detected CEPs. In principle, if the two events associated are not from the same laser pulse, there will be no correlation between them and the resulting asymmetry parameters will not show an oscillation with a period of $2\pi$. We calculated the asymmetry for 50 testing data sets which are generated by shifting the sequence of the VMI images with respect to the CEP data by random steps. Afterwards, the asymmetry oscillations are fitted with a cosine function and the fitted asymmetry amplitude and adjusted R-square parameter are compared with those from the original data. The adjusted R-square parameter evaluates the goodness of the fitting model, and
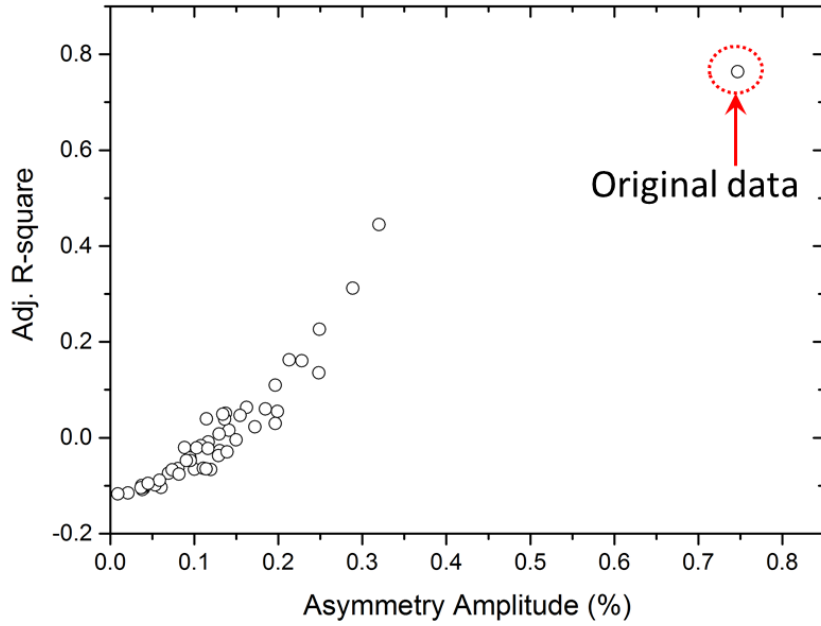
Figure 3.20: Statistical testing of the asymmetry. The CEPs of the measured data are randomized and the resulting asymmetry curves are fitted with a cosine function. The extracted asymmetry amplitude and the adjusted R-square parameter are plotted for 50 testing points. The original experimental data is pointed out in a red dashed circle, which demonstrates that the observed asymmetry oscillation is statistically significant.

is defined as

$$R^2_{adj.} = 1 - \frac{\sum\limits_{i=1}^{n}[A(\phi_i) - \hat{A}(\phi_i)]^2/(n-m)}{\sum\limits_{i=1}^{n}[A(\phi_i) - \bar{A}]^2/(n-1)}. \tag{3.23}$$

Here, $A$ is the measured asymmetry parameter, $\hat{A}$ is the fitted asymmetry parameter, and $\bar{A}$ denotes the mean value of asymmetry over all the data points. $n$ is the number of total sample size, and $m$ is the number of the fitted coefficients. The adjusted R-square parameter $R^2_{adj}$ is derived from the $R^2$ parameter and is corrected with the degrees of freedom. It can take any values from 0 to 1, with 1 indicating the best fitting. As shown in Fig. 3.20, the original data exhibits higher asymmetry amplitude and higher adjusted R-square value which can be well distinguished from the other testing data sets. This indicates that the observed asymmetry oscillation, although with tiny amplitude, is statistically significant.

To conclude, our results demonstrate that the proton migration dynamics in allene can be steered by 4 fs CEP-controlled few-cycle pulses. The underlying control mechanism, from a quantum dynamical model, is due to the manipulation of the phases in the vibrational wavepackets when they superimpose. Although the asymmetry amplitude obtained

in the present experimental condition is small, this work can initiate future investigations and the degree of control can be improved by optimizing several parameters, such as the laser intensity, pulse duration, wavelength *etc.*.

**Toluene**

Toluene is a prototype system for asymmetric aromatic hydrocarbons. When interacting with intense few-cycle pulses, the formation of several fragment ions could involve the breaking of C-H bonds and forming of new bonds between the hydrogen atoms within the transient structure of the multiply charged precursor. The momentum distributions of $H_2^+$, $H_3^+$ and $CH_3^+$ fragment ions are monitored as a function of CEP and laser intensity in few-cycle laser fields. Here, the $CH_3^+$ fragment is studied along with the molecular hydrogen fragments, providing a reference for a simple C-C bond breaking process without the proton migration step.

The experimental setup is similar to what was used for the measurement of allene. Vaporized toluene (>99.8% purity, Sigma-Aldrich) enters the VMI chamber through a differential pumping chamber. Before arriving in the laser-matter interaction region, the gas passes through a skimmer with an opening of 0.5 mm in diamter. The pressure in the differential pumping chamber is kept below $10^{-5}$ mbar during data acquisition to maintain a continuous pure toluene molecular beam which interacts with the laser pulses without contribution of clusters. A cold-trap is installed downstream of the toluene source to reduce pollution in the experimental chamber.

The CEP-averaged momentum distributions in the plane of $p_z = 0$ of the $CH_3^+$ and $H_2^+$ fragments are presented in Fig. 3.21 for three laser intensities, i.e. (0.8±0.1, 1.1±0.1, and 1.5±0.1)×$10^{14}$ W cm$^{-2}$, respectively. The corresponding kinetic energy spectra are shown in Fig. 3.22. The VMI images of $CH_3^+$ exhibit a bimodal profile, consisting of two components centered at about 1.7 eV and 4.0 eV, respectively. The lower energy component (at 1.7 eV) exhibits an isotropic angular distribution which is attributed to two-body dissociation channel involving a metastable dication state on a microsecond timescale [116]. The component at 4.0 eV involves ions ejected preferentially along the laser polarization axis which indicates a fast process. Recent work by Kaziannis *et al.* carried out on deuterium marked toluene in asymmetric two-color laser field showed that the 4.0 eV component is absent in the energy spectra of $CD_3^+$ and $CHD_2^+$ fragments which involves a hydrogen and deuterium exchange process [117]. Therefore the $CH_3^+$ fragments with kinetic energy around 4.0 eV should originate from precursors that dissociate with a faster rate compared to hydrogen migration. For the $H_2^+$ fragment, the corresponding kinetic energy spectra are shown in Fig. 3.22 (b) for the three intensities. Besides the ion signal centered around 2.4 and 4.2 eV, higher energy fragments around 7.5 eV are obtained. These high kinetic energy $H_2^+$ fragments indicate the formation of higher charge number parent ions which can be supported by the intensity dependence of the peak height. We also carried out measurements on toluene with circular polarized pulses at twice the intensity as the linear case (0.8×$10^{14}$ W cm$^{-2}$), and the spectra are shown with dashed curves in Fig. 3.22. Comparing the black dashed curve with the red solid curve, which corresponds to the same
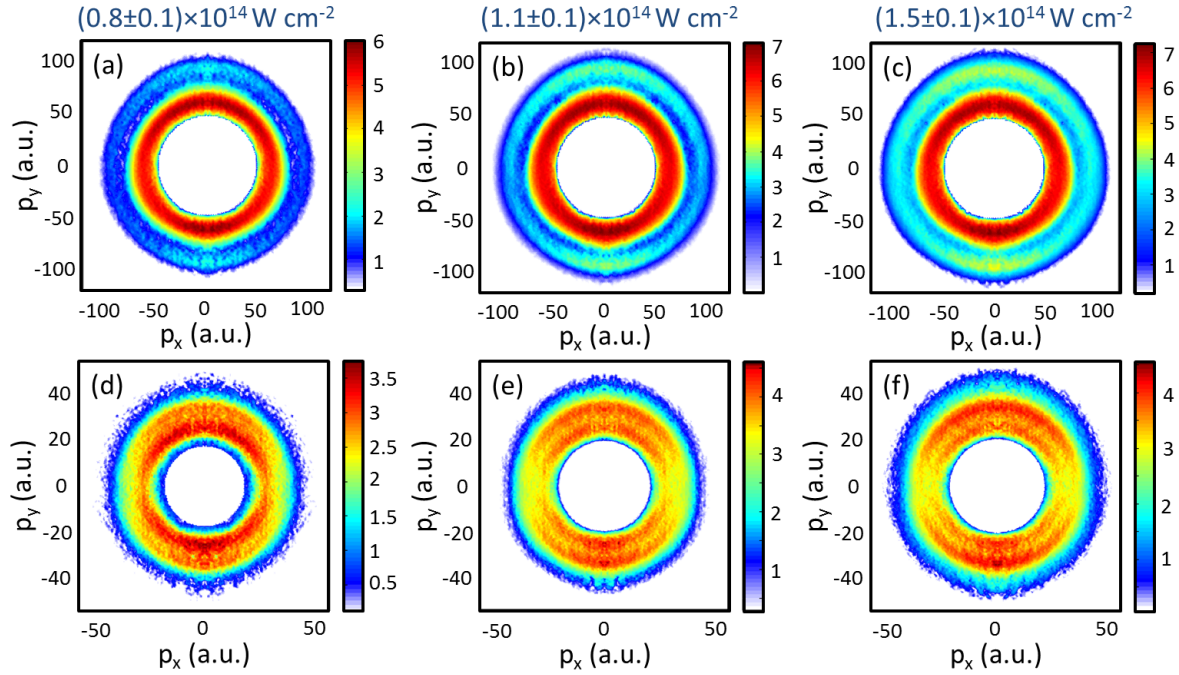
Figure 3.21: CEP-averaged momentum distributions of (a-c) $CH_3^+$ and (d-f) $H_2^+$ ions in a 4 fs linear polarized laser field at intensities of (0.8±0.1, 1.1±0.1, and 1.5±0.1)×$10^{14}$ W cm$^{-2}$, respectively.

peak laser intensity for circular and linear polarization cases, they show similar spectral structure especially for the high energy part. Note that the data for circular polarization were not inverted due to the restriction of symmetry.

The asymmetry maps for $CH_3^+$ and $H_2^+$ are shown in Fig. 3.23 (a, b) at an intensity of (1.1±0.1)×$10^{14}$ W cm$^{-2}$. For $CH_3^+$, the asymmetry oscillation exhibits a jump at a kinetic energy slightly below 4 eV, which agrees with the division of the two spectral peaks. The difference in both amplitude and phase offset for these two regions can be clearly distinguished by the energy integrated asymmetry parameters which are shown in Fig. 3.23 (c). The asymmetry map for $H_2^+$ exhibits gradual changes in both asymmetry amplitude and phase as shown in Fig. 3.23 (b) and (d). The asymmetry parameter also shows intensity-dependence. To illustrate this, a fitting function $A(\varphi) = A_0 \cdot \cos(\varphi + \varphi_0)$ is used with $A_0$ the asymmetry amplitude and $\varphi_0$ the phase offset. The energy integrated asymmetry oscillations are fitted by this function and the results for different intensities are shown in Table 3.2 and Table 3.3. A decrease in the phase offset for the highest energy range (7-8 eV) of $H_2^+$ from about 2.7 to 1.8 rad is observed when the intensity is increased from 0.8 to 1.1×$10^{14}$ W cm$^{-2}$, while the other peaks are less affected by intensity change. For $CH_3^+$ the high energy peak shows no clear intensity-dependence in the phase offset.

We also measured the directional emission of $H_3^+$ from toluene at an intensity of (1.1±0.1)×$10^{14}$ W cm$^{-2}$ and the results are shown in Fig. 3.24. Clear asymmetry os-
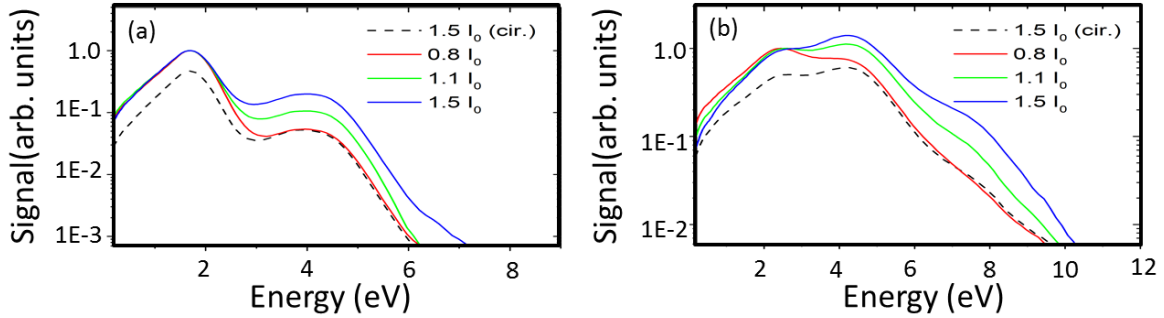
Figure 3.22: Kinetic energy spectra for (a) $CH_3^+$ and (b) $H_2^+$ ions for linear polarization at intensitites: $(0.8\pm0.1, 1.1\pm0.1,$ and $1.5\pm0.1)\times10^{14}$ W cm$^{-2}$, and for circular polarization at the intensity of $(1.5\pm0.1)\times10^{14}$ W cm$^{-2}$. The spectra are nomalized to the peak at around 2 eV. (Adapted from Ref. [84])

cillation is obtained and shown in Fig. 3.24 (b) and (c). The generation of $H_3^+$ requires the breakup of two C-H bonds and the formation of a new $H_3^+$ moiety in a multiply charged precursor prior to its dissociation.

Table 3.2: The fitting results of asymmetry amplitude $A_0$ (in the unit of %) of $CH_3^+$ and $H_2^+$ fragments for the indicated energy ranges and intensities.

| Intensity($10^{14}$W cm$^{-2}$) | | $(0.8\pm0.1)$ | $(1.1\pm0.1)$ | $(1.5\pm0.1)$ |
|---|---|---|---|---|
| $H_2^+$ | (2-3) eV | $2.4\pm0.2$ | $2.0\pm0.2$ | $1.1\pm0.2$ |
| | (4-6) eV | $3.1\pm0.2$ | $2.2\pm0.2$ | $1.4\pm0.2$ |
| | (7-8) eV | $4\pm1$ | $4.9\pm0.7$ | $2.9\pm0.5$ |
| $CH_3^+$ | (1.5-2.5) eV | $0.7\pm0.1$ | $0.5\pm0.1$ | $0.2\pm0.1$ |
| | (4.5-6) eV | $2.7\pm0.3$ | $2.1\pm0.3$ | $0.7\pm0.1$ |

Table 3.3: The fitting results of the phase offset $\varphi_0$ (in the unit of rad) of the asymmetry parameter of $CH_3^+$ and $H_2^+$ fragments for the indicated energy ranges and intensities.

| Intensity($10^{14}$W cm$^{-2}$) | | $(0.8\pm0.1)$ | $(1.1\pm0.1)$ | $(1.5\pm0.1)$ |
|---|---|---|---|---|
| $H_2^+$ | (2-3) eV | $3.1\pm0.1$ | $3.0\pm0.1$ | $2.3\pm0.2$ |
| | (4-6) eV | $2.6\pm0.1$ | $2.4\pm0.1$ | $1.8\pm0.1$ |
| | (7-8) eV | $2.7\pm0.2$ | $1.8\pm0.1$ | $1.5\pm0.2$ |
| $CH_3^+$ | (1.5-2.5) eV | $3.7\pm0.1$ | $3.7\pm0.2$ | $2.7\pm0.3$ |
| | (4.5-6) eV | $2.8\pm0.1$ | $2.4\pm0.1$ | $2.6\pm0.2$ |

We believe the mechanism introduced at the beginning of this section is responsible for the observed control of directional emission of the fragmentation and the migration reaction of toluene. However, due to the complexity of toluene, simulations are out of the scope at the moment. This can be verified in the future with the development of theoretical capabilities.
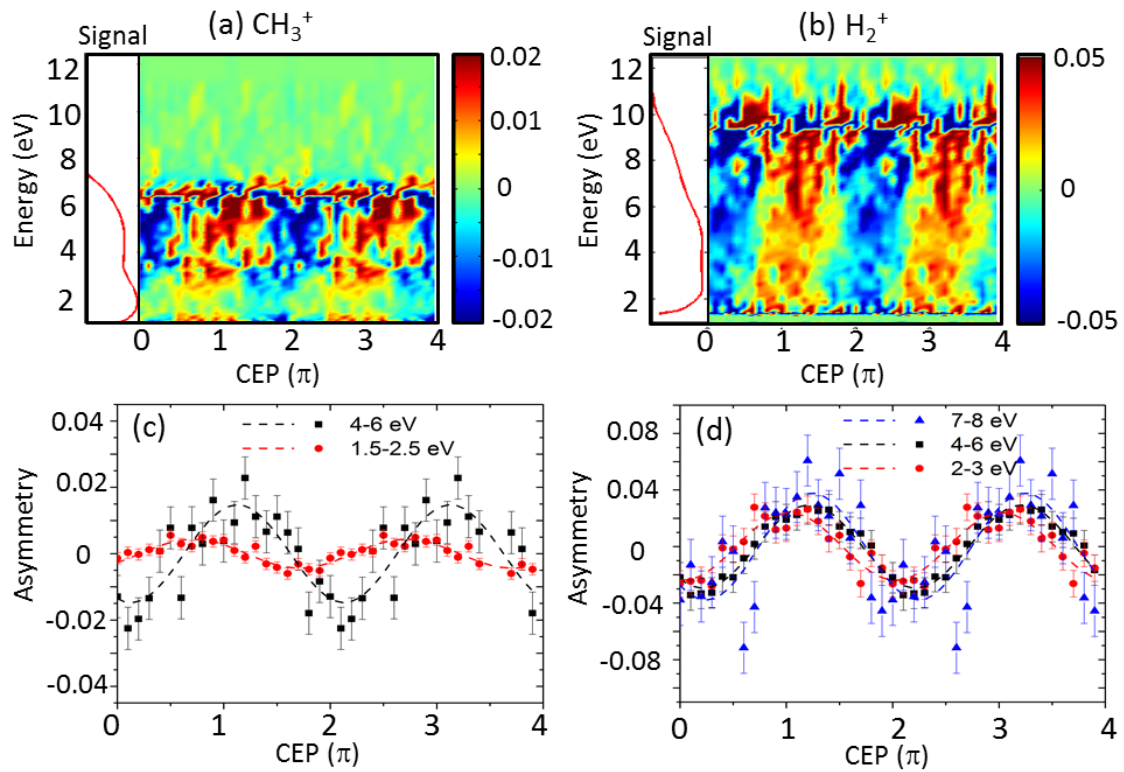
Figure 3.23: The asymmetries for (a) $CH_3^+$ and (b) $H_2^+$ fragment emission as a function of kinetic energy and CEP at the intensity of $(1.1\pm0.1)\times10^{14}$ W cm$^{-2}$. The kinetic energy integrated asymmetry for (c) $CH_3^+$ and (d) $H_2^+$ for the indicated energy ranges. (Adapted from Ref. [84])
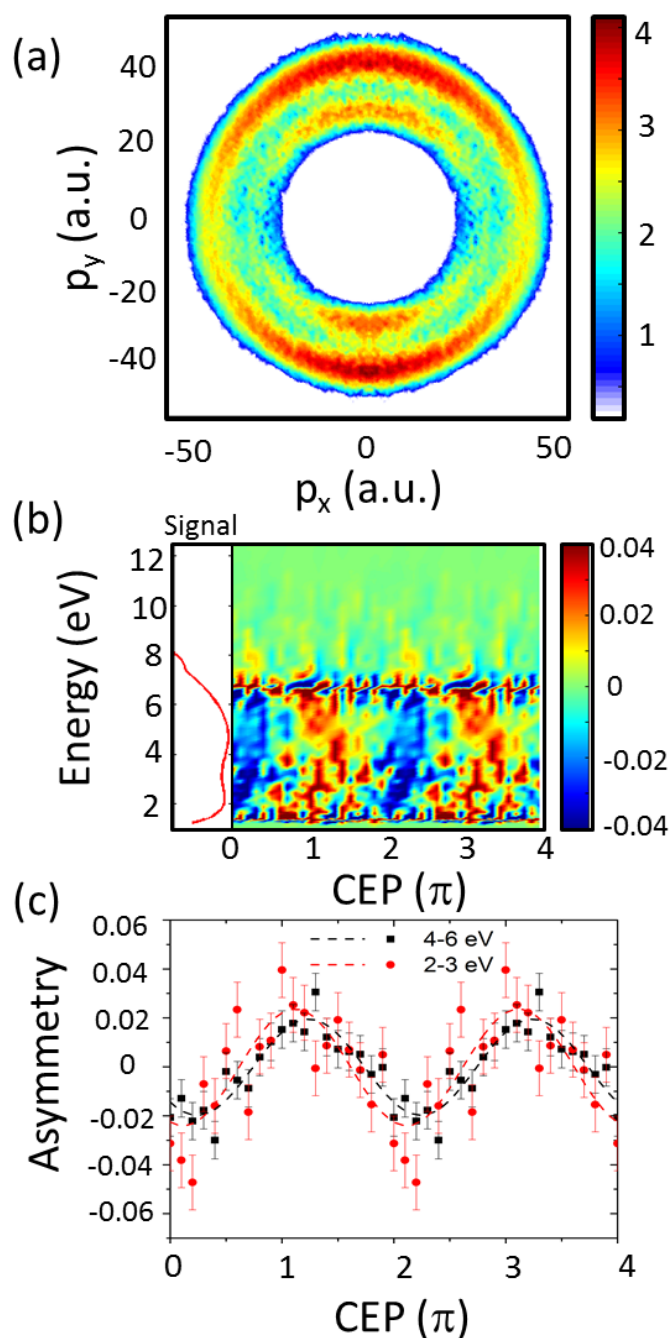
Figure 3.24: (a) CEP-averaged momentum distribution of $H_3^+$ from toluene with linear polarized few-cycle pulses at an intensity of $(1.1\pm0.1)\times10^{14}$ W cm$^{-2}$. (b) Kinetic energy spectrum and asymmetry map for $H_3^+$. (c) Kinetic energy integrated asymmetry parameters as a function of CEP for the indicated energy regions. (Adapted from Ref. [84])

## 3.5   Conclusions and outlook

In this chapter, we have dissussed the CEP-controlled ultrafast molecular dynamics in several molecular systems, i.e. from the prototype $D_2$ to more complex molecules. The main control knob utilized for the dissociative ionization of $D_2$ and DCl are the CEP and intensity of few-cycle pulses. For $D_2$, by exploring the reaction for an intensity range up to about $3.5 \times 10^{14}$ W cm$^{-2}$, we find the dissociation from higher excited states ($3\sigma$) of $D_2^+$ which can generate ions with kinetic energies above 8 eV. The observed asymmetry for the ion emission reveals two mechanisms for the population of the $3\sigma$ states. For low intensities, the molecule can be excited by electron recollision to the lower excited states, and being excited to the $3\sigma$ states subsequently by the laser-field. For higher intensities, the molecule can be directly excited to the $3\sigma$ states by electron recollision. For DCl, $D^+$ ion emission with kinetic energies above 15 eV are obtained for higher laser intensities above $2 \times 10^{14}$ W cm$^{-2}$. The quantum dynamical simulations indicate that the high kinetic energy signal can be attributed to double ionization induced by rescattered electrons, which exhibits a characteristic CEP-dependence. Then for even more complex molecular systems of hydrocarbons, we demonstrate the sub-cycle control of the hydrogen migration process utilizing few-cycle pulses. The underlying mechanism, which is revealed by a quantum dynamical model, is the manipulation of the phases of vibrational wavepackets when they superimpose. This mechanism, which has been successfully applied to the manipulation of the deprotonation process in hydrocarbons, can be generalized to isomerization processes.

There is still large room for further improvement. The hydrogen molecule and its isotopes performed as model systems in strong-field molecular physics and the related studies have improved our understanding of the interaction of strong fields with molecular targets. The previous experimental studies on electron localization in hydrogen addressed the control mechanisms, the reaction pathways and the optical parameter dependence of the control. However, new processes and mechanisms could be discovered by utilizing broader experimental conditions. Obviously, intensity serves as an experimental control parameter which can be easily adjusted. However, the combined effects of the exponential increasing of the ionization rate and saturation significantly limit the availability of the intensity range to be explored. In our work, using few-cycle pulses we can explore broader intensity region, where more highly excited states of $D_2^+$ can be populated. This could be prohibited for multi-cycle pulses due to the onset of double ionization processes. On the other hand, changing the wavelength is more effective with less limitation of saturation since the tunneling rate is independent of $\lambda$. Thus with the same intensity, the deep tunneling regime can be reached using longer wavelengths. Another strong motivation is to generate brighter and shorter attosecond bursts [118]. Longer driving wavelength at a certain intensity can produce a denser frequency comb ($\propto \lambda$) with a higher cutoff energy ($\propto \lambda^2$) [119]. Besides, the attochirp scales with $\lambda^{-1}$, indicating shorter attosecond bursts with longer wavelengths. The wavelength-dependent investigations can significantly benefit from the development of intense, ultrashort laser sources in the mid-infrared region. From the theoretical perspective, the strong-field interaction with hydrogen molecular ion can be

treated exactly with quantum mechanical computations. However, from neutral hydrogen molecules on, the exact modeling has become difficult. The theoretical development is very desirable for more complex molecular systems, which can benefit from comparing to a variety of experimental observations. On the other hand, the control mechanism for the hydrogen migration in hydrocarbons needs more verifications on other complex molecules both experimentally and theoretically. The simulation meets great difficulties for non-linear molecules. Nevertheless, we expect a dramatic development of theoretical ability in the near future which will help understanding the mysteries in complex molecular systems.

# Chapter 4

# Control of Coherent electron emission from $C_{60}$ by tailored few-cycle pulses

Electron dynamics are usually probed indirectly by detecting the molecular fragmentation signals of dissociative ionization channels. Based on the electronic and nuclear coupling, the information of electronic dynamics can be indicated. In general, the analysis for the fragmentation patterns is already complex for simple diatomic molecules, and quickly becomes extremely complicated for larger molecular systems due to huge amount of fragmentation channels [120]. It was proposed recently that by measuring the angularly resolved photoelectron distributions it is possible to probe the electronic dynamics before the onset of significant nuclear motion [121]. The intrinsic time scale for electronic dynamics is on the order of sub-femtoseconds. This time resolution can be reached by CEP-controlled near single-cycle NIR pulses.

The interaction of large molecules with ultra-fast laser pulses and the induced electron dynamics have been of fundamental importance to understand the properties of coherent control [122]. Here we select $C_{60}$ as a candidate for the investigation of collective electron motion. The $C_{60}$ fullerene is a unique prototype system with nanometer dimension and high degree of symmetry. It bridges the gap between atoms and condensed matter which not only exhibits hybrid properties of the two extremes, but also carries special characteristics. Many interesting physical properties have been discussed for $C_{60}$, such as high polarizability [123], macroatom behavior [124], large photoionization cross sections [125, 126], and *etc..* With single photon ionization, a wide range of Rydberg states have been recognized in $C_{60}$ [127]. Recently, super atomic molecular orbitals (SAMOs) have been discovered in solid state fullerene deposited on copper substrates and have also been reported in gas phase neutral $C_{60}$ molecules interacting with intense femtosecond laser pulses [128, 129]. SAMOs are diffuse hydrogen-like orbitals differing from the Rydberg states by significant electronic density existing inside the carbon cage [125]. With the development of varies laser systems, the ionization and fragmentation properties of $C_{60}$ have been widely studied as a function

of different laser parameters, such as pulse duration, wavelength, laser intensity [130] and so on. One interesting aspect is the different ionization behaviors in fullerene with different pulse durations. When using picosecond to nanosecond pulses, delayed ionization with a microsecond time scale was observed [131]. For intense short pulses (on the order of 100 fs), spectral peaks superimposing on a background signal from thermal electrons can be found [129, 132]. The nature of 'thermal electrons', can be understood as from rapid redistribution of the absorbed energy among the electronic degrees of freedom [133]. For short pulses with durations below 50 fs, multiphoton ionization was proven to be dominant [134]. In this work, CEP- and polarization-controlled 4 fs near single-cycle NIR pulses are used, where the interaction properties of fullerene have not been explored. Under this condition, the thermal electron emission can be dramatically suppressed. The angular-resolved electron distributions after laser-fullerene interaction are detected using a single-shot VMI spectrometer. It is shown that the coherent electronic wave packet motion can be controlled by the waveform and polarization of few-cycle laser fields.

## 4.1 Theoretical Models

The CEP-dependent electron emission from $C_{60}$ are investigated theoretically by both quantum dynamical and classical Monte-Carlo-trajectory simulations.

### 4.1.1 Quantum Dynamical Simulations

Quantum dynamical simulations on $C_{60}$ interacting with few-cycle laser pulses were carried out in Prof. Remacle's group at University of Liège in Belgium. The ionization and electronic dynamics in $C_{60}$ by a near single-cycle laser pulse are computed by solving the TDSE using a coupled equation scheme that includes the coupling between the bound states and the ionization continua [55]. The TDSE is expressed as

$$i\frac{\partial}{\partial t} \mid \Psi(t)\rangle = H(t) \mid \Psi(t)\rangle. \tag{4.1}$$

The Hamiltonian is expressed as below which is composed of the field free part $H^0$ and the time dependent electric field $\mathbf{E(t)}$

$$H(t) = H^0 + \mathbf{E(t)}. \tag{4.2}$$

In the simulation, $C_{60}$ molecules are treated with a fixed orientation along the laser polarization direction. The time-dependent electronic Hamiltonian includes the coupling with the laser electric field which is described in the dipole approximation by

$$\mathbf{E(t)} = \mathbf{k}E_0 e^{-(t-t_0)^2/\sigma^2}[\cos(\omega t + \varphi) - \frac{2(t-t_0)\sin(\omega t + \varphi)}{\omega\sigma^2}], \tag{4.3}$$

where $E_0$ is amplitude of the electric field, $\mathbf{k}$ is the polarization vector, $\omega$ is the angular frequency of the carrier wave, $\varphi$ is the CEP and $\sigma$ is the width of the Gaussian envelope. A

few-cycle pulse at a central wavelength of 720 nm with a 3.2 fs (FWHM) Gaussian envelope is used in the simulation.

The TDSE is solved numerically using a coupled equation scheme [121, 135] based on the partitioning technique [136, 137] in which the total space is partitioned into a bound subspace $\mathbf{Q}$ and an ionized subspace $\mathbf{P}$. The bound subspace is spanned on a basis of 407 electronic states of $C_{60}$ that includes the ground state and the 406 lowest excited states, which is shown below

$$\mathbf{Q} = \sum_{i-1} \mid \Psi_i^{Neut} \rangle \langle \Psi_i^{Neut} \mid . \tag{4.4}$$

The electronic structure of the 500 lowest excited states of $C_{60}$ are computed in the time-dependent density functional theory (TD-DFT) with the long range correlated CAM-B3LYP [138] functional and a 6-31$^+$G(d) basis set augmented by 6s, p and d additional diffuse functions centered in the $C_{60}$ cage [60]. Very diffuse basis functions are added in order to describe the highly excited Rydberg and SAMO states below the ionization potential (IP). Some examples of the molecular orbitals (MOs) of $C_{60}$ are shown in Fig. 4.1. Among the 500 excited states, 406 are below the IP and all of them have excitation energies lower than the Koopman's IP so that they are not spurious. Since autoionization is not included in the formalism, we only use the excited states below the IP in the basis of the bound states.
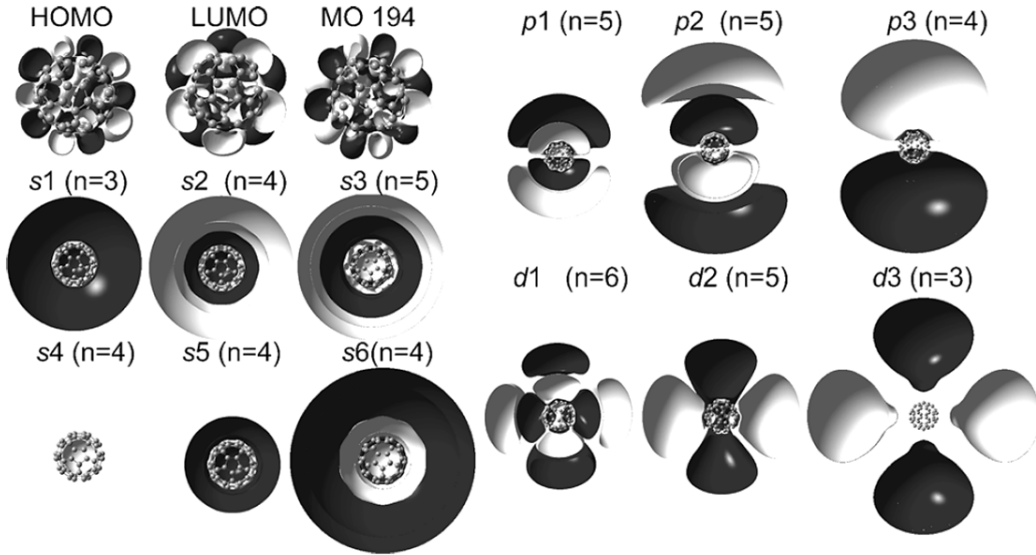


Figure 4.1: Examples of the computed isocontour amplitudes of the molecular orbitals (MOs) of $C_{60}$. (Taken from Ref. [125])

The ionized subspace is spanned on a basis of ionized states built from the antisymmetrized product of the field-free state of the cation $\Psi_j^{cat}$ and the wavefunction of the

ionized electron $\chi_k$ which is an orthogonalized plane wave with a wave vector $\mathbf{k}$ [139, 140].

$$\mathbf{P} = \sum_j \int d\mathbf{k} \mid \chi_k \Psi_j^{Cat} \rangle \langle \Psi_j^{Cat} \chi_k \mid, \tag{4.5}$$

The subspace $\mathbf{P}$ is composed of the ground state of the cation that is five times degenerate. For each cationic state, an ionization continuum discretized in energy and angle is associated. The momentum of the ionized electron varies between 0 and 2 a.u. with a step size of 0.01 a.u. and a set of 80 solid angle values is associated to each momentum value. The ionized subspace is spanned on a basis of 80000 states.

Most of the highly excited states accessed during the pulse have large photoionization widths to the ground state of the cation and negligible ones (200 times smaller) to the cationic excited states. Therefore, while it is important to have a large number of bound states to describe accurately the multiphoton excitation, it is enough to only include the five time degenerate ground state of the cation in the ionized subspace. The large difference in the values of the photoionization widths to the ground state of the cation and higher excited states can be understood from the analysis of their electronic configurations. The photoionization widths are computed as the integral of the dipole moment between an orthogonalized plane wave and a Dyson orbital that represents the overlap between an $n$ electron neutral state and an $(n-1)$ electron cationic state. The ground state of the cation has an electronic structure similar to that of the ground state of the neutral with an electron removed from the HOMO. It follows that only the excited states with an electronic configuration involving the excitation of an electron from the HOMO to a virtual orbital will have a non-zero Dyson orbital and a large photoionization width to the ground state of the cation. On the other hand, the photoionization widths to the excited cationic states are almost zero. In these cationic states an electron is excited from the HOMO-X to the HOMO, which implies that the Dyson orbital between the highly excited states of the neutral, presenting excitation of the HOMO to a Rydberg-type MO, and the cationic excited states will have a norm close to zero and thus a very small photoionization width. Only neutral bound states with an excitation from HOMO-X to a virtual orbital can photoionize significantly to these cationic excited states but none of these neutral excited states are significantly populated during the pulse.

Using the partitioning of the space into the bound ($\mathbf{Q}$) and ionized ($\mathbf{P}$) subspaces, the TDSE has the following form

$$i \begin{pmatrix} \mathbf{Q} \\ \mathbf{P} \end{pmatrix} \frac{d\Psi(t)}{dt} = \begin{pmatrix} \mathbf{Q}H\mathbf{Q} & \mathbf{Q}H\mathbf{P} \\ \mathbf{P}H\mathbf{Q} & \mathbf{P}H\mathbf{P} \end{pmatrix} \begin{pmatrix} \mathbf{Q}\Psi(t) \\ \mathbf{P}\Psi(t) \end{pmatrix}. \tag{4.6}$$

The $\mathbf{Q}H\mathbf{Q}$ and $\mathbf{P}H\mathbf{P}$ terms induce dipolar transitions between the electronic states of the neutral and the cation. The $\mathbf{P}H\mathbf{Q}$ and $\mathbf{Q}H\mathbf{P}$ terms describe the photoionization. The $\mathbf{Q}H\mathbf{Q}$ term describes the multiphoton excitation of the ground state and the motion of the electronic density induced by the pulse. The $\mathbf{P}H\mathbf{P}$ term describes the dynamics in the cationic states and the effect of the field on the ionized electron. Acceleration and

deceleration of the ionized electron by the vector potential are accounted for by using orthogonalized plane waves.

At each time step, the time-dependent wavefunction is composed of a coherent superposition of bound and ionized states with amplitudes which are obtained by numerically integrating the TDSE (Eqn. 4.6) using a $6^{th}$ order Runge-Kutta algorithm:

$$\mid \Psi(t)\rangle = \sum_i c_i^{neut} \mid \Psi_i^{neut}\rangle + \sum_j \sum_k c_{j,k}^{cat}(t) \mid \chi_k \Psi_j^{cat}\rangle \tag{4.7}$$

The photoelectron spectra are computed by integrating the population of the ionized states $|c_{j,k}(t)|^2$ at the end of the pulse. To obtain the CEP-dependent information, 24 simulations were performed for the linear and circular polarizations in which the CEP was varied systematically from 0 to $2\pi$. Focus volume averaging is also taken into account.

## 4.1.2 Monte Carlo Classical Trajectory Simulations

Since the electron trajectories are not easily accessible for the quantum calculations, semi-classical simulations of electron emission and rescattering were also performed for better understanding of the dynamics involved in the laser-fullerene interactions. This simulation work was carried out by people from Prof. Burgdörfer's group at Vienna University of Technology.

The process was simulated by a classical trajectory Monte Carlo method [141]. The aim was to identify the main physics which gives rise to the observed asymmetry by a minimal model containing only the essential physical points. In this simulation, electrons are emitted from the $C_{60}$ shell with a probability given by the ADK rate [142] at the classical tunneling exit with an initial velocity given by the ADK momentum [142]. The electrons are propagated according to Newton's equations of motion in the laser field (at 720 nm central wavelength and with 4 fs pulse length). Those electrons which return to the $C_{60}$ shell are scattered by the ionic cores, for which the double differential scattering cross sections from partial-wave analysis [143] were employed. The total elastic scattering cross sections from partial-wave analysis for electron impact onto a neutral carbon atom with energy up to 20 eV are of the magnitude $\geq$30 bohr$^2$, much larger than the surface area per carbon atom in $C_{60}$ (around 10 bohr$^2$). Thus it is assumed that every electron is scattered when it reaches the $C_{60}$ shell. The atomic scattering centers are randomly placed on the shell, therefore the spatial correlations between them can be neglected. Since the probability for small-angle scattering is large, electrons either penetrate the shell or undergo glancing collisions at the surface of the shell.

For linear polarization, the laser field can be denoted as $F(t) = F_0 f(t) \cos(\omega t + \varphi)$. Here, $\varphi$ is the CEP employing a sine-squared envelope $f(t)$ of a full length of 11 fs (corresponding to 4 fs FWHM) and a photon energy of $\omega = 1.7$ eV (central wavelength at 720 nm). The asymmetry at large electron energies is determined by the rescattering mechanism. Near the peak of the optical electric force, an electron tunnels out from the $C_{60}$ shell. As the field changes its sign, the electron is driven back towards its origin and some electrons undergo

elastic scattering reversing their velocity vector, allowing the electrons to gain large final energies. The distribution of the emitted electrons is calculated from the ensemble average over many trajectories with a half acceptance angle of 15 degrees, which is the same as what has been used in the analysis of the experimental data.

For circular polarization, the vector potential can be expressed as

$$\hat{A}(t) = f(t)(-\frac{F_0}{\sqrt{2}\omega})(\hat{e}_y \cos(\omega t + \varphi - \pi/2) + \hat{e}_z \sin(\omega t + \varphi - \pi/2)). \quad (4.8)$$

The time-dependent electric force of the laser in the polarization plane can be given as the time derivative of the vector potential $\hat{F}(t) = -\frac{d\hat{A}(t)}{dt}$ therefore has the following form

$$\hat{F}(t) = f(t)(\frac{F_0}{\sqrt{2}})(\hat{e}_y \cos(\omega t + \varphi) + \hat{e}_z \sin(\omega t + \varphi)). \quad (4.9)$$

In the absence of other forces, the final velocity $\hat{v}_f$ of an electron started at time $t_0$ with the initial velocity $v_0$ is given by

$$\hat{v}_f = \hat{v}_0 + \hat{A}(t_0). \quad (4.10)$$

Here, $A(t_0)$ is the vector potential at the birth time $t_0$.
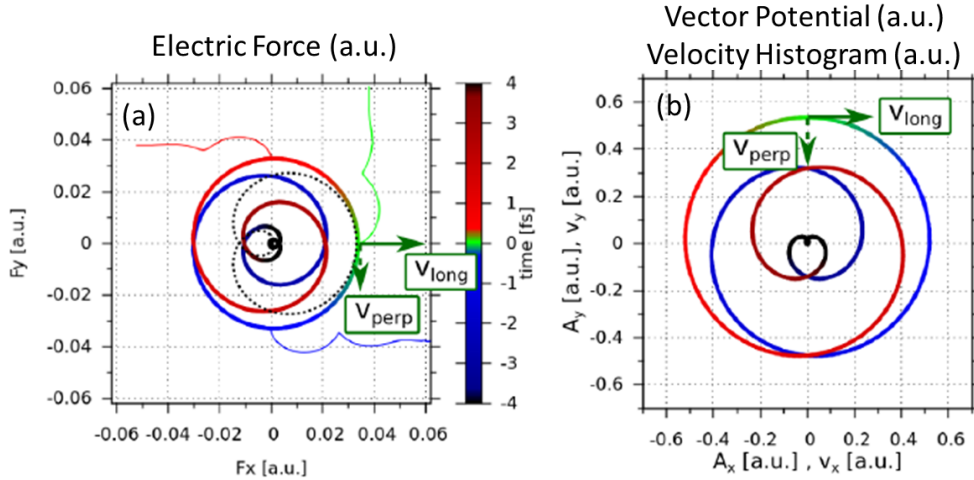


Figure 4.2: (a) Electron trajectories near the field maximum in a circularly polarized few-cycle laser field. (b) Illustration of the velocity vector and vector potential. (Courtesy of Dr. Georg Wachter)

For example, as shown in Fig. 4.2, electrons with zero initial velocity at the field maximum will end up at a final velocity pointing 90° with respect to polarization direction, following a corkscrew-like trajectory that spins away from the origin (the green trajectory

in Fig. 4.2 (a)). The same happens for other emission times (such as the red and blue trajectories in Fig. 4.2 (a)). This mechanism has been extensively investigated by U. Keller's group [144, 145]. For the cases that the initial velocity is nonzero, the initial velocity can be decomposed into the velocity along the radial coordinate $\hat{v}_{perp}$ and the velocity component along the longitudinal direction $\hat{v}_{long}$, as shown in Fig. 4.2 (b). The strongly nonlinear dependence of the ionization rate on the field strength leads to appreciable contributions to the electron spectra from only about one optical cycle around the field maximum.
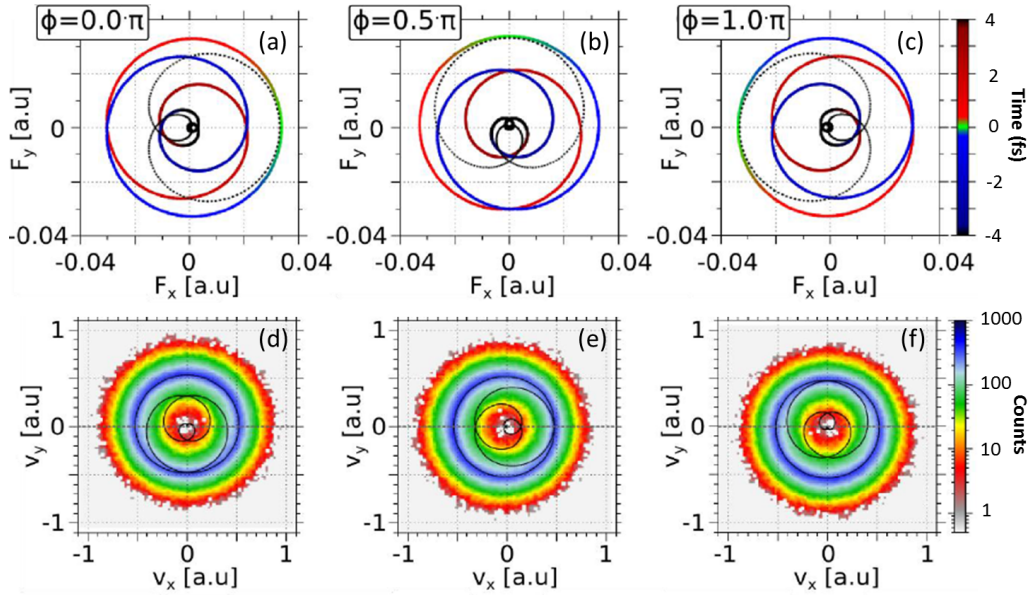


Figure 4.3: (a-c) Electric field for three different CEPs ($0$, $0.5\pi$ and $\pi$) for circular polarized 4 fs pulses. (d-f) The corresponding velocity histogram and vector potentials for the above CEPs. (Courtesy of Dr. Georg Wachter)

In contrast to linear polarization, rescattering is highly prohibited for the interaction of small atoms and molecules with circularly polarized laser field. For zero initial velocity at any emission time during the optical cycle, rescattering is not possible since the trajectories spiral away from their origin. Furthermore, it is not possible to reach velocities larger than the vector potential when starting with zero velocity. However, there is theoretical prediction that by combining co-rotating or anti-rotating circularly polarized pulse pairs, it is possible to get electrons recollide with the atomic core [146]. This still needs to be clarified by future experimental works.

Changing the CEP has, for circular polarization, the effect of rotating the pulse in the polarization plane (YZ plane). Employing the same simulation as for linear polarization, the effect of varying the CEP on the final velocity distributions projected along the z-axis are illustrated in Fig. 4.3. For circular polarization, the rescattering energy can be very low ($\leq 2U_p \sim 6.4$ eV) and scattering is expected to be approximately isotropic. The momentum

distributions and the asymmetry plots of the emitted electrons are calculated from an ensemble average comprised of over 300 million trajectories using a full acceptance angle of 30 degrees. The MC simulations are single electron calculations and electron-electron interactions are not taken into account.

## 4.2 Collective electron emission from $C_{60}$ in tailored few-cycle laser fields
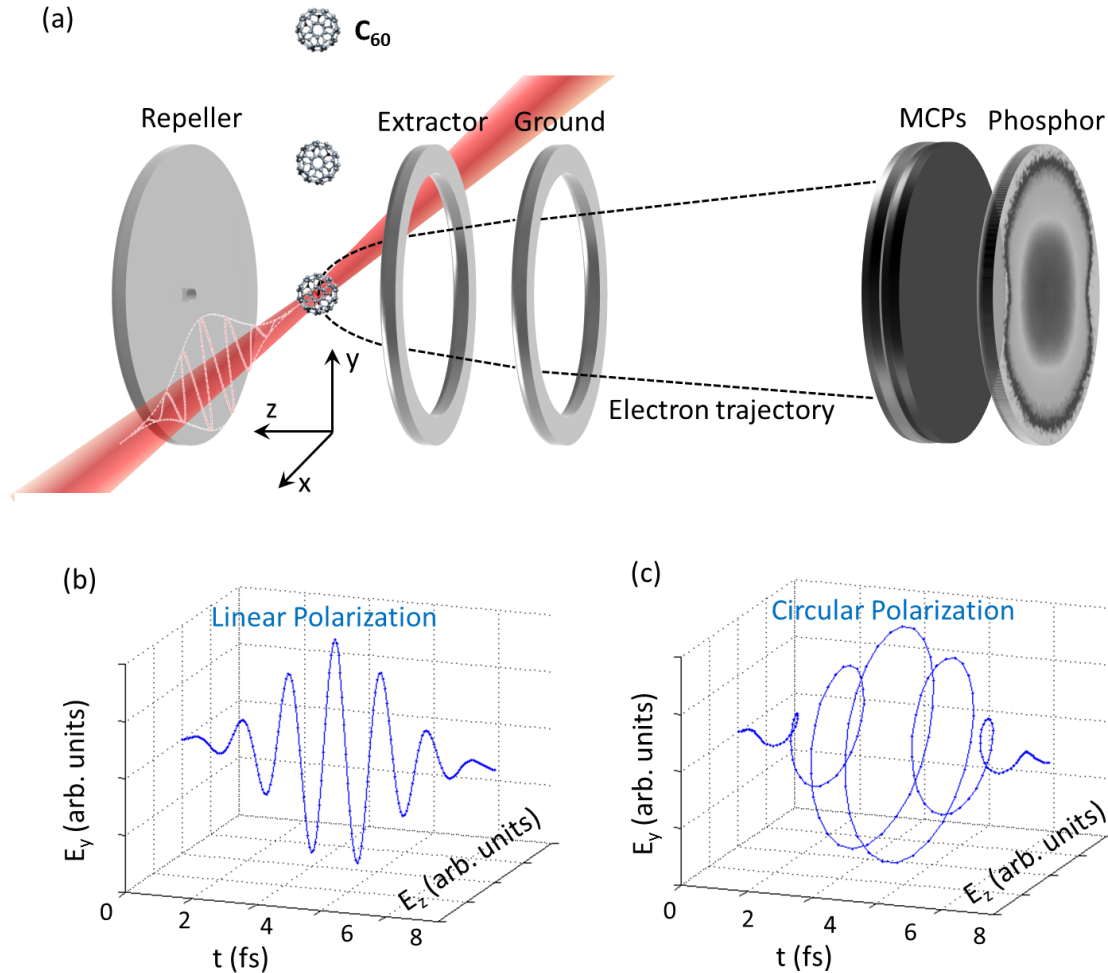


Figure 4.4: (a) Schematic drawing of the experimental geometry for laser interaction with $C_{60}$ and detection of electron emission with a VMI spectrometer. (b, c) Examples of the linearly and circularly polarized few-cycle NIR pulses used in the experiment (CEP=0), respectively. The pulses have a central wavelength at around 720 nm and a pulse duration of about 4 fs.

Experimentally, the electron emission from $C_{60}$ after interacting with near single-cycle NIR laser pulses for both linear and circular polarizations are recorded as a function of CEP utilizing phase-tagged single-shot VMI [55]. In other words, the laser pulses are tailored in both polarization and CEP for the steering of the collective electron motion in the multi-electron system, here $C_{60}$. A schematic drawing of the experimental configuration

is shown in Fig. 4.4. The 4 fs pulses at 720 nm central wavelength are generated from sending a beam of 25 fs pulses through a HCF and chirped mirror compressor. The HCF is filled with 2.8 bar of Ne gas for spectral broadening. After the compressor, the beam is split into two parts by a broadband beam splitter. A small portion (about 20 %) is sent to a stereo-ATI phase meter for CEP tagging. The main part is guided towards the single-shot VMI spectrometer. A combination of a broadband half-wave plate (HWP) and a broadband quarter-wave plate (QWP) is used for the adjustment between linear and circular polarizations. This beam is focused orthogonally to the C$_{60}$ molecular beam using a focusing mirror with 500 mm focal length. The dispersion for both the laser paths towards the phase meter and towards the VMI spectrometer are compensated seperately with a pair of fused silica wedges. There is a constant phase offset between the two paths, which can be calibrated from reference scans on the electron emission from Xe gas. The molecular beam of C$_{60}$ is generated from a home-made oven which was introduced in detail in Section 2.3.1. The convention is defined as follows, and is also shown in Fig. 4.4. The spectrometer detector lies in the x-y plane with the detector axis along the z-direction. The polarization axis of the linear polarized laser pulses is along the y-axis. The circular polarized pulses are polarized in the y-z plane.

**Linear polarization**
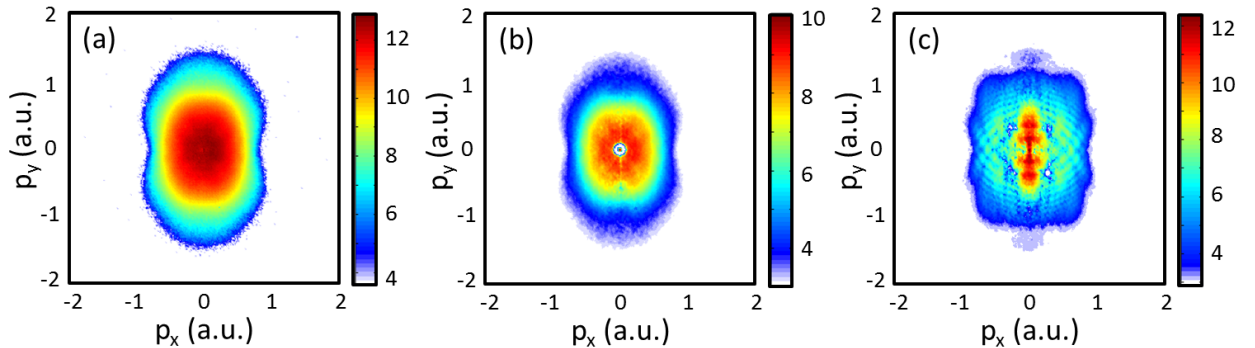


Figure 4.5: Raw (a) and Abel-inverted (b) CEP-averaged electron momentum image from C$_{60}$ with linear polarization at an intensity of $(6.5\pm0.5)\times10^{13}$ W cm$^{-2}$. The inverted VMI image from electron emission from Xe gas under identical experimental conditions.

The CEP-averaged VMI images obtained from linear polarized pulses at an intensity of $(6.5\pm0.5)\times10^{13}$ W cm$^{-2}$ are shown in Fig. 5.7. This intensity corresponds to a laser field amplitude of about 22.1 GV m$^{-1}$. Fig. 5.7 (a) is the raw VMI image from C$_{60}$ representing the electron momentum distribution projected along $p_z$, while Fig. 5.7 (b) is the Abel-inverted image representing the electron momentum distribution in a plane at $p_z = 0$. The inverted VMI image from Xe under identical experimental conditions is shown
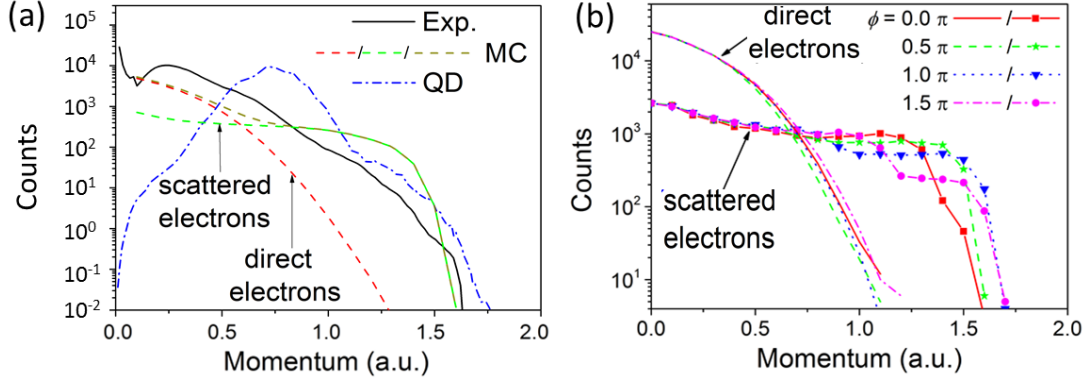
Figure 4.6: (a) Experimental and theoretical photoelectron spectra of $C_{60}$ with linear polarization at an intensity of $(6.5\pm0.5)\times10^{13}$ W cm$^{-2}$. The experimental data (the solid curve) is obtained from angular integration of Fig. 5.7 (b). The result from MC simulations is shown as dashed line, while that from the QD simulation is shown as dash-dotted line. (Taken from Ref. [55]) (b) Contributions from direct and rescattered electrons at four different CEPs (0, $0.5\pi$, $\pi$, and $1.5\pi$) obtained from MC simulations.

in Fig. 5.7 (c). Xe is a well-studied atomic system, therefore it serves as a reference in our study. We can see that the electron momentum distribution from $C_{60}$ does not exhibit the fine structures such as the ATI patterns appearing for Xe. A previous study has shown that $C_{60}$ behaves as a 'macro-atom' and the smoothing of the spectral structure is from the influence of electron-electron interactions [124]. The cutoff momentum for electrons from both $C_{60}$ and Xe are similar, which is around 1.5 a.u. for linear polarization. This corresponds to a cutoff energy at about 10 $U_p$, where $U_p$ is the ponderomotive energy and is given by $U_p = E^2/(4\omega^2)$ (in atomic units).

Fig. 4.6 shows the computed (from both MC and QD methods) and the experimental ionization yield as a function of the radial momentum $p_r$, where $p_r$ is defined as $p_r = \sqrt{p_x^2 + p_y^2}$. Nice agreement for the cutoff from both the experimental data and the simulated results can be seen, which are all around 1.5 a.u.. From the MC results, contributions from the direct and the rescattered electrons can be distinguished by tracing different electron trajectories. It is shown in Fig. 4.6 (a) that the rescattered electrons start to dominate the signal above 0.6 a.u.. Furthermore, the contribution for direct and rescattered electrons for several CEPs are shown in Fig. 4.6 (b). Clear CEP-dependence in the electron yield can be recognized for the cutoff region, which is dominated by the scattered electrons. On the other hand, there is deviation in the low-momentum region between the QD simulated electron spectra and the measured data. The main reason is the improper representation of the Coulomb interaction between the cationic core and the ionized electron. The ionization from the deeply bound states by tunneling or autoionization which are expected to generate low momentum electrons is not included properly in the formalism of the QD model. However, it should be noted that the asymmetry expected from these contributions is
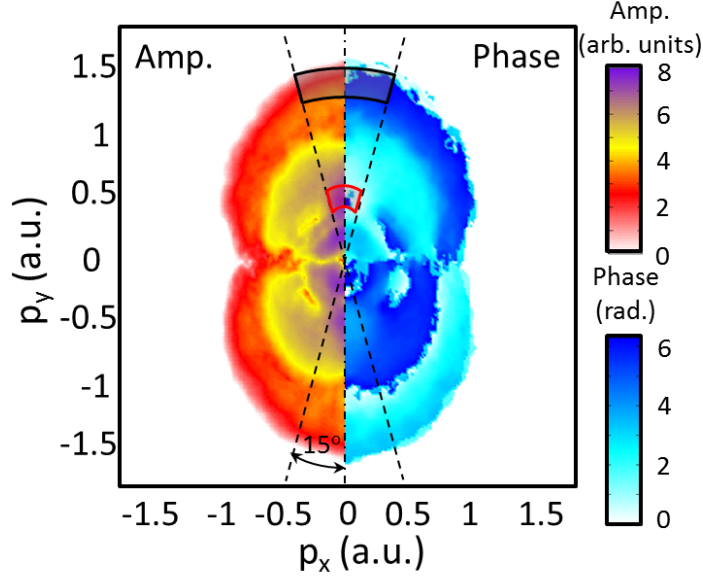
Figure 4.7: Momentum-dependent amplitude (the left part) and phase (the right part) of the CEP-dependent oscillation in the photoelectron yield from C$_{60}$ for linear polarization at an intensity of $(6.5\pm0.5)\times10^{13}$ W cm$^{-2}$. Only half of the image is shown due to $p_x$, -$p_x$ symmetry.

very small (which can be shown later), thus cannot significantly affect the main physical observation.

Utilizing a phase-tagged VMI approach, it also permits to investigate the amplitude and phase of the CEP-dependent part of the electron emission as a function of the momenta $p_x$ and $p_y$. For each postion in momentum space, the CEP-dependent electron yield can be fitted with the following function:

$$Y(p_x, p_y, \varphi) = Y_0(p_x, p_y) \cos(\varphi + \Delta\varphi(p_x, p_y)) \tag{4.11}$$

where $Y$ represents the electron yield, $Y_0$ is the amplitude of the oscillation and $\Delta\varphi$ denotes a phase offset. The experimental yield is integrated over $p_x$ and $p_y$ using a bin size around 0.02 a.u. $\times$ 0.02 a.u.. The momentum distributions of the parameters $Y_0$ and $\Delta\varphi$ are shown in Fig. 4.7. Due to the symmetry between -$p_x$ and $p_x$ only half of the image is shown. The left part of Fig. 4.7 shows the amplitude map while the right part is the phase map of the CEP-dependent part of electron yield. An angular region with nearly constant amplitude and phase of around 15° with respect to the laser polarization axis is marked by the dashed lines. A momentum region from 0.4-0.6 a.u. which is marked by the red line is chosen for the direct electrons. The region of rescattering electrons is selected close to the cutoff and marked by the black line.

Based on the above regions, the directional emission of electrons can be analyzed with
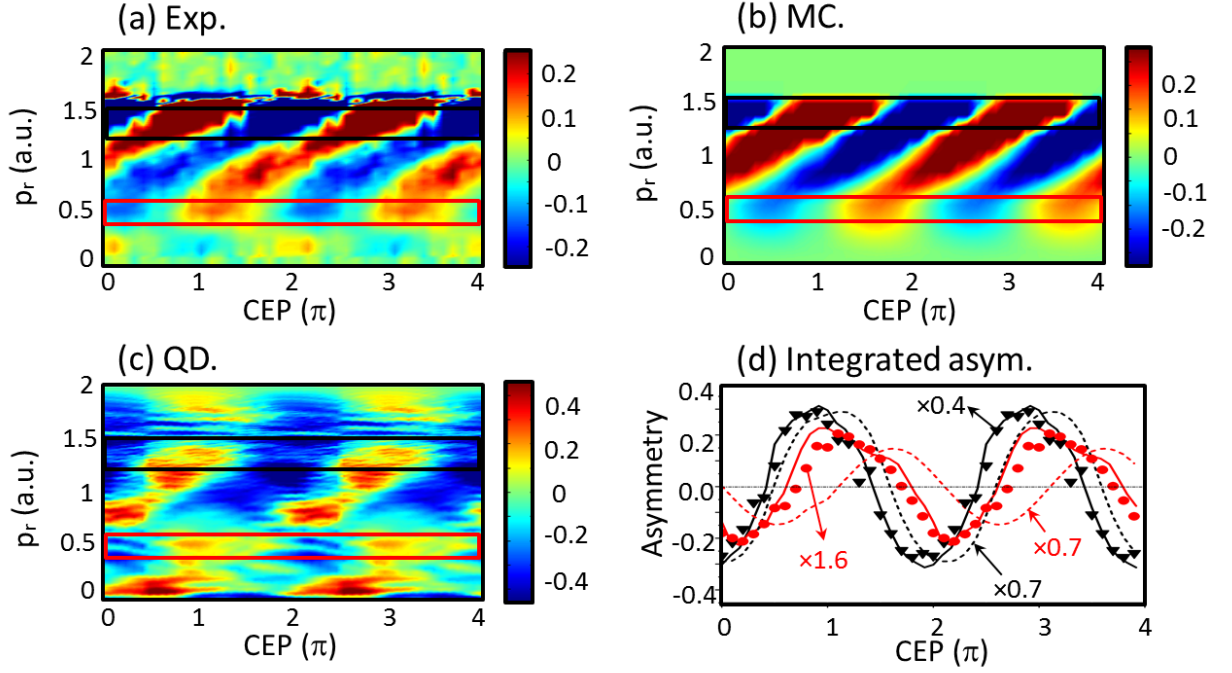
Figure 4.8: Density map of asymmetry parameter as a function of CEP and radial momentum obtained from experimental data (a), MC (b), and QD (c) simulation results for linear polarization, respectively. (b) Comparision between angle- and momentum-integrated asymmetries from experiment for electrons with high momentum close to the cutoff (scattered triangles) and for electrons with low momentum (scattered bullets), QD simulation results (solid curves), and MC simulations (dotted curves), respectively. The high-momentum electrons are obtained by integration over a momentum range between 1.3-1.5 a.u., and the low-momentum electrons are from 0.4-0.6 a.u.. Some of the data were scaled by the indicated factors for better comparison. (Adapted from Ref. [55])

the asymmetry parameter, which is defined as

$$A(\mathbf{p}, \varphi) = \frac{Y_{up}(\mathbf{p}, \varphi) - Y_{down}(\mathbf{p}, \varphi)}{Y_{up}(\mathbf{p}, \varphi) + Y_{down}(\mathbf{p}, \varphi)}, \tag{4.12}$$

where $\mathbf{p}$ is the momentum vector, $\varphi$ is the CEP, $Y_{up}(\mathbf{p}, \varphi)$ and $Y_{down}(\mathbf{p}, \varphi)$ represent the electron yields in the up (+y) and down (-y) directions, respectively. The asymmetry maps as a function of electron radial momentum $p_r$ and CEP from both experiment and theory are shown in Fig. 5.10 (a-c). The data are measured within 0-2$\pi$ and are copied to 2$\pi$-4$\pi$ for better visulization. A strong oscillation of the asymmetry parameter up to about 30 % is obtained which indicates a strong control over the electron emission from the near-single cycle pulses. Fig. 5.10 (d) shows the comparison of the momenta-integrated asymmetry oscillations obtained from the indicated regions shown in Fig. 4.7. There is characteristics difference on the asymmetry parameter between the direct and the rescattered electrons.

For the high-momentum region close to the cutoff (1.3-1.5 a.u.) the agreement from both the quantum and the classical simulations with respect to the experimental data are nice, which can be seen more clearly by the integrated asymmetry parameters (black data) in Fig. 5.10 (d). The amplitude of the oscillation exhibits an offset of about a factor of 2 between the theoretical prediction and measured results. Despite this, the agreement on both periodicity and phase are good for both MC and QD results.

For the low-momentum region, which is chosen to be the highest discernible momentum region for direct electrons (0.4-0.6 a.u.), the QD simulation results show a better agreement with the experimental data, while the MC simulations exhibit a large phase offset. From all above, the QD method shows nice agreement for both high and low momentum regions, which are dominated by rescattered and direct electron emission. The formalism of the quantum simulation takes into account the dynamics in the electron bound states induced by their coupling to the photoionizaiton continuua and the dynamical change in the ionization potential in the strong optical field. An outgoing electron can be driven by the external electic field and can be captured later by a bound state. This electron can be ionized again in a different direction. Based on this, the rescattering process is also introduced in the QD method. The angular distribution of the electron emission from an ionization process depends on the electronic dynamics and the coupling elements of the transitions from the ground and the excited states to the ionized states. The electronic dynamics, which can be predicted by the time-dependent electron density [121, 135], significantly depend on the property of the optical field, such as the CEP, the polarization, and the electric field strength. On the other hand, the coupling elements depend on the electric field strengh and the electronic structure of the molecular system. According to these, the CEP-dependent oscillation of the asymmetry parameter for the electrons from direct ionization can be controlled by the evolution of the electronic wave packet.

The motion of the electronic density induced by the NIR pulse generates a coherent superposition of the ground and the excited states. Different states can be accessed during the pulse depending on the CEP for a linearly polarized near single-cycle pulse. The time-dependent population of the electronic bound states of $C_{60}$ is shown in Fig. 4.9 (b), with the density of electronic states as a function of the excitation energy at several time points shown in Fig. 4.9 (a). Complex transient dynamics is induced during the laser pulse, as shown in Fig. 4.9 (c) and (d). The ground state can be efficiently excited at the beginning of the pulse by multiphoton ionization. The dipole moment follows the electric field almost adiabatically at the beginning of the pulse, until around 3.5 fs, when the electric field reaches its maximum and the ionization rate increases dramatically, the dipole moment suddenly collapses and follows a complex motion afterwards. As shown in Fig. 4.9 (e), for CEP=0, the electron density mainly localizes at the bottom (-y direction) of the molecule at the time of ionization. In principle, the variation of the time-dependent density can be reflected by the change of the asymmetry parameter in the direct ionization region [121]. When the density is mainly localized at the bottom of the molecule, the photoionization probability is higher in the -y direction. This will result in a higher yield in the -y direction for the direct electron emission, thus a negative asymmetry parameter. The situation is reversed for CEP=$\pi$. It is calculated that about 0.3 of the electron density

is transferred from the top to the bottom in the molecule. This demonstrates the control over spatial localization of the electron density at the peak of the laser pulse by changing the CEP. For other CEP values, for instance CEP=$\pi/2$ and $3\pi/2$, the dipole moment and the asymmetry parameter are of a smaller value due to the fact that more electron density is delocalized on the molecule. Table 4.1 shows the calculated dipole moments as well as the asymmetry parameters for several CEPs at the peak of the laser pulse obtained from QD simulations.

Table 4.1. The calculated dipole moments and asymmetry parameters (at the time $t = 3.5$ fs, when the pulse reaches its maximum) at several CEPs for a linear polarized few-cycle pulse. The asymmetry parameter is shown for the direct ionization region ($\mathbf{p} = 0.55$ a.u.), the intermediate ($\mathbf{p} = 0.85$ a.u.), and the rescattering region ($\mathbf{p} = 1.35$ a.u.), respectively. (Taken from Ref. [55].)

| CEP ($\varphi$) | $\mu_y(a.u.)$ | $A(\mathbf{p} = 0.55a.u.)$ | $A(\mathbf{p} = 0.85a.u.)$ | $A(\mathbf{p} = 1.35a.u.)$ |
|---|---|---|---|---|
| 0 | 2 | -0.12 | 0.23 | -0.28 |
| $\pi/2$ | 1 | -0.04 | 0.15 | -0.08 |
| $\pi$ | -2 | 0.13 | -0.20 | 0.25 |
| $3\pi/2$ | -1 | 0.01 | -0.16 | 0.04 |

For the rescattered electrons, the asymmetry parameter is calculated to be negative for CEP=0 and positive for CEP=$\pi$ as shown in Table 4.1. This agrees well with the experimental results shown in Fig. 5.10. In the intermediate momentum region where both direct and scattered electrons contribute, a change of the asymmetry parameter from positive to negative for a CEP of 0 and of $\pi$ is shown, which has also been observed in the experiment.
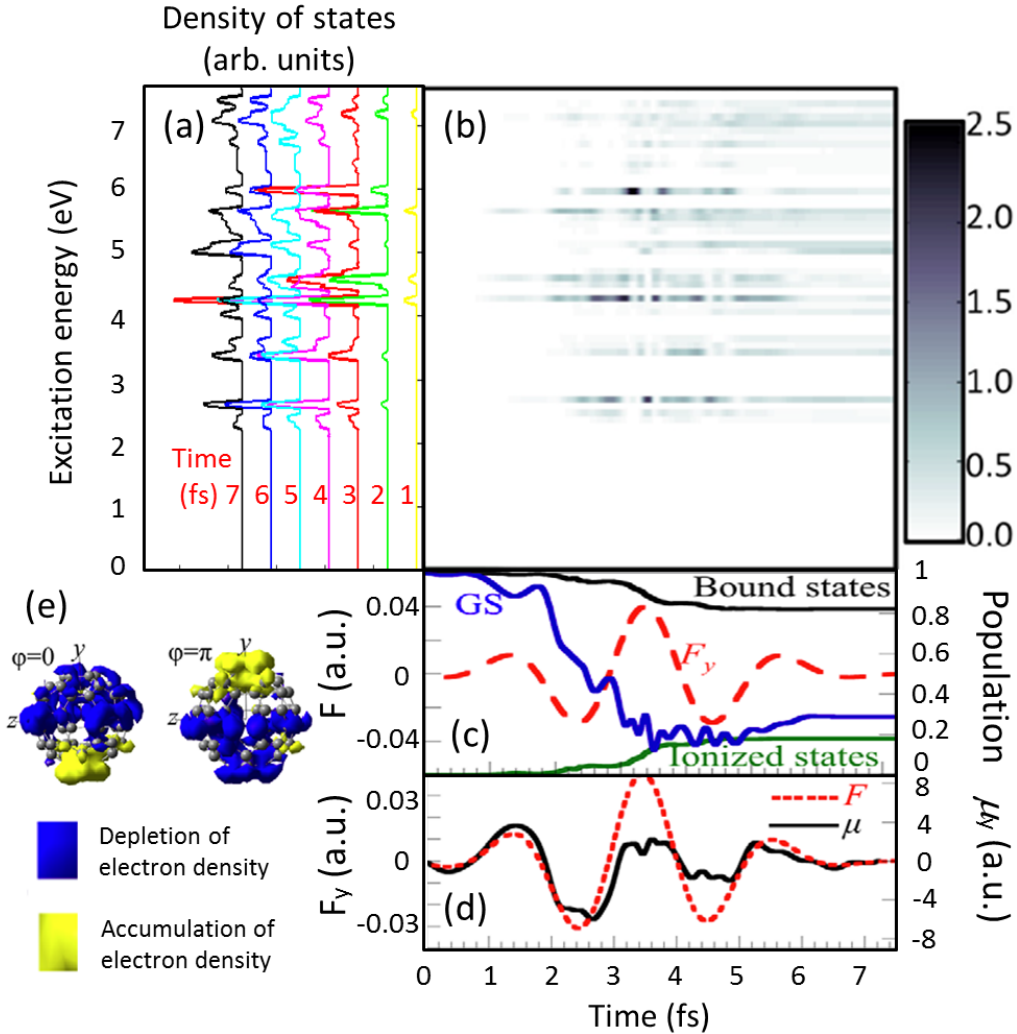
Figure 4.9: (a) Density of the electronic states of $C_{60}$ as a function of the excitation energy for several time points indicated by the red numbers. (b) Time-dependent population of the electronic bound states of $C_{60}$ for a linearly polarized laser pulse with CEP=0. (c) Time-dependent population of the ground state (GS), bound and ionized states for $C_{60}$ for linear polarization. (d) The dipole oscillations along the direction of the electric field for linear polarization. (e) The isocontour difference $(0.0003| e |/Å^3)$ between the density at the time $t$=3.5 fs and $t$=0 fs are shown for CEP=0 and $\pi$ for linear polarization, respectively. (Adapted from Ref. [55])

**Circular Polarization**
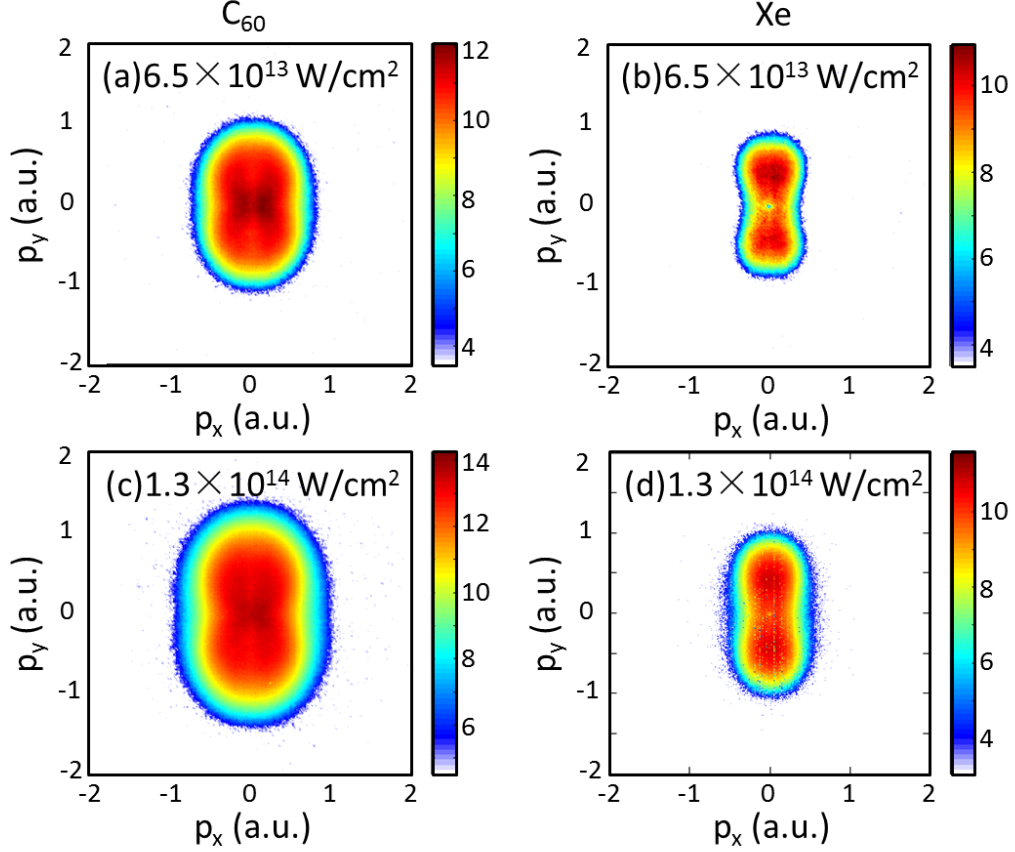


Figure 4.10: CEP-averaged electron momentum image from $C_{60}$ with circular polarization at an intensity of (a) $(6.5\pm0.5)\times10^{13}$ W cm$^{-2}$ and (c) $(1.3\pm0.1)\times10^{14}$ W cm$^{-2}$, respectively. (b, d) CEP-averaged electron momentum image from Xe gas under identical experimental conditions. The polarization plane for the circular polarized pulses is in the y-z plane. (Adapted from Ref. [55])

Besides the work carried out using linear polarized few-cycle pulses, similar measurements and simulations have also been performed for circular polarization. The experimental momentum distributions of electron emission from both $C_{60}$ and Xe using circular polarized near single-cycle NIR pulses are shown in Fig. 4.10 for two laser intensities, i.e. $(6.5\pm0.5)\times10^{13}$ W cm$^{-2}$ and $(1.3\pm0.1)\times10^{14}$ W cm$^{-2}$, respectively. These VMI images are the projection of the 3D momentum distribution onto the x-y plane, with the laser polarized in the y-z plane. Xe is a well-studied atomic system and it is known that the electron rescattering process can be prohibited in Xe with a cutoff energy at about $2\,U_p$ for circular polarization. The electrons are mainly from a direct ionization process. From the comparison of the experimental data between Xe and $C_{60}$ in Fig. 4.10, we can clearly see
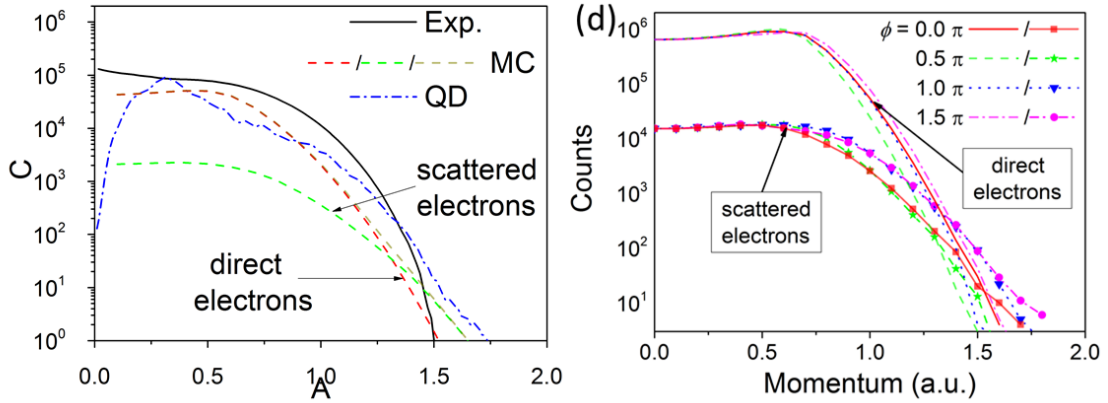
Figure 4.11: (a) Experimental and theoretical photoelectron spectra of $C_{60}$ with circular polarization at an intensity of $(1.3\pm0.1)\times10^{14}$ W cm$^{-2}$, respectively. The experimental data (the solid curve) is obtained from angular integration of Fig. 4.10 (c). The results from MC simulations are shown as dashed line, while that from the QD simulation is shown as dash-dotted line. (b) Contributions from direct and rescattered electrons at four different CEPs (0, $0.5\pi$, $\pi$, and $1.5\pi$) obtained from MC simulation. (Adapted from Ref. [55])

a broader angular distribution and a higher cutoff energy for the results of $C_{60}$. The corresponding electron spectra for the higher intensity are shown in Fig. 4.11 together with the theoretial simulation results. The MC results show a clear contribution from rescattered electrons, which starts to dominate the signal from about 1.3 a.u.. The momentum cutoff are all around 1.5 a.u. for both the simulated results and the measured data, which corresponding to a cutoff energy around 10 $U_p$. The CEP-dependence of the electron emission from direct and scattered electrons from MC simulation is also shown in Fig. 4.11 (b). This observation is unique comparing to other atomic and simple molecular systems.

The CEP-dependent yield and asymmetry oscillations are also analyzed for circular polarization. Similar to the results shown in the previous section, the amplitude and phase of the CEP-dependent electron yield are shown in Fig. 4.12. The same angular and momentum regions as those for the linear polarization are selected for the analysis of the asymmetry parameter. The resulting asymmetry maps as a function of electron radial momentum and CEP from experiment, MC, and QD simulations are shown in Fig. 4.13 (a-c), with the angle- and momentum-integrated asymmetry parameters shown in Fig. 4.13 (d). A good agreement is obtained for the high momentum electrons from both MC and QD simulation results. While the QD results show a better agreement to experimental results in the low-momentum region compared to that of the MC calculations. The MC simulation shows that the high-momentum electrons are dominated by a rescattering process, which is a new observation for complex systems for circular polarization.

Differing from the asymmetry map for linear polarization, we observed a pronounced leftward tilt of the asymmetry in the high momentum region for the circular polarization.
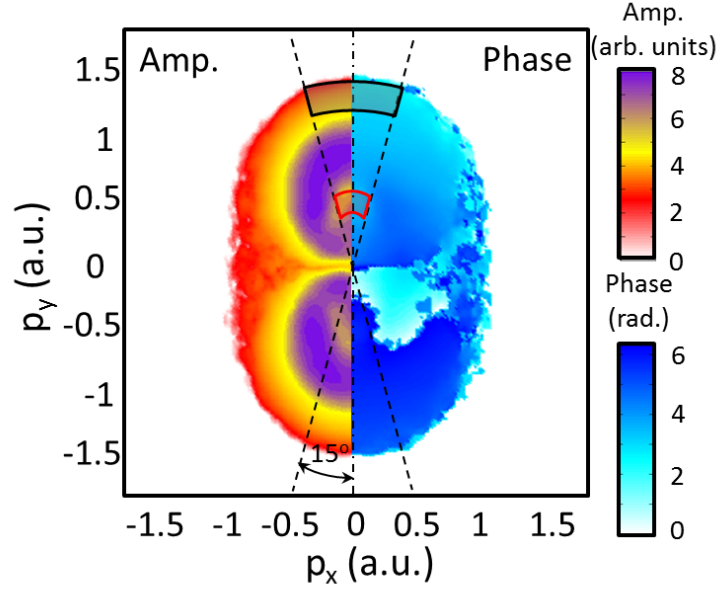
Figure 4.12: Momentum-dependent amplitude (the left part) and phase (the right part) of the CEP-dependent oscillation in the photoelectron yield from $C_{60}$ for circular polarization at an intensity of $(1.3\pm0.1)\times10^{14}$ W cm$^{-2}$. Only half of the image is shown due to $p_x$, -$p_x$ symmetry. (Adapted from Ref. [55])

The rightward tilt for linear polarization originates from the correlation of the recollision time and the recollision energy, which has been widely investigated in many atomic and molecular systems [8]. However, a left tilt indicates that the high momentum electrons are advanced to the electrons with lower momenta with respect to the rotation direction of the laser field. Both MC and QD results show a leftward tilt. The underlying mechanism can be illustrated from trajectory analysis. Fig. 4.14 shows an example of the rescattering trajectories obtained for $C_{60}$ in a circularly polarized near single-cycle laser field. Briefly, they arise from a series of small-angle collisions of the electron with the $C_{60}$ shell.

As shown in Fig. 4.14, to generate electrons which can gain high momenta in the circularly polarized laser field, the instantaneous momentum vector needs to stay aligned with the laser induced force $\mathbf{F}_N(t) \propto -\mathbf{E}_N(t)$ during the rescattering process. Fig. 4.14 shows the time dependent properties for the electron trajectories corresponding to the electron emission with the highest momenta observed in the experiment. The MC simulations show that about 1% of the trajectories lead to scattering. Most of these trajectories involve electrons experiencing two to three small-angle collisions at the shell. The velocity vector is rotated with the circularly polarized laser field during the process. At the end, the electrons will exhibit a momentum vector pointing in the direction which is opposite to that of their initial direction. This rotation of 180° differs from the general 90° rotation angle for circular polarization without the existance of a rescattering process. The advancement
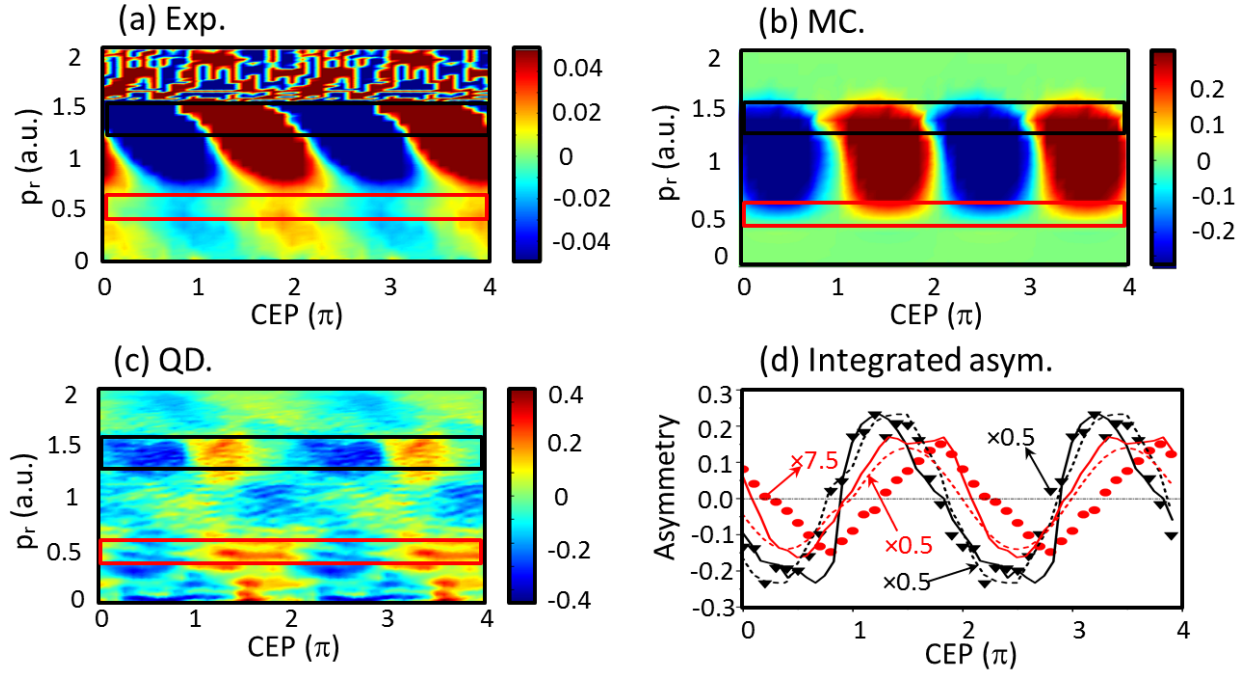
Figure 4.13: Density map of asymmetry parameter as a function of CEP and radial momentum obtained from (a) experimental data measured from $C_{60}$, (b) MC, and (c) QD simulation results for circular polarization, respectively. (b) Comparision between angle- and momentum-integrated asymmetries from experiment for electrons with high momentum close to the cutoff (scattered triangles) and for electrons with low momentum (scattered bullets), QD simulation results (solid curves), and MC simulations (dotted curves), respectively. The high-momentum electrons are obtained by integration over a momentum range between 1.3-1.5 a.u., and the low-momentum electrons are from 0.4-0.6 a.u.. Some of the data were scaled by the indicated factors for better comparison. (Adapted from Ref. [55])

results in a leftward tilt in the asymmetry map. This recollision mechanism for circular or elliptical polarization will likely play an important role in other complex molecular systems and nanosystems.

The QD simulations, which provide better agreement for the low momentum electron emission, indicate that the asymmetry oscillation for these electrons, dominated by the direct ionization process, reflects the instant electron localization at the time of ionization. The calculated dynamics are shown in Fig. 4.15. For circular polarization, the dipole moment undergoes a spiraling motion and only reduces to zero at the end of the laser pulse. The electron density localizes at the bottom of the molecule at the time of ionization ($t = 3.5$ fs) for CEP=0. Other cases for CEP=$\pi/2$ and $\pi$ are also shown in Fig. 4.15 (e). The results demonstrate that the localization of the bound electron density can by
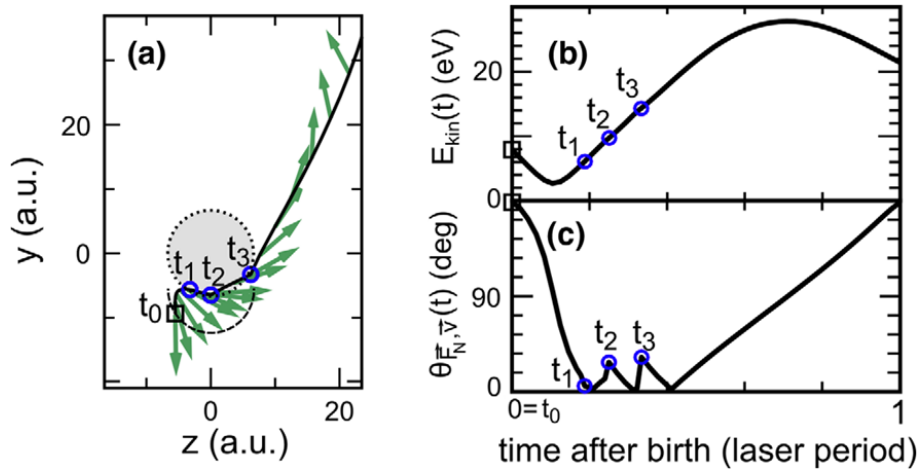
Figure 4.14: (a) The rescattering trajectory (black solid curve) for circular polarization obtained from MC simulations. The green vectors are time-dependent laser-induced forces. The blue circles represent the scattering events which occur at the C$_{60}$ shell (dotted circle) at times $t_1$, $t_2$ and $t_3$. (b) Time-dependent electron kinetic energy. (c) The angle $\theta_{F_{N,v}}(t)$ between the velocity $v(t)$ and the laser force as a function of time. (Taken from Ref. [55])

controlled by the CEP for a circularly polarized few-cycle pulse.
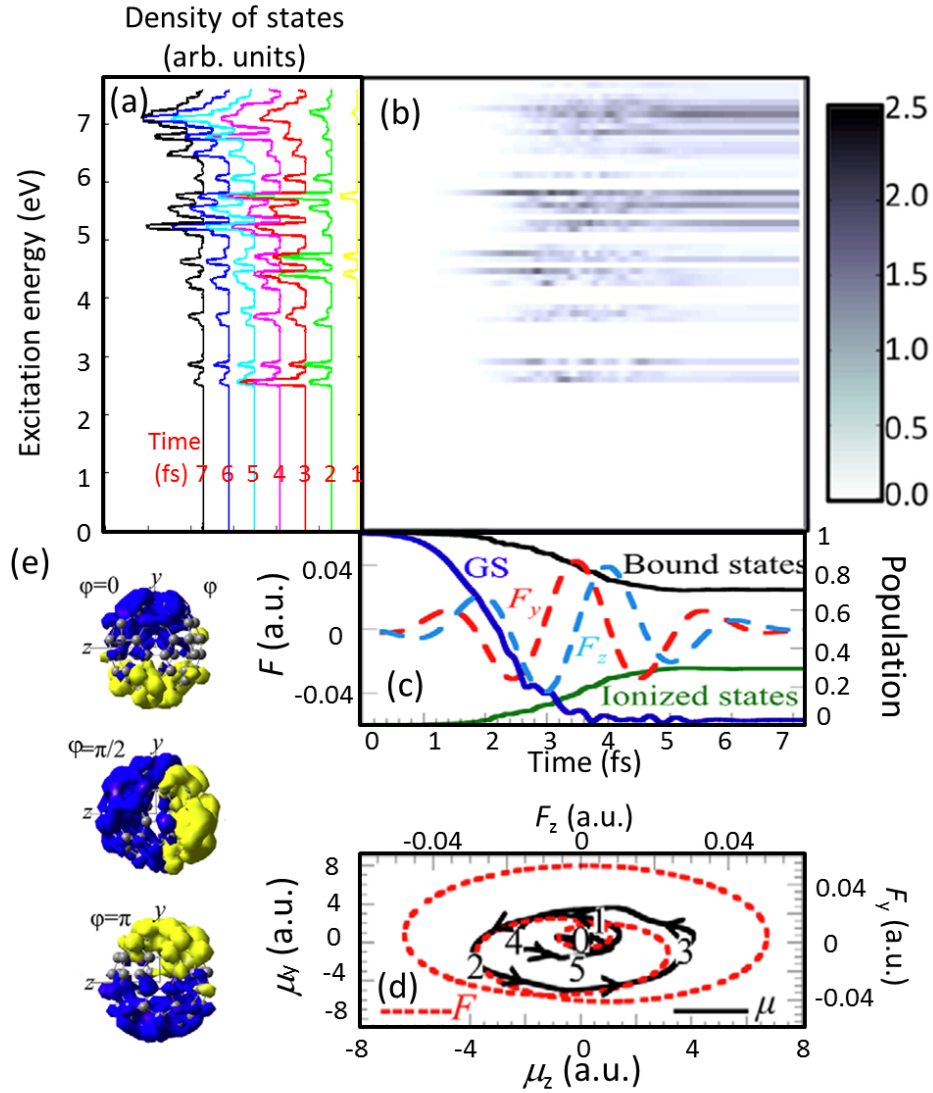
Figure 4.15: (a) Density of the electronic states of C$_{60}$ as a function of the excitation energy for several time points indicated by the red numbers for a circularly polarized laser pulse with CEP=0. (b) Time-dependent polulation of the electronic bound states of C$_{60}$. (c) Time-dependent population of the ground state (GS), bound and ionized states for C$_{60}$ for circular polarization. (d) The dipole oscillations in the polarization plane of the electric field for circular polarization. The dipole undergoes a spiraling motion as a function of time (shown by the numbers on the dipole curve). (e) The isocontour difference $(0.0003| e |/\text{Å}^3)$ between the density at the times $t$=3.5 fs and $t$=0 fs are shown for CEP=0, $\pi/2$ and $\pi$ for circular polarization as indicated. (Adapted from Ref. [55])

## 4.3   Conclusions and outlook

To conclude, the transient electronic dynamics in a large polyatomic system, i.e. $C_{60}$, have been experimentally and theoretically investigated for intense near single-cycle laser pulses. The quantum simulations show that the laser-induced electronic wave packet motion in $C_{60}$ can be probed by angular-resolved photoelectron spectroscopy. The asymmetry of the photoelectrons from direct ionization can reflect the localization of the coherent electron density at the time of ionization. Classical simulations based on the simple-man's model are also performed and show that the rescattering is well described in both theoretical methods. However, the directional emission of the 'direct' electrons is only well reproduced by the quantum simulations. Our results demonstrate that the electron wave packet motion and thus the spatial electron localization in $C_{60}$ can be steered by the CEP and polarization of the intense few-cycle laser pulses. Another important observation is the yield of rescattered electrons from interaction with circularly polarized pulses. The MC simulations reveal that these electrons are from multiple small-angle collisions with the $C_{60}$ shell, which is expected to be a general recollision mechanism for such complex molecular systems.

Theoretically, with state-of-the-art calculation capabilities, quantum dynamical simulations can be performed on $C_{60}$. This is already a great achievement. However, the current model did not well represent the Coulomb interaction between the ionized electron and the cationic core which results in a large discrepancy in the low energy photoelectron yield between theory and experiment. This can be addressed in the near future. On the other hand, the recollision mechanism which we extracted from $C_{60}$ in circularly polarized laser field will likely also play a role in other complex systems, such as large molecules, nanoclusters, nanoparticles, and *etc.*. This still needs to be verified.

Fullerenes are ideal systems for the exploration of new phenomena and mechanisms. For instance, recent theoretical work performed on $C_{60}$ predicted that spectral minima in certain energy range carrying information about dynamical correlations and spatial information [147], which can be experimentally verified via attosecond RABBIT (reconstruction of attosecond beating by interference of two-photon transitions) interferometry. Furthermore, it is an interesting research direction to 'watch' the ultrafast structural dynamics in molecules. Conventional methods based on diffraction and absorption using electrons or X-rays can achieve sub-Angstrom spatial resolutions, but the time resolution is restricted to the order of picoseconds [148, 149, 150]. Recently, Blaga and coworkers developed a new technique using laser-induced electron diffraction (LIED) to reach sub-Angstrom and femtosecond resolution [151, 152]. Intense femtosecond laser pulses with wavelengths in the mid-infrared range are utilized to generate energetic rescattering electron wavepackets, which are used to probe the instantaneous molecular structure. The information of differential cross section (DCS) can be extracted from the fixed-energy angle-swept LIED measurement, and bond-lengths can be derived afterwards. Alternatively, another approach of fixed-angle broadband laser-driven electron scattering (FABLES) is proposed

which can provide similar bond-length information with much faster measurement and processing [153]. Therefore FABLES has the potential to be developed with a pump-probe technique to image molecular structural changes. We expect these techniques can be tested on $C_{60}$ in the future to explore e.g. the breathing motion in such a complex system.

# Chapter 5

# Directional electron emission from expanding nanoplasmas in dual pulses

In the previous chapters, the response of atoms and molecules interacting with tailored few-cycle laser fields was studied. As we move to complex molecular systems, such as $C_{60}$, the coherent collective electronic dynamics shows new properties as compared to atoms and simple molecules. For even larger systems such as gas-phase clusters, the strong field induced processes can be investigated in the transition regime between the molecular and solid phase. When exposed to a strong laser field, clusters can generate a transient nano-plasma with almost solid density, providing a unique system for the investigation of electronic dynamics.
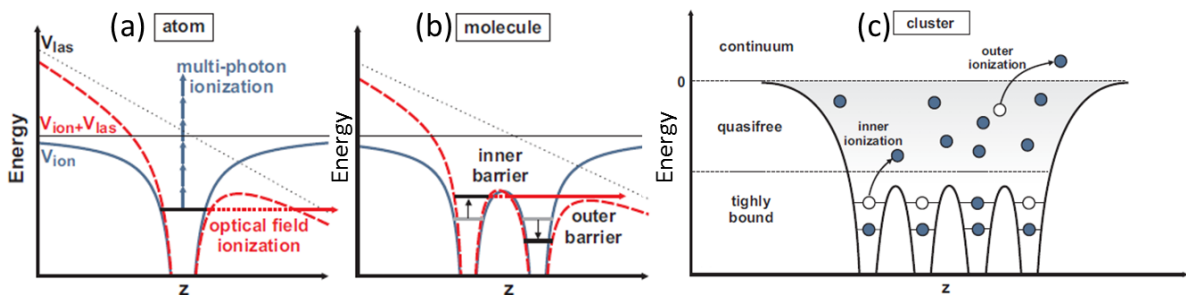


Figure 5.1: A schematic view of the ionization mechanisms in (a) atoms, (b) molecules and (c) clusters. (Adapted from Ref. [154])

For moderately strong laser field in the intensity range of $10^{13}$-$10^{14}$ W cm$^{-2}$, the ionization mechanism exhibits distinctive properties for atoms, molecules and solids. Compared to atoms, structural properties become increasingly important for extended systems. Fig. 5.1 shows a schematic comparison of the ionization mechanisms in atoms, molecules and clusters. On the atomic level, a bound electron can be ionized directly by single- or multi-

photon absorption and generate characteristic peaks in the electron spectra separated by one photon energy. Or, an electron can be tunneling ionized in a rapidly oscillating optical field, as indicated by the red dashed curves in Fig. 5.1 (a) and (b). The relative significance of multiphoton ionization and tunneling ionization can be quantitatively described by the Keldysh parameter $\gamma$ [29]. For molecules and more complex systems, the structural details become important. An example is charge-resonance-enhanced-ionization (CREI) [155], as shown in Fig. 5.1 (b). An appropriate internuclear separation is required for a simultaneous lowering of both the inner and the outer potential barriers, giving rise to an enhanced ionization rate. For larger or smaller separations, either the inner or the outer barrier increases and the ionization probability will be reduced. For even larger systems such as clusters, the electrons can be classified as tightly bound, quasifree and continuum electrons, as shown in Fig. 5.1 (c). The concepts of inner and outer ionization are introduced for clusters [156]. Inner ionization means the excitation of a tightly bound electron to the conduction band. This is equivalent to remove an electron from its host ion, but the electron is still bound to the cluster. Outer ionization is the excitation of the electron to the continuum, corresponding to a net ionization of the system.
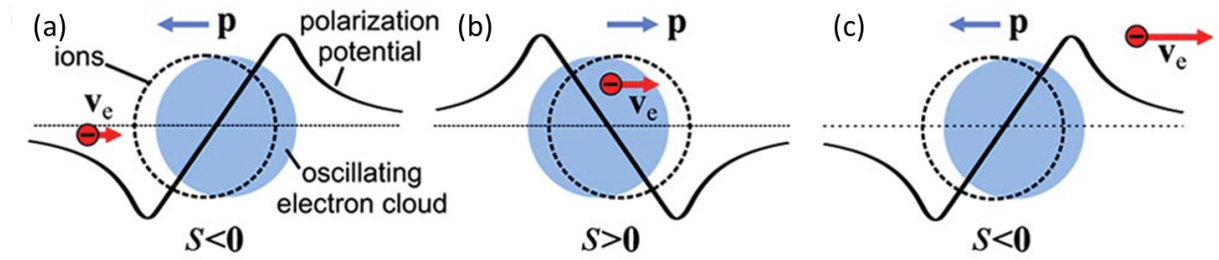


Figure 5.2: Schematics of the SPARC mechanism. Energetic electrons can be generated in a three-step energy gain, each on a time scale of half a plasmon cycle. The electrons leave the cluster and then return at zero plasmon excursion and pass the cluster during a favorable plasmon half-cycle. The highest energy capture requires a flipping of the polarization. (Taken from Ref. [157])

Among the variety of interesting properties of strong-field light-cluster interactions, the plasmonic resonance in clusters has drawn many attentions. Early studies have shown that a temporary resonant collective mode in clusters can lead to a significantly enhanced absorption, resulting in increased yields of electrons and high charge state ions [158, 159, 160]. Electron emission with high maximum kinetic energies has also been observed in medium-sized clusters exposed to dual 100 fs pulses which can be explained by surface-plasmon-assisted rescattering in clusters (SPARC) [157]. As depicted in Fig. 5.2, the energetic electrons experience three steps of energy gain. Each step takes half of a plasmon cycle. The electron has to leave, return to, and transit through the cluster during favorable times to gain maximum energies. Due to these constraints in the SPARC mechanism, energetic electrons can be only ejected in sub-cycle bursts. This promises the possibility to control the acceleration process with the CEP of few-cycle pulses. Another work has investigated

the angular-resolved electron emission from the plasmonic electron acceleration in silver clusters both experimentally and theoretically [161]. However, the CEP-dependence of these electron emissions has not been reported yet. In this chapter, the directionality of the electron emission from medium sized silver clusters are studied when interacting with moderately intense dual NIR pulses. Clear indication of the transient plasmon resonance has been found and the different phase offsets of the asymmetry for low energy electrons at different stages of the expanding plasma may provide a tool to detect the instantaneous local field.

## 5.1 Theoretical background

To understand the interaction of nanosized objects with few-cycle laser pulses, the macroscopic Maxwell equations are applied. If the material is magnetic and/or polarizable, the Maxwell equations in the differential form [162] are:

$$\begin{aligned}
\bigtriangledown \cdot \mathbf{D} &= \rho \\
\bigtriangledown \cdot \mathbf{B} &= 0 \\
\bigtriangledown \times \mathbf{E} &= -\frac{\partial \mathbf{B}}{\partial t} \\
\bigtriangledown \times \mathbf{H} &= \mathbf{J} + \frac{\partial \mathbf{D}}{\partial t}.
\end{aligned} \tag{5.1}$$

Here $\mathbf{D}$ is the electric displacement, $\mathbf{B}$ is the magnetic field, $\mathbf{E}$ is the electric field, $\mathbf{H}$ is the magnetic field strength, $\rho$ and $\mathbf{J}$ are the external charge density and current. For isotropic and non-magnetic materials with linear response, the constitutive relations are as follows

$$\begin{aligned}
\mathbf{D} &= \varepsilon \mathbf{E} = \varepsilon_0 \mathbf{E} + \mathbf{P} \\
\mathbf{B} &= \mu \mathbf{H} = \mu_0 \mathbf{H}.
\end{aligned} \tag{5.2}$$

Here $\varepsilon$ and $\mu$ are the permittivity and permeability in the media. $\varepsilon_0$ and $\mu_0$ are the permittivity and permeability in free space. $\mathbf{P}$ is the polarization which is from the effective separation of the charges in the medium induced by the electric field. If the material is uniform, we can introduce the relative permittivity which is defined as $\varepsilon_r = \varepsilon/\varepsilon_0$.

If the field and the induced current are homogeneous, their relationship is given by the Ohm's law as,

$$\mathbf{J} = \frac{\partial \mathbf{P}}{\partial t} = \sigma \mathbf{E} \tag{5.3}$$

where $\sigma$ is the conductivity.

Generally, the relative permittivity is frequency dependent. For the case of metal materials, one can utilize the Drude model which assumes that the microscopic behavior of electrons in a metal can be treated as a free electron gas. Then the dielectric function can be derived as

$$\varepsilon_r(\omega) = 1 - \frac{\omega_p^2}{\omega^2 + i\gamma_e\omega}. \tag{5.4}$$

Here $\omega$ is the frequency of the external electric field, $\gamma_e$ is the collision frequency of the electrons, and $\omega_p$ is the plasma frequency which is given by

$$\omega_p = \sqrt{\frac{n_e e^2}{\varepsilon_0 m_{eff}}}. \tag{5.5}$$

Here $e$ is the charge of electron, $n_e$ is the number of electrons in the medium with an effective mass of $m_{eff}$. In the Drude model, the only interaction is taken into account of a free electron with its environment is via instantaneous collisions. For the real cases, inter- and intra-band transitions also need to be taken into account.

### 5.1.1 Mie theory for spherical objects
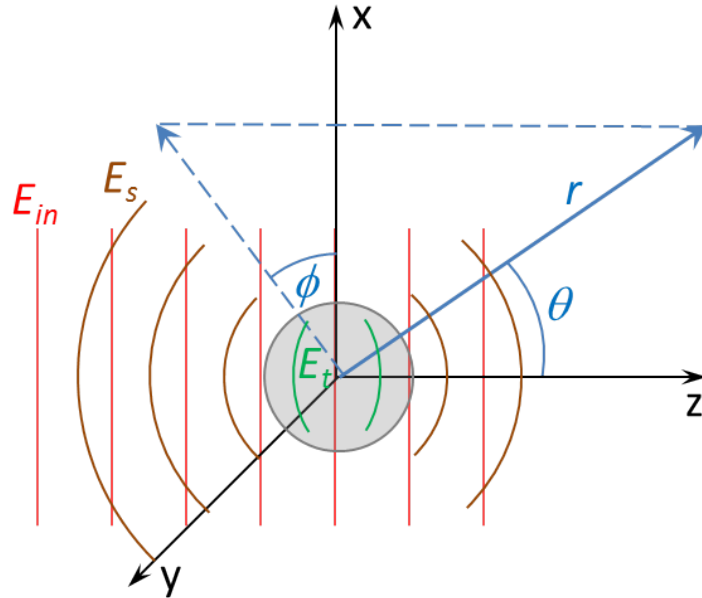


Figure 5.3: The schematic drawing of the conventions for Mie theory. The incident wave ($E_{in}$) propagates towards +z direction and the wavefront is represented by the red lines. The scattered light ($E_s$) is represented by the brown curves and the transmitted light ($E_t$) inside the sphere is represented by the green curves. The spherical coordinates are shown with $r$ (radial distance), $\theta$ (polar angle) and $\phi$ (azimuthal angle).

When a beam of electromagnetic waves is incident on an object, the light will be partly scattered by the object, and part of the waves can be transmitted into the object. The scattered field usually carries the characteristics of the target. Here, we introduce the

simplest geometry, i.e., a spherical target. For this special case, Mie theory [163] presents the solution for the interaction of an electromagnetic wave with a sphere of radius $R$ in a homogeneous medium.

The wave equations can be derived from Eq. 5.1 and have the following form

$$
\begin{aligned}
\bigtriangledown^2 \mathbf{E} + k^2 \mathbf{E} &= 0, \\
\bigtriangledown^2 \mathbf{H} + k^2 \mathbf{H} &= 0.
\end{aligned}
\tag{5.6}
$$

Here $k$ is the wavenumber and is defined as $k = \omega\sqrt{\varepsilon\mu}$, $\omega$ is the frequency of the incident field.

The electric and magnetic fields are divergence free due to zero charge density. Therefore we have

$$
\begin{aligned}
\bigtriangledown \cdot \mathbf{E} &= 0, \\
\bigtriangledown \cdot \mathbf{H} &= 0.
\end{aligned}
\tag{5.7}
$$

Besides, the Faraday's and Ampere's laws are expressed as

$$
\begin{aligned}
\bigtriangledown \times \mathbf{E} &= i\omega\mu\mathbf{H}, \\
\bigtriangledown \times \mathbf{H} &= -i\omega\varepsilon\mathbf{E}.
\end{aligned}
\tag{5.8}
$$

As shown in Fig. 5.3 , the field outside the sphere includes an incident plane wave component $\mathbf{E}_{in}$ and a scattered part $\mathbf{E}_s$. The internal field inside the sphere can be denoted as the transmitted field $\mathbf{E}_t$. All the field quantities inside and outside the spherical object should satisfy Eqs. 5.7 and 5.8.

Now we introduce two vector functions,

$$
\begin{aligned}
\mathbf{M} &= \bigtriangledown \times (\mathbf{r}\psi), \\
\mathbf{N} &= \bigtriangledown \times \mathbf{M}/k.
\end{aligned}
\tag{5.9}
$$

Here $\mathbf{r}$ is a constant vector, and $\psi$ is a scalar function. $\mathbf{M}$ and $\mathbf{N}$ are divergence free.

$$
\begin{aligned}
\bigtriangledown \cdot \mathbf{M} &= 0, \\
\bigtriangledown \cdot \mathbf{N} &= 0.
\end{aligned}
\tag{5.10}
$$

Now we apply the operator $(\bigtriangledown^2 + k^2)$ to $\mathbf{M}$:

$$
\bigtriangledown^2 \mathbf{M} + k^2 \mathbf{M} = \bigtriangledown \times (\mathbf{r}(\bigtriangledown^2\psi + k^2\psi)).
\tag{5.11}
$$

Comparing Eqn. 5.11 with Eqn. 5.6, if $\bigtriangledown^2\psi + k^2\psi = 0$ can be satisfied, $\mathbf{M}$ and $\mathbf{N}$ are equivalent to the electric and magnetic field. Then the problem of solving the wave equations is transferred to solve the scaler equation about $\psi$. $\psi$ is called the 'generating function' and $\mathbf{r}$ is the 'guiding vector'.

Spherical coordinates are more convenient for such a geometry. The scalar wave equation in spherical coordinates is given by

$$\frac{1}{r^2}\frac{\partial}{\partial r}\left(r^2\frac{\partial \psi}{\partial r}\right) + \frac{1}{r^2 \sin\theta}\frac{\partial}{\partial\theta}\left(\sin\theta\frac{\partial\psi}{\partial\theta}\right) + \frac{1}{r^2\sin\theta}\frac{\partial^2\psi}{\partial\phi^2} + k^2\psi = 0, \tag{5.12}$$

assuming that the variables are separable

$$\psi(r,\theta,\phi) = R(r)\Theta(\theta)\Phi(\phi). \tag{5.13}$$

Introducing Eqn. 5.13 to Eqn. 5.12, the complete solution of the scalar wave equation is given by

$$\begin{aligned}
\psi_{emn}(r,\theta,\phi) &= \cos(m\phi)P_n^m(\cos\theta)z_n(kr), \\
\psi_{omn}(r,\theta,\phi) &= \sin(m\phi)P_n^m(\cos\theta)z_n(kr).
\end{aligned} \tag{5.14}$$

where the 'e' and 'o' in the subscripts stand for even and odd, respectively. $P_n^m$ are the associated Legendre functions of the first kind. $z_n$ represents any of the four spherical Bessel functions $j_n, y_n, h_n^{(1)}$ or $h_n^{(2)}$. Thus the solution of the scalar wave equation can be expressed as an infinite series of Eqn. 5.14. Then the solutions for the electric and magnetic fields can be written as

$$\begin{aligned}
\mathbf{M}_{emn} &= \bigtriangledown \times (\mathbf{r}\psi_{emn}), \\
\mathbf{M}_{omn} &= \bigtriangledown \times (\mathbf{r}\psi_{omn}), \\
\mathbf{N}_{emn} &= \bigtriangledown \times (\mathbf{r}\psi_{emn})/k, \\
\mathbf{N}_{omn} &= \bigtriangledown \times (\mathbf{r}\psi_{omn})/k.
\end{aligned} \tag{5.15}$$

Now let's assume the incident field is a plane wave linearly polarized in the x-direction, which can be expressed as

$$\mathbf{E}_{in} = E_0 e^{-ikr\cos\theta}\hat{e}_x, \tag{5.16}$$

where $E_0$ is the amplitude of the electric field, $k$ is the wavenumber, $\hat{e}_x$ is the unit vector in x-direction, which is given in spherical coordinates as

$$\hat{e}_x = \sin\theta\cos\phi\hat{e}_r + \cos\theta\cos\phi\hat{e}_\theta - \sin\theta\hat{e}_\phi. \tag{5.17}$$

Then the incident field can be expressed as an infinite series of Eqn. 5.15, which is given by

$$\mathbf{E}_{in} = \sum_{m=0}^{\infty}\sum_{n=m}^{\infty}(B_{emn}\mathbf{M}_{emn} + B_{omn}\mathbf{M}_{omn} + A_{emn}\mathbf{N}_{emn} + A_{omn}\mathbf{N}_{omn}). \tag{5.18}$$

Here, $B_{emn}$, $B_{omn}$, $A_{emn}$, and $A_{omn}$ are the expansion coefficients.

Using the orthoganality of the vector harmonics ($\mathbf{M}$ and $\mathbf{N}$) and the finiteness of the incident beam $\mathbf{E}_{in}$ at the origin, Eqn. 5.18 can be reduced to

$$\mathbf{E}_{in} = \sum_{n=1}^{\infty}(B_{o1n}\mathbf{M}_{o1n}^{(1)} + A_{e1n}\mathbf{N}_{e1n}^{(1)}). \tag{5.19}$$

The superscript '(1)' means that the spherical Bessel function $j_n(kr)$ is used for the radial part of the generating function, which can make sure that the incident field is finite at the origin. The expansion coefficients can be derived as

$$\begin{aligned} B_{o1n} &= i^n E_0 \frac{2n+1}{n(n+1)}, \\ A_{e1n} &= -i^n E_0 i \frac{2n+1}{n(n+1)}. \end{aligned} \tag{5.20}$$

Then the incident field can be expressed as

$$\mathbf{E}_{in} = E_0 \sum_{n=1}^{\infty} i^n \frac{2n+1}{n(n+1)}(\mathbf{M}_{o1n}^{(1)} - i\mathbf{N}_{e1n}^{(1)}). \tag{5.21}$$

The corresponding magnetic field is

$$\mathbf{H}_{in} = -\frac{k}{\varepsilon\mu} E_0 \sum_{n=1}^{\infty} i^n \frac{2n+1}{n(n+1)}(\mathbf{M}_{e1n}^{(1)} + i\mathbf{N}_{o1n}^{(1)}). \tag{5.22}$$

The scattered field and the transmitted field inside the particle can be obtained from the following boundary conditions:

$$\begin{aligned} (\mathbf{E}_{in} + \mathbf{E}_s - \mathbf{E}_t) \times \hat{e}_r &= 0, \\ (\mathbf{H}_{in} + \mathbf{H}_s - \mathbf{H}_t) \times \hat{e}_r &= 0. \end{aligned} \tag{5.23}$$

Then the scattered and the transmitted fields can be derived as

$$\begin{aligned} \mathbf{E}_s &= \sum_{n=1}^{\infty} E_n(ia_n\mathbf{N}_{e1n}^{(3)} - b_n\mathbf{M}_{o1n}^{(3)}), \\ \mathbf{E}_t &= \sum_{n=1}^{\infty} E_n(c_n\mathbf{M}_{o1n}^{(1)} - id_n\mathbf{N}_{e1n}^{(1)}). \end{aligned} \tag{5.24}$$

Here the superscript '(3)' means that the radial part of $\psi$ is given by the spherical Hankel function $h_n^{(1)}$. Now we get the Mie coefficients $a_n$, $b_n$, $c_n$, and $d_n$. The analytical expressions

for the coefficients are

$$a_n = \frac{m^2 j_n(m\rho)(\rho j_n(\rho))' - j_n(\rho)(m\rho j_n(m\rho))'}{m^2 j_n(m\rho)(\rho h_n(\rho))' - h_n(\rho)(m\rho j_n(m\rho))'}, \tag{5.25}$$

$$b_n = \frac{j_n(m\rho)(\rho j_n(\rho))' - j_n(\rho)(m\rho j_n(m\rho))'}{j_n(m\rho)(\rho h_n(\rho))' - h_n(\rho)(m\rho j_n(m\rho))'}, \tag{5.26}$$

$$c_n = \frac{j_n(\rho)(\rho h_n(\rho))' - h_n(\rho)(\rho j_n(\rho))'}{j_n(m\rho)(\rho h_n(\rho))' - h_n(\rho)(m\rho j_n(m\rho))'}, \tag{5.27}$$

$$d_n = \frac{m j_n(\rho)(\rho h_n(\rho))' - m h_n(\rho)(\rho j_n(\rho))'}{m^2 j_n(m\rho)(\rho h_n(\rho))' - h_n(\rho)(m\rho j_n(m\rho))'}. \tag{5.28}$$

Here $j_n$ is the $n$-th spherical Bessel function of the first kind, $h_n$ is the $n$-th spherical Hankel function of the first kind, $m$ is the relative refractive index which is given by $m = n_l/n$ where $n_l$ and $n$ are the refractive index of the sphere and the surrounding medium. $\rho$ is the size parameter and is given by $\rho = kR$.

## 5.1.2　Dipole approximation
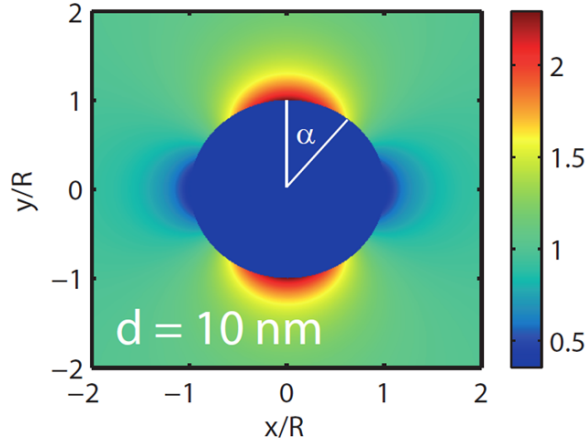


Figure 5.4: The field distribution of $E_y$ in the plane $z = 0$ at an Au sphere with a diameter of d=10 nm. The incident laser field was assumed to have a wavelength of 720 nm and linearly polarized along y-direction. (Taken from Ref. [38].)

In principle, Mie theory is valid for all particle sizes and all incident wavelengths. For a special case of very small particles (compared to the incident wavelength), the dipole approximation can be employed. For $\rho << \lambda$, the expressions of the Mie coefficients in Eqn. 5.25 are reduced to only the first order with $n = 1$. Here, we are only interested in the electric fields. Applying $n = 1$, the electric field inside and outside the spherical object

can be derived as

$$\mathbf{E}_{ins}(\mathbf{r}) = \frac{3\epsilon_m}{\epsilon_r + 2\epsilon_m}E_0,$$

$$\mathbf{E}_{out}(\mathbf{r}) = E_0 + \frac{3\hat{\mathbf{r}}(\hat{\mathbf{r}} \cdot \mathbf{p}) - \mathbf{p}}{4\pi\epsilon_0\epsilon_m} \cdot \frac{1}{r^3}. \tag{5.29}$$

Here $\hat{\mathbf{r}}$ is the unit vector of the radial coordinate, $\epsilon_m$ and $\epsilon_r$ are the relative permittivity of the surrounding medium and the target. $\mathbf{p}$ is the effective polarization of the object and is given by

$$\mathbf{p} = 4\pi\epsilon_0\epsilon_m R^3 \frac{\epsilon_r - \epsilon_m}{\epsilon_r + 2\epsilon_m}\mathbf{E_0}. \tag{5.30}$$

For metals, the real part of $\epsilon_r$ is usually negative while their imaginary part is usually positive. Therefore there exists resonant condition for Eqn. 5.29 and 5.30, which is called 'Fröhlich condition' [164]. For the wavelenghs in the visible region, the dipole approximation can describe with good accuracy the optical response of spherical objects with diameter much smaller than 100 nm. An example is shown in Fig. 5.4 of an Au nanoparticle with a diameter of 10 nm. The incident light is monochromatic at a wavelength of 720 nm and linearly polarized along the y-direction. The field distribution of the $E_y$ component shows enhancement near the two poles of the object along the y-axis. The strength of the enhancement is related to the light wavelength, the relative permittivity of the object, the particle size, *etc.*. For increasing particle sizes, the dipole approximation is not valid anymore and geometric effects and wave propagation effects will take place [59].

## 5.2    Steering electron emission from nanoclusters with dual laser pulses

The directionality of electron emission from expanding silver nanoplasma is investigated under dual pulses for laser intensities on the order of $10^{13}$ W cm$^{-2}$. Resonant plasmon excitation for optimal delays is observed and the asymmetry parameter shows delay-dependent phase offsets for the electron emission with low kinetic energies.

### 5.2.1    Experimental Technique
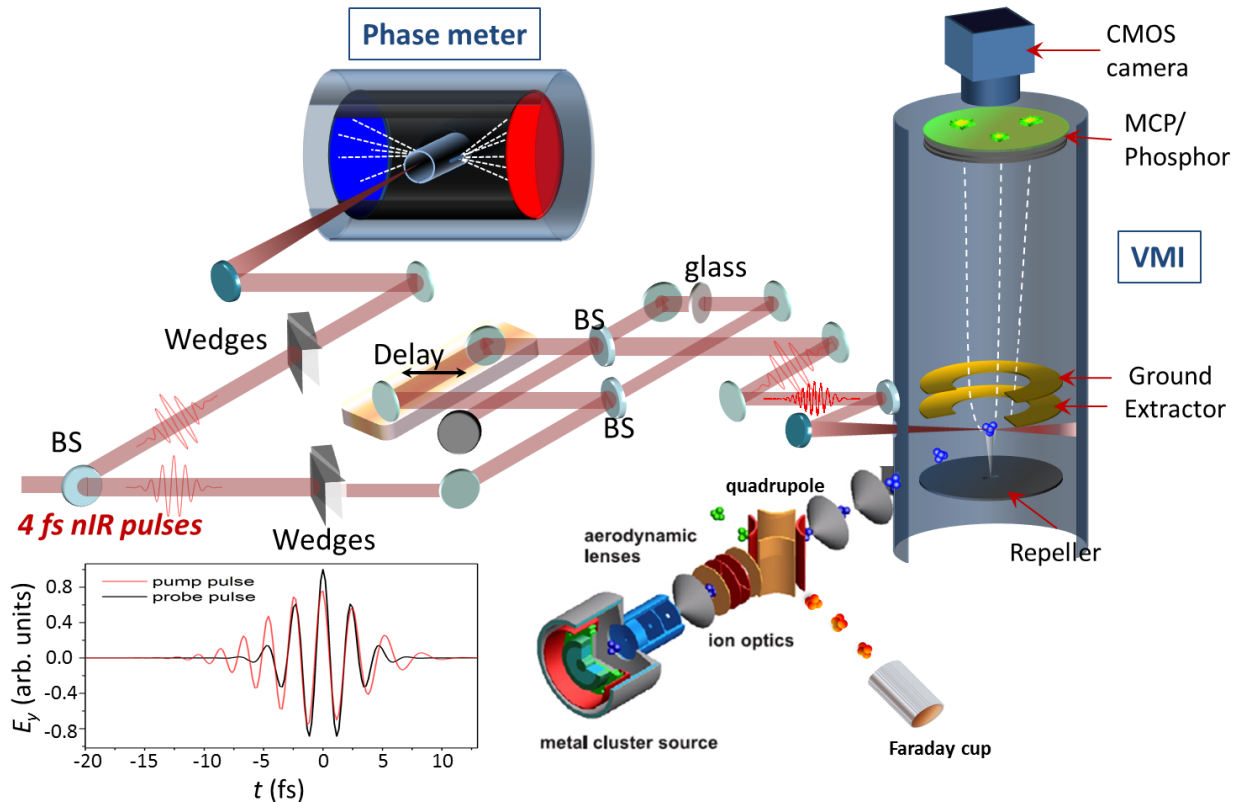


Figure 5.5: A schematic drawing of the experimental apparatus for the investigation of electron emission from silver clusters interacting with dual laser pulses (the part of the cluster source is adapted from Ref. [161]). The inserted figure at the left bottom corner illustrates the time evolution of the electric fields for both the pump and the probe pulses. The probe pulse (black curve) is a 4 fs NIR pulse at 720 nm with a Gaussian envelope (CEP=0). The pump pulse (red curve) is calculated from a 4 fs pulse propagating through a 0.5 mm thick fused silica plate. The pump pulse is chirped and the duration is about 10 fs.

A pump-probe experimental scheme combined with CEP-tagging is utilized for investigating the directionality of the electron emission from the expanding nanoplasmas. The pump beam is a chirped pulse with a duration of about 10 fs which is used to pre-ionize the silver clusters. After the pre-ionization the nanoclusters expand resulting in a slow decrease (ps time scale) of the charge density $\rho_{ion}$ and corresponding red-shift of the plasmon resonance frequency $\omega_p$ (Eq. 5.5). A beam of 4 fs few-cycle Fourier transform limited (FTL) pulses serves as the probe beam.

The experimental setup is shown in Fig. 5.5 with the electric fields of the pump and probe pulses shown in the inserted figure at the left bottom corner. The single-shot CEP-tagged VMI system and the nanocluster source were introduced in detail in Chapter 2. Briefly, a beam of 4 fs few-cycle pulses is split into two parts by a 20/80 broadband beamsplitter. The small portion is sent to the stereo-ATI phasemeter for measuring the CEP of every laser shot. The larger part is sent into a Mach-Zehnder interferometer to generate delay-controlled dual pulses. The pump pulse is temporally stretched and chirped by a slab of fused silica with a thickness of 0.5 mm. The resulting chirped pulse is estimated to have a duration of around 10 fs with a peak intensity decreased by a factor of about 50% compared to the FTL pulse. The probe beam path length was adjusted with a computer controlled linear translation stage. A peak intensity of about $(2\sim3)\times10^{13}$ W cm$^{-2}$ can be obtained for the probe pulse which is estimated from a reference scan on electron emission from background gases. The intensity for the stretched pump pulse is about half of the probe intensity. The laser beams are linearly polarized. The silver clusters interact with the dual pulses and the resulting electron emission is detected by the single-shot VMI spectrometer. Large efforts have been made to obtain a high target density in the interaction region which can be realized by optimizing multiple operation parameters of the cluster source. The cluster size distributions were monitored by the quadrupole mass spectrometer and can be estimated to peak at about $3\sim4$ nm in diameter (at an average applied voltage of about $\pm140$ V on the QMS electrodes). This corresponds to thousands of silver atoms per cluster [161]. Several delays around the plasmon resonance are selected for the measurements on the CEP-dependent electron emission.

## 5.2.2   CEP-dependence of the electron emission from expanding silver nanoplasmas

Single-shot VMI detection of the electron emission from nanoclusters allows for an effective deduction of the background signal in the accumulated momentum images [12]. The number of electrons emitted from a nanocluster is typically much larger than the ATI electron emission from the background gases. Due to a limited target density in the interaction volume, typically 0-1 nanoclusters can be hit in a single laser shot. Consequently, a significant number of the single-shot VMI images contain only background ATI signal. Fig. 5.6 (a) shows histograms of the event count for the measurement with nanoclusters at different delays between the pump and the probe pulses. Since the background produces a relatively low number of electrons per shot, the histogram can be divided into images with
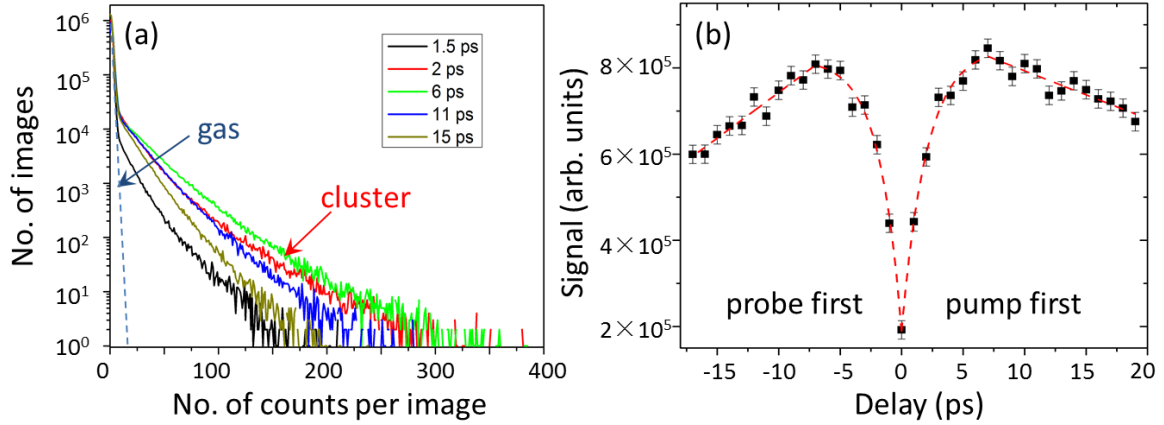
Figure 5.6: (a) Histogram of the electron signal for several delays at 1.5, 2, 6, 11, and 15 ps. (b) The yield of electrons from silver nanoclusters as a function of delay time between the pump and the probe pulse. The black squares are experimental data. The red dashed curve is a fitting curve with an exponential grow and decay function.

low number of counts per frame (marked by the blue dashed curve which including major contributions from the background gases) and data with higher count rates. By selecting the frames with event numbers larger than a chosen threshold value the background contributions can be dramatically suppressed. Fig. 5.6 (b) shows the plot of the electron yield from silver nanoclusters as a function of delay time. The pump pulse arrives first and pre-ionizes the silver nanoclusters for positive delays. The total electron yield from the clusters exhibits clear delay-dependence in the present dual-pulse configuration. The resonance at the delay of about 6∼7 ps can be recognized by the higher electron yield. About 4 times higher signal can be obtained at resonance compared to the signal close to zero time delay. Note that the electron emission at the exact zero delay time is not in the plot. The expanding time of the plasma system to reach the critical density which is resonant with the external electric field depends on the cluster size and the laser intensity. As shown in Fig. 5.6 (b), the red dashed curve is the fitting result for the measured data with an exponential grow and decay function. The fitting results show that the critical delay time (i.e. the expanding time of the plasma to reach resonance) for the positive delay part is about 0.2 ps later than the negative part. This is due to the fact that the chirped pump pulses with lower peak intensity pre-ionize the silver clusters for the positive delays, which requires a longer time for the plasma to reach resonance. The laser intensity is selected such that the ionization rate of the background gases can be maintained at a very low level.

Five time delays are selected for the CEP-tagging measurements. They are 1.5, 2, 6, 11, and 15 ps, where 6 ps is the time delay closest to the resonance condition. The histograms for the five selected time delays are shown in Fig. 5.6 (a). As indicated in the figure, the signal originating from background gases dominates for the count rates per image below

20, while the count rate for cluster signals extends to much higher value at hundreds of counts. We can see that the signals from gases show no apparent difference for the five delay times, while the signal from clusters show clear delay-dependence.
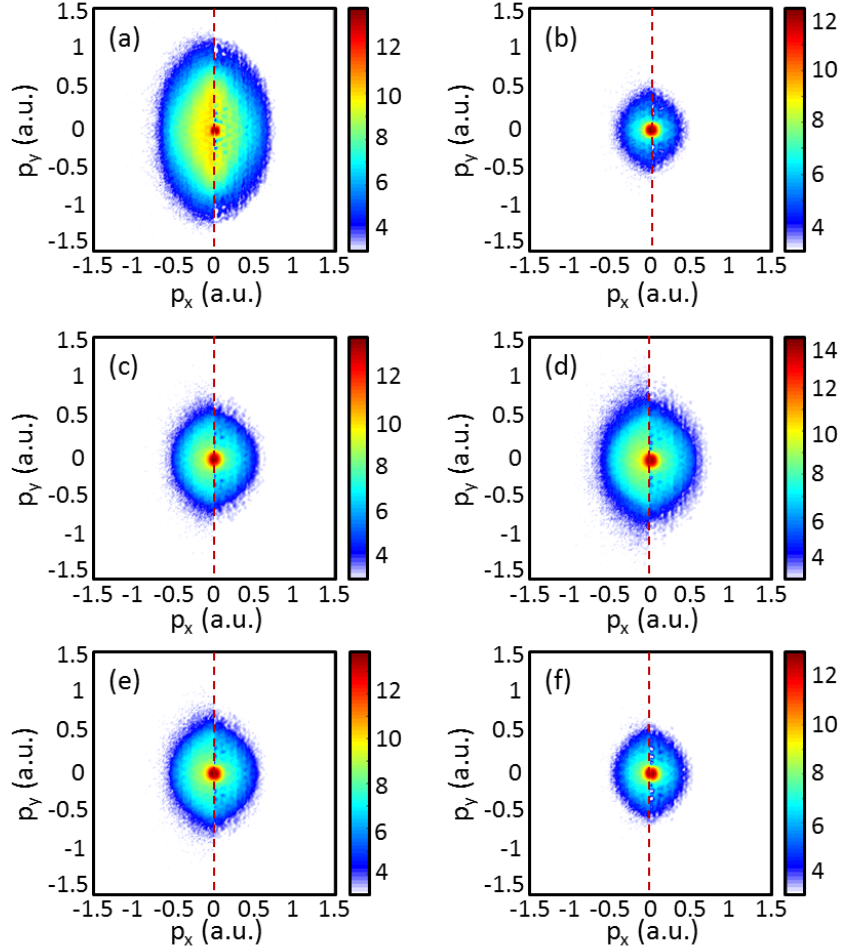


Figure 5.7: The VMI images for the electron emission dominated by background gas (a) and from silver nanoclusters (b-f) for time delays at 1.5, 2, 6, 11, 15 ps, respectively. The raw VMI images are shown at the left side while the inverted images are shown at the right side. The polarization axis is along the y-direction.

This plot also shows that the total electron yield is the maximum at resonance (delay=6 ps) with the largest area below the histogram curve. According to the histograms, the VMI images are resorted by count rates. The VMI images for electron emission from nanoclusters (count rate > 20) and the images which are dominated by background gases (count rate ≤ 20) are shown in Fig. 5.7. The raw VMI images are shown at the left side and the inverted images are shown at the right side for each plot.
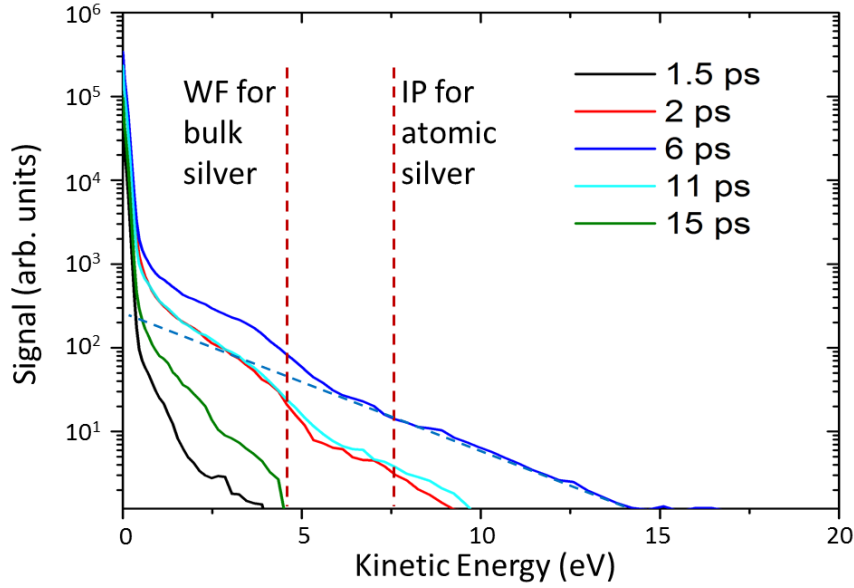
Figure 5.8: The kinetic energy spectra for the photoelectron from silver clusters obtained at delays of 1.5, 2, 6, 11 and 15 ps, respectively.

In Fig. 5.7 (a), the VMI image is dominated by photoelectrons from background gases. All the background gas images at different time delays are consistent. Therefore only one image is shown here, which is comparable to earlier studies [58, 57]. However, the electron momentum distributions from nanoclusters at different time delays exhibit different signatures, as shown in Fig. 5.7 (b-f). These images exhibit an almost isotropic momentum distribution for most of the momenta, and a strong signal close to zero momentum. The cutoff momentum changes for different delays and reaches a maximum at the resonance (around 6 ps). Combined with Fig. 5.6 (a), it is shown that the highest electron yield and the most energetic electrons are generated at the delay of about 6 ps. However, the 'energetic electrons' mentioned here do not campare to what was reported in previous experiments where electron kinetic energy up to 100 $U_p$ can be obtained [38, 161]. The cutoff energy at around resonance is about 15 eV in our experiment, corresponding to only 10 $U_p$. One reason may be that the 100 $U_p$ cutoff energy was obtained with a laser intensity in the order of $10^{14}$ W cm$^{-2}$. The intensity used in our experiment is lower by about one order of magnitude, therefore the ratio of the cutoff energy over $U_p$ could be lower [38]. Another reason may be that the VMI spectrometer provides limited detection dynamics range such that the high energy electrons have too little statistics to be detected.

Fig. 5.8 shows the kinetic energy spectra for the electron emission from silver clusters which are obtained by integrating the inverted VMI images on Fig. 5.7 (b-f) within an angle range of $\pm 20°$ along the polarization axis. The spectra exhibit a strong peak close to zero momenta and a prominent peak structure in the energy region below the ionization
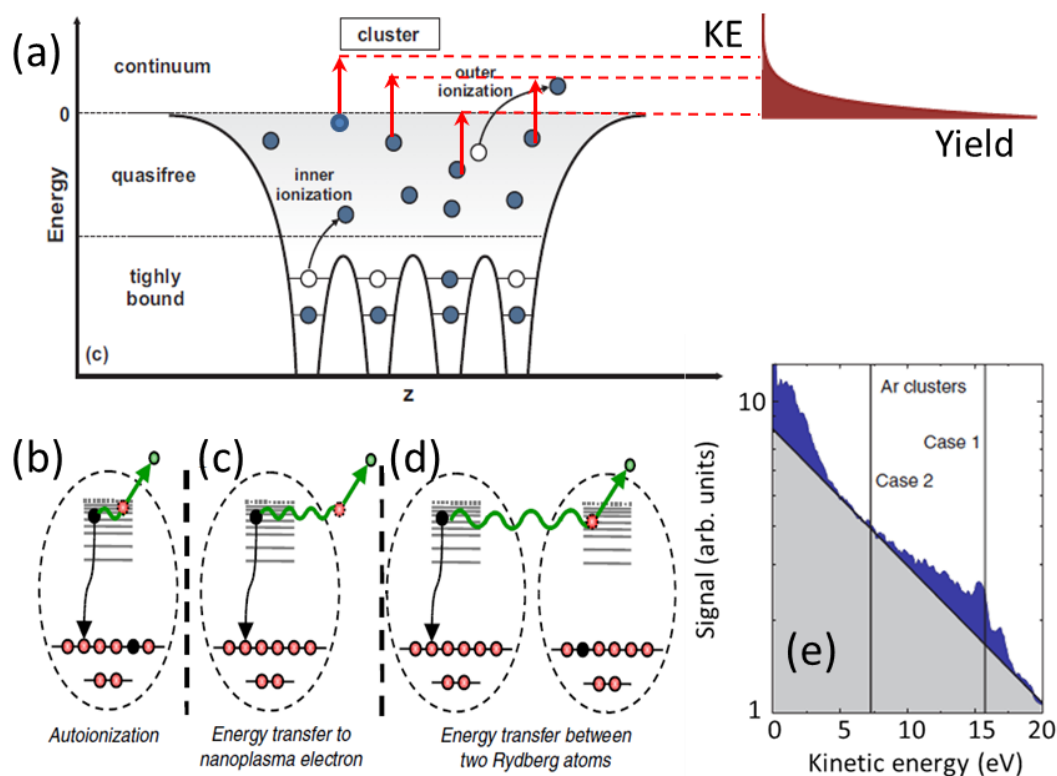
Figure 5.9: (a) The schemetic drawing of the mechanism of single-photon outer ionization in clusters. (Adapted from Ref. [154]) (b-d) Mechanisms of CED in clusters. (Adapted from Ref. [165]) (e) Electron kinetic energy spectrum of Ar clusters after NIR ionization at an intensity of $1\times10^{14}$ W cm$^{-2}$. The peak for 'Case 1' close to the IP of atomic Ar is attributed to a CED process involving two weakly bound Rydberg electrons. The peak for 'Case 2' is attributed to a decay process involving two Ar (4s) atoms.

potential (IP). The strong peak close to zero momenta (corresponding to the strong signal close to the center on the VMI images) can be from thermal ionization or single-photon outer ionization induced by the weak pedestal of the laser pulse, as depicted in Fig. 5.9 (a). Or, it can also come from ionization by the DC-field of the VMI spectrometer. Investigations based on molecular dynamics simulations have shown that the pump pulse can increase the inner ionization substantially and generate many quasi-free electrons within the clusters [161]. The later coming probe pulse can enhance the outer ionization significantly. The enhancement is about two orders of magnitude at resonance [161]. The quasifree electrons in the cluster can easily absorb one NIR photon and being ionized to the continuum, which results in a spectral peak below one photon energy. We can see in Fig. 5.7 and Fig. 5.8 that this strong signal at very low kinetic energy does not show a clear delay-dependence. Another interesting characteristics is the peak structure below IP,

which has never been reported for metal nanoclusters interacting with intense NIR laser pulses. Recent work showed that the correlated electron decay (CED) in expanding rare-gas clusters triggered by intense NIR fields can generate similar spectral signatures [165]. As shown in Fig. 5.9 (b-d), CED involves the relaxation of two Rydberg state electrons and transfer of the available electronic energy to the adjacent Rydberg electron (Fig. 5.9 (b)), or to a quasi-free electron in the expanding nanoplasma (Fig. 5.9 (c)), or even to another Rydberg state electron in a neighboring atom (Fig. 5.9 (d)). These processes are expected to take place on ps timescales. A distinct signature on the electron spectrum of the CED mechanism, as indicated in Ref. [165], is the peak structure below IP. When two electrons in Rydberg states are involved in the relaxation process, the emitted electron has an initial kinetic energy given by

$$E_{kin} = E_{IP} - E_{b,1} - E_{b,2}. \tag{5.31}$$

Here, $E_{IP}$ is the ionization potential of the cluster, $E_{b,1}$ is the binding energy of the electron who donates the energy by relaxing to the ground state and $E_{b,2}$ is the binding energy of the second electron who gains this energy. There are two kinds of CED processes. One involves two weakly bound Rydberg electrons, which will result in a structural peak with relatively higher kinetic energy indicated by 'Case 1' in Fig. 5.9 (e). The other case involves two deeply bound Rydberg electrons and will generate a peak at lower kinetic energy which is indicated by 'Case 2' in Fig. 5.9 (e). The electron kinetic energy spectra in our experiments show similar spectral signatures. For instance, there is spectral structure superimposed on a 'thermal' background , which is indicated by the dashed blue line in Fig. 5.8 for the resonance condition. However, we cannot distinguish the contributions from 'Case 1' and 'Case 2'. It is possible that the IP for silver clusters is too low such that the signals from the two cases overlap in kinetic energy and thus cannot be distinguished. The uniform angular distributions within this region in the VMI images (Fig. 5.7 (b-f)) mainly come from the 'thermal' background. However, due to the low signal statistics and non-uniformity of the detector efficiency, we do not have a reliable approach to subtract the thermal background at the moment. This problem needs to be solved. On the other hand, the characteristic spectral feature from CED can only be obtained within narrow experimental conditions [165]. First, a proper laser intensity is required to provide enough density of Rydberg atoms. Second, the distinct peaks broaden and red-shift in larger clusters since the nanoplasma environment holds for longer time, therefore will be hard to be observed. In addition to the CED process, processes such as three-body recombination (TBR) and interatomic Coulombic electron capture (ICEC) with ps time scales may play a role during the cluster expansion [166].

CEP-tagging was performed to measure the directional elecron emission at three time delays, i.e. 2, 6, and 11 ps. The resulting asymmetry maps for both background gases and for silver clusters are shown in Fig. 5.10. The plot in Fig. 5.10 (a) is obtained from gases. The asymmetry plots from gases for all the delays are identical thus only one is shown here. A laser intensity of about $2 \times 10^{13}$ W cm$^{-2}$ can be derived from the measurements. In

Fig. 5.10 (b-d), the asymmetry maps show delay-dependent directionality on the electron emission from silver clusters. Both the cutoff energy and phase offset as a function of delay can be distinguished from these plots.
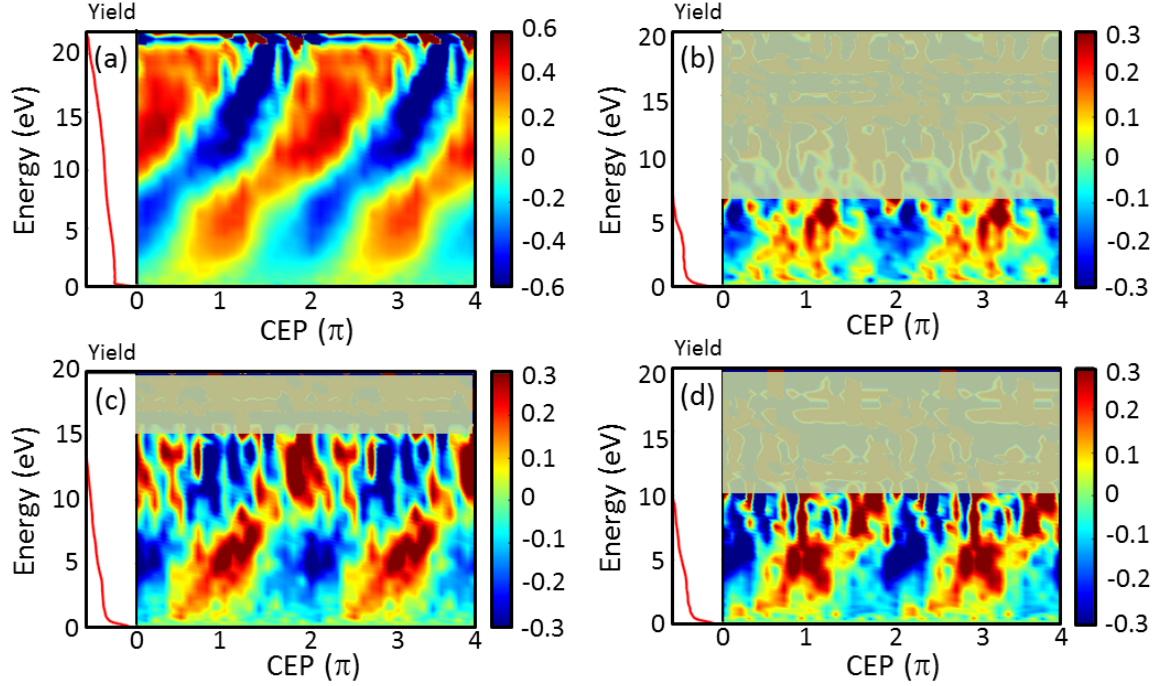


Figure 5.10: The asymmetry maps and the spectra for the electron emission from background gas (a) and from silver nanoclusters (b-d) for time delays at 2, 6, 11 ps, respectively.

For a better comparison of the phase offsets, the asymmetry parameters are integrated for a kinetic energy range from 3 to 5 eV for all the delays and are fitted with a cosine function. This energy range is dominated by electrons from direct ionization. The resulting phase offsets at the three delay times are plotted in Fig. 5.11. In the figure, the red data are obtained from background gases, which show almost no delay-dependence within the uncertainty range. The black data from silver clusters exhibit clear phase shifts as a function of time delay. Small phase shifts of about 0.1-0.3 radian can be obtained for the time delays investigated in this work, and the tendency is reproducible from day to day. This indicates that the electron emission from clusters may be influenced by the instantaneous local field, i.e. the electrons can be further boosted by the local field during the expanding of nanoplasma. The asymmetry map in Fig. 5.10 (b) shows similar behavior compared to the results from gas. A division at around 8 eV can be distinguished on the asymmetry map. It is likely that the electrons below 8 eV are from direct ionization, while those above 8 eV are from rescattering processes. These 'high' energy rescattered electrons from clusters are only observed in the resonance condition. On the other hand, the electron
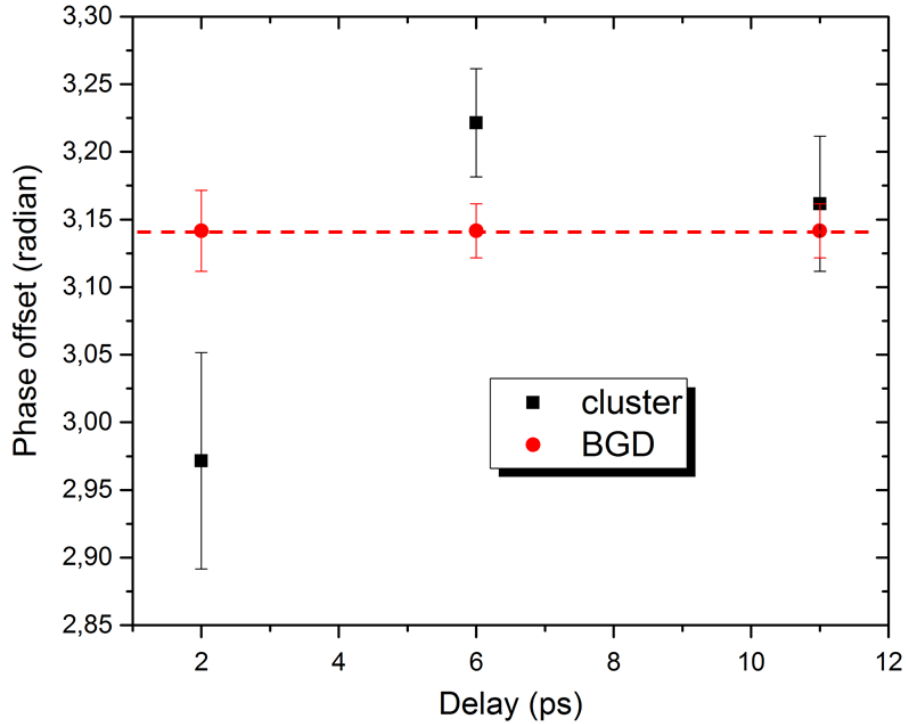
Figure 5.11: The delay-dependent phase offsets of the asymmetry oscillations for electrons in the energy range of 3-5 eV from clusters and from background (BGD) gases.

emission at low momentum corresponding to the strong signal close to zero momenta (with kinetic energy below 1 eV) does not show clear asymmetry oscillations. This agrees with our assumption that the signal may arise from thermal emission or single-photon outer ionization from the pulse pedestal or DC-field ionization.

An earlier work carried out by Passig *et al.* has explored the CEP-dependence of electron emission from silver clusters in dual few-cycle NIR laser fields at laser intensities on the order of $10^{14}$ W cm$^{-2}$ [167]. Electrons with high kinetic energies up to keV (corresponding to a cutoff energy above 100 $Up$) are observed utilizing a High-energy TOF spectrometer. The asymmetry of the high energy rescattering electrons exhibits clear phase offsets as a function of the delay between the pump and probe pulses. However, the signal at low kinetic energies is dominated by electron emission from background gases therefore cannot be compared with our data. At the moment there is no report on the theoretical calculations about the CEP-dependence of the electron emission from metal clusters within our parameter range. A theoretical model is required and further experiments need to be carried out for different parameters, such as laser intensities, cluster sizes, and delay times, to verify the underlying mechanisms for the electron emission.

# 5.3   Conclusions and outlook

To conclude, the angular-resolved momentum distributions of the electron emission from silver nanoclusters are studied in dual ultrashort laser fields at intensities on the order of $10^{13}$ W cm$^{-2}$. Transient nanoplasma resonance with the NIR field is observed in expanding silver nanoclusters at optimal delay time with higher electron yields. The resulting electron kinetic energy spectra from silver clusters exhibit a strong peak close to zero momenta and characteristic spectral features below IP. Compared to a recent work reported in expanding rare-gas clusters, the spectral feature below IP may have a contribution from CED processes which involve two Rydberg state electrons. Besides, the asymmetry parameter of the electrons show delay-dependent phase offsets for clusters, compared to a constant phase obtained from the signal for background gases. This indicates that the acceleration of electrons by the local field in an expanding nanoplasma can be steered by the CEP of few-cycle pulses.

This chapter shows a preliminary experimental study on the electronic dynamics in expanding silver nanoclusters under moderate intense laser fields. However, the interpretation of the presented results is insufficient. On one hand, a theory model which can deal with metal nanoclusters interacting with moderate intense few cycle laser pulses is required to verify the underlying mechanism observed in our experiment. On the other hand, systematical experimental investigations can help to understand the behavior under different conditions. For instance, an extension of experiments towards higher laser intensities will help to explore the onset of approaching the highly nonlinear regime. We can also study nanoclusters from other metallic and dielectric materials with various sizes or with different geometries, to find out the influences from material properties.

With attosecond probing, it is possible to trace the transient dynamics of clusters after excitation by an ultrashort pulse. One interesting aspect is the time evolution of the charging of ions during cluster expansion. An IR pump/XUV probe scheme was proposed to trace this dynamics [168]. After excited by an IR pulse, the inner potential of the cluster is changing during the expansion, corresponding to an evolution of charge states. An XUV photon can excite the bound electrons to the continuum by one-photon absorption, resulting in a high kinetic energy peak, which can be used to trace the instantaneous binding energy and thus the transient charging states of the cluster. We have tried with this experimental scheme in collaboration with the Calegari and Nisoli groups at Politecnico di Milano. Due to low count rate, no valuable results have been obtained yet. We expect this research work can be accomplished in the near future with the efforts to improve the target density as well as generating higher XUV photon flux.

# Bibliography

[1] A. H. Zewail, "Femtochemistry: Atomic-scale dynamics of the chemical bond," *J. Phys. Chem. A*, vol. 104, p. 5660, 2000.

[2] R. Martens, K. Varju, P. Johnsson, J. Mauritsson, Y. Mairesse, P. Salieres, M. Gaarde, K. Schafer, A. Persson, S. Svanberg, C. Wahlström, and A. Huillier, "Amplitude and phase control of attosecond light pulses," *Phys. Rev. Lett.*, vol. 94, p. 033001, 2005.

[3] A. Baltuska, T. Udem, M. Uiberacker, M. Hentschel, E. Goulielmakis, C. Gohle, R. Holzwarth, V. Yakovlev, A. Scrinzi, T. Hänsch, and F. Krausz, "Attosecond control of electronic processes by intense light fields," *Nature*, vol. 421, p. 611, 2003.

[4] K. Zhao, Q. Zhang, M. Chini, Y. Wu, X. Wang, and Z. Chang, "Tailoring a 67 attosecond pulse through advantageous phase-mismatch," *Optics Letters*, vol. 37, p. 3891, 2012.

[5] M. Kling, C. Siedschlag, A. Verhoef, J. Khan, M. Schultze, T. Uphues, Y. Ni, M. Uiberacker, M. Drescher, F. Krausz, and M. Vrakking, "Control of electron localization in molecular dissociation," *Science*, vol. 312, p. 246, 2006.

[6] M. Kremer, B. Fischer, B. Feuerstein, V. L. de Jesus, V. Sharma, C. Hofrichter, A. Rudenko, U. Thumm, C. D. Schroeter, R. Moshammer, and J. Ullrich, "Electron localization in molecular fragmentation of $h_2$ by carrier-envelope phase stabilized laser pulses," *Phys. Rev. Lett.*, vol. 103, p. 213003, 2009.

[7] H. Xu, J.-P. Maclean, D. Laban, W. Wallace, D. Kielpinski, R. Sang, and I. Litvinyuk, "Carrier-envelope-phase-dependent dissociation of hydrogen," *New J. Phys.*, vol. 15, p. 023034, 2013.

[8] M. Kling, C. Siedschlag, I. Znakovskaya, A. Verhoef, S. Zherebtsov, F. Krausz, M. Lezius, and M. Vrakking, "Strong-field control of electron localisation during molecular dissociation," *Molecular Physics*, vol. 106, pp. 455–465, 2008.

[9] B. Fischer, M. Kremer, T. Pfeifer, B. Feuerstein, V. Sharma, U. Thumm, C. D. Schröter, R. Moshammer, and J. Ullrich, "Steering the electron in $h_2^+$ by nuclear wave packet dynamics," *Phys. Rev. Lett.*, vol. 105, p. 223001, 2010.

[10] I. Znakovskaya, P. von den Hoff, G. Marcus, S. Zherebstov, B. Bergues, X. Gu, Y. Deng, M. Vrakking, R. Kienberger, F. Krausz, R. de Vivie-Riedle, and M. Kling, "Subcycle controlled charge-directed reactivity with few-cycle midinfrared pulses," *Phys. Rev. Lett.*, vol. 108, p. 063002, 2012.

[11] T. Wittmann, B. Horvath, W. Helml, M. Schätzel, X. Gu, A. Cavalieri, G. Paulus, and R. Kienberger, "Single-shot carrierâenvelope phase measurement of few-cycle laser pulses," *Nature Physics*, vol. 5, p. 357, 2009.

[12] F. Süßmann, S. Zherebtsov, J. Plenge, N. G. Johnson, M. Kübel, A. Sayler, V. Mondes, C. Graf, E. Rühl, G. Paulus, D. Schmischke, P. Swrschek, and M. Kling, "Single-shot velocity-map imaging of attosecond light-field control at kilohertz rate," *Review of Scientific Instruments*, vol. 82, p. 093109, 2011.

[13] T. Rathje, N. G. Johnson, M. Möller, F. Süßmann, D. Adolph, M. Kübel, R. Kienberger, M. Kling, G. Paulus, and A. Sayler, "Review of attosecond resolved measurement and control via carrierâenvelope phase tagging with above-threshold ionization," *J. Phys. B: At. Mol. Opt. Phys.*, vol. 45, p. 074003, 2012.

[14] D. Ray, F. He, S. De, W. Cao, H. Mashiko, P. Ranitovic, K. Singh, I. Znakovskaya, U. Thumm, G. Paulus, M. Kling, I. Litvinyuk, and C. Cocke, "Ion-energy dependence of asymmetric dissociation of d2 by a two-color laser field," *Phys. Rev. Lett.*, vol. 103, p. 223201, 2009.

[15] H. Li, D. Ray, S. De, I. Znakovskaya, W. Cao, G. Laurent, Z. Wang, M. Kling, A. Le, and C. Cocke, "Orientation dependence of the ionization of co and no in an intense femtosecond two-color laser field," *Phys. Rev. A*, vol. 84, p. 043429, 2011.

[16] J. Wu, A. Vredenborg, L. Schmidt, T. Jahnke, A. Czasch, and R. Dörner, "Comparison of dissociative ionization of h2, n2, ar2, and co by elliptically polarized two-color pulses," *Phys. Rev. A*, vol. 87, p. 023406, 2013.

[17] P. Eckle, M. Smolarski, P. Schlup, J. Biegert, A. Staudte, M. Schöffler, H. G. Muller, R. Dörner, and U. Keller, "Attosecond angular streaking," *Nature Physics*, vol. 4, p. 565, 2008.

[18] J. Wu, M. Magrakvelidze, L. Schmidt, M. Kunitski, T. Pfeifer, M. Schöffler, M. Pitzer, M. Richter, S. Voss, H. Sann, H. Kim, J. Lower, T. Jahnke, A. Czasch, U. Thumm, and R. Dörner, "Understanding the role of phase in chemical bond breaking with coincidence angular streaking," *Nature Communications*, vol. 4, p. 2177, 2013.

[19] P. Corkum, "Plasma perspective on strong-field multiphoton ionization," *Phys. Rev. Lett.*, vol. 71, p. 1994, 1993.

[20] J. Krause, K. Schafer, and K. Kulander, "High-order harmonic generation from atoms and ions in the high intensity regime," *Phys. Rev. Lett.*, vol. 68, p. 3535, 1992.

[21] M. Lewenstein, P. Balcou, M. Ivanov, A. Huillier, and P. Corkum, "Theory of high-harmonic generation by low-frequency laser fields," *Phys. Rev. A*, vol. 49, p. 2117, 1994.

[22] L. Keldysh, "Ionization in the field of a strong electromagnetic wave," *Sov. Phys. JETP*, vol. 20, pp. 1945–1950, 1964.

[23] A. Le, H. Wei, C. Jin, and C. Lin, "Strong-field approximation and its extension for high-order harmonic generation with mid-infrared lasers," *J. Phys. B: At. Mol. Opt. Phys.*, vol. 49, p. 053001, 2016.

[24] X. Tong and S. Chu, "Time-dependent density-functional theory for strong-field multiphoton processes: Application to the study of the role of dynamical electron correlation in multiple high-order harmonic generation," *Phys. Rev. A*, vol. 57, p. 452, 1998.

[25] B. Zhang, J. Yuan, and Z. Zhao, "Dynamic core polarization in strong-field ionization of co molecules," *Phys. Rev. Lett.*, vol. 111, p. 163001, 2013.

[26] P. Li and S. Chu, "High-order-harmonic generation of ar atoms in intense ultrashort laser fields: An all-electron time-dependent density-functional approach including macroscopic propagation effects," *Phys. Rev. A*, vol. 88, p. 053415, 2013.

[27] P. Corkum and F. Krausz, "Attosecond science," *Nature Physics*, vol. 3, p. 381, 2007.

[28] F. Krausz and M. Ivanov, "Attosecond physics," *Rev. Mod. Phys.*, vol. 81, p. 163, 2009.

[29] L. Keldysh, "Ionization in the field of a strong electromagnetic wave," *Soviet Physics JETP*, vol. 20, p. 1307, 1965.

[30] F. Fabre, G. Petite, P. Agostini, and M. Clement, "Multiphoton above-threshold ionisation of xenon at 0.53 and 1.06 $\mu$m," *J. Phys. B: At. Mol. Opt. Phys.*, vol. 15, p. 1353, 1982.

[31] P. Agostini, F. Fabre, G. Mainfray, G. Petite, and N. Rahman, "Free-free transitions following six-photon ionization of xenon atoms," *Phys. Rev. Lett.*, vol. 42, p. 1127, 1979.

[32] S. Augst, D. Strickland, D. Meyerhofer, S. Chin, and J. Eberly, "Tunneling ionization of nobel gases in a high-intensity laser field," *Phys. Rev. Lett.*, vol. 63, p. 2212, 1989.

[33] S. Chin, F. Yergeau, and P. Lavigne, "Tunnel ionisation of xe in an ultra-intense $co_2$ laser field ($10^{14}$ w cm$^{-2}$) with multiple charge creation," *J. Phys. B: At. Mol. Phys.*, vol. 18, p. L213, 1985.

[34] D. Fittinghoff, P. Bolton, B. Chang, and K. Kulander, "Observation of nonsequential double ionization of helium with optical tunneling," *Phys. Rev. Lett.*, vol. 69, p. 2642, 1992.

[35] M. Ammosov, N. Delone, and V. Krainov, "Tunnel ionization of complex atoms and of atomic ions in an alternating electromagnetic field," *Sov. Phys. JETP*, vol. 64, p. 1191, 1986.

[36] X. Tong, Z. Zhao, and C. Lin, "Theory of molecular tunneling ionization," *Phys. Rev. A*, vol. 66, p. 033402, 2002.

[37] I. Ahmad, S. Trushin, Z. Major, C. Wandt, S. Klingebiel, T.-J. Wang, V. Pervak, A. Popp, M. Siebold, F. Krausz, and S. Karsch, "Frontend light source for short-pulse pumped opcpa system," *Appl. Phys. B*, vol. 97, pp. 529–536, 2009.

[38] F. Süßmann, "Attosecond dynamics of nano-localized fields probed by photoelectron spectroscopy," *PhD Thesis*, 2013.

[39] V. Pervak, C. Teisset, A. Sugita, S. Naumov, F. Krausz, and A. Apolonski, "High-dispersive mirrors for femtosecond lasers," *Optics Express*, vol. 16, p. 10220, 2008.

[40] M. Nisoli, S. Silvestri, and O. Svelto, "Generation of high energy 10 fs pulses by a new pulse compression technique," *Appl. Phys. Lett.*, vol. 68, p. 2793, 1996.

[41] R. Stolen and C. Lin, "Self-phase-modulation in silica optical fibers," *Phys. Rev. A*, vol. 17, p. 1448, 1978.

[42] R. Stolen and A. Ashkin, "Optical kerr effect in glass waveguide," *Appl. Phys. Lett.*, vol. 22, p. 294, 1973.

[43] T. Brabec and F. Krausz, "Nonlinear optical pulse propagation in the single-cycle regime," *Phys. Rev. Lett.*, vol. 78, p. 3282, 1997.

[44] V. Pervak, I. Ahmad, M. Trubetskov, A. Tikhonravov, and F. Krausz, "Double-angle multilayer mirrors with smooth dispersion characteristics," *Optics Experss*, vol. 17, p. 7943, 2009.

[45] A. Wirth, M. Hassan, I. Grgura, J. Gagnon, A. Moulet, T. Luu, S. Pabst, R. Santra, Z. Alahmed, A. Azzeer, V. Yakovlev, V. Pervak, F. Krausz, and E. Goulielmakis, "Synthesized light transients," *Science*, vol. 334, p. 195, 2011.

[46] N. G. Johnson, O. Herrwerth, A. Wirth, S. De, I. Ben-Itzhak, M. Lezius, B. Bergues, M. Kling, A. Senftleben, C. Schröter, R. Moshammer, J. Ullrich, K. Betsch, R. Jones, A. Sayler, T. Rathje, K. Rühle, W. Müller, and G. Paulus, "Single-shot carrier-envelope-phase-tagged ion-momentum imaging of nonsequential double ionization of argon in intense 4-fs laser fields," *Phys. Rev. A*, vol. 83, p. 013412, 2011.

[47] D. W. Chandler and P. L. Houston, "Twoâdimensional imaging of stateâselected photodissociation products detected by multiphoton ionization," *J. Chem. Phys.*, vol. 87, p. 1445, 1987.

[48] A. T. Eppink and D. H. Parker, "Velocity map imaging of ions and electrons using electrostatic lenses: Application in photoelectron and photofragment ion imaging of molecular oxygen," *Review of Scientific Instruments*, vol. 68, p. 3477, 1997.

[49] O. Ghafur, W. Siu, P. Johnsson, M. Kling, M. Drescher, and M. Vrakking, "A velocity map imaging detector with an integrated gas injection system," *Review of Scientific Instruments*, vol. 80, p. 033110, 2009.

[50] M. J. Vrakking, "An iterative procedure for the inversion of two-dimensional ion/photoelectron imaging experiments," *Review of Scientific Instruments*, vol. 72, p. 4084, 2001.

[51] G. Paulus, F. Grasbon, H. Walther, P. Villoresi, M. Nisoli, S. Stagira, E. Priori, and S. De Silvestri, "Absolute-phase phenomena in photoionization with few-cycle laser pulses," *Nature*, vol. 414, p. 182, 2001.

[52] F. Lindner, G. Paulus, H. Walther, A. Baltuka, E. Goulielmakis, M. Lezius, and F. Krausz, "Gouy phase shift for few-cycle laser pulses," *Phys. Rev. Lett.*, vol. 92, p. 113001, 2004.

[53] G. Paulus, W. Nicklich, H. Xu, P. Lambropoulos, and H. Walther, "Plateau in above threshold ionization spectra," *Phys. Rev. Lett.*, vol. 72, p. 2851, 1994.

[54] H. Li, A. Alnaser, X. Tong, K. Betsch, M. Kübel, T. Pischke, B. Förg, J. Schötz, F. Süßmann, S. Zherebtsov, B. Bergues, A. Kessel, S. Trushin, A. Azzeer, and M. Kling, "Intensity dependence of the attosecond control of the dissociative ionization of d2," *J. Phys. B: At. Mol. Opt. Phys.*, vol. 47, p. 124020, 2014.

[55] H. Li, B. Mignolet, G. Wachter, S. Skruszewicz, S. Zherebtsov, F. Süßmann, A. Kessel, S. Trushin, N. G. Kling, M. Kübel, B. Ahn, D. Kim, I. Ben-Itzhak, C. Cocke, T. Fennel, J. Tiggesbäumker, K.-H. Meiwes-Broer, C. Lemell, J. Burgdörfer, R. Levine, F. Remacle, and M. Kling, "Coherent electronic wave packet motion in c60 controlled by the waveform and polarization of few-cycle laser fields," *Phys. Rev. Lett.*, vol. 114, p. 123004, 2015.

[56] I. Znakovskaya, P. von den Hoff, N. Schirmel, G. Urbasch, S. Zherebtsov, B. Bergues, R. de Vivie-Riedle, K.-M. Weitzel, and M. Kling, "Waveform control of orientation-dependent ionization of dcl in few-cycle laser fields," *Phys. Chem. Chem. Phys.*, vol. 13, p. 8653, 2011.

[57] S. Zherebtsov, T. Fennel, J. Plenge, E. Antonsson, I. Znakovskaya, A. Wirth, O. Herrwerth, F. Süßmann, C. Peltz, I. Ahmad, S. A. Trushin, V. Pervak, S. Karsch,

M. J. Vrakking, B. Langer, C. Graf, M. I. Stockman, F. Krausz, E. Rühl, and M. F. Kling, "Controlled near-field enhanced electron acceleration from dielectric nanospheres with intense few-cycle laser fields," *Nature Physics*, vol. 7, p. 656, 2011.

[58] S. Zherebtsov, F. Süßmann, C. Peltz, J. Plenge, K. Betsch, I. Znakovskaya, A. Alnaser, N. Johnson, M. Kübel, A. Horn, V. Mondes, C. Graf, S. Trushin, A. Azzeer, M. Vrakking, G. Paulus, F. Krausz, E. Rühl, T. Fennel, and M. Kling, "Carrierâenvelope phase-tagged imaging of the controlled electron acceleration from sio2 nanospheres in intense few-cycle laser fields," *New Journal of Physics*, vol. 14, p. 075010, 2012.

[59] F. Süßmann, L. Seiffert, S. Zherebtsov, V. Mondes, J. Stierle, M. Arbeiter, J. Plenge, P. Rupp, C. Peltz, A. Kessel, S. Trushin, B. Ahn, D. Kim, C. Graf, E. Rühl, M. Kling, and T. Fennel, "Field propagation-induced directionality of carrier-envelope phase-controlled photoemission from nanospheres," *Nature Communications*, vol. 6, p. 7944, 2015.

[60] J. Abrefah, D. Olander, M. Balooch, and W. Siekhaus, "Vapor pressure of buckminsterfullerene," *Appl. Phys. Lett.*, vol. 60, p. 1313, 1992.

[61] H. Li, "Study on molecular photoionization in femtosecond laser field," *Master Thesis*, 2013.

[62] H. Hartmann, V. Popok, I. Barke, V. von Oeynhausen, and K.-H. Meiwes-Broer, "Design and capabilities of an experimental setup based on magnetron sputtering for formation and deposition of size-selected metal clusters on ultra-clean surfaces," *Review of Scientific Instruments*, vol. 83, p. 073304, 2012.

[63] J. Passig, K.-H. Meiwes-Broer, and J. Tiggesbäumker, "Collimation of metal nanoparticle beams using aerodynamic lenses," *Review of Scientific Instruments*, vol. 77, p. 093304, 2006.

[64] P. Liu, P. J. Ziemann, D. B. Kittelson, and P. H. McMurry, "Generating particle beams of controlled dimensions and divergence: I. theory of particle motion in aerodynamic lenses and nozzle expansions," *Aerosol Science and Technology*, vol. 22, p. 293, 1995.

[65] P. Liu, P. J. Ziemann, D. B. Kittelson, and P. H. McMurry, "Generating particle beams of controlled dimensions and divergence: Ii. experimental evaluation of particle motion in aerodynamic lenses and nozzle expansions," *Aerosol Science and Technology*, vol. 22, p. 314, 1995.

[66] X. Wang, F. E. Kruis, and P. H. McMurry, "Aerodynamic focusing of nanoparticles: I. guidelines for designing aerodynamic lenses for nanoparticles," *Aerosol Science and Technology*, vol. 39, p. 611, 2005.

[67] O. A. Research, *NC200U-B Operation and Maintenance.*

[68] K. J. L. Company, "Practical process tips," *Lesker Tech.*, vol. 7, p. 1, 2010.

[69] H. Haberland, M. Karrais, M. Mall, and Y. Thurner, "Thin films from energetic cluster impact: A feasibility study," *J. Vac. Sci. Technol. A*, vol. 10, p. 3266, 1992.

[70] H. Zeman, "Deflection of an ion beam in the twoâdimensional electrostatic quadrupole field," *Rev. Sci. Instrum.*, vol. 48, p. 1079, 1977.

[71] P. von den Hoff, I. Znakovskaya, M. Kling, and R. de Vivie-Riedle, "Attosecond control of the dissociative ionization via electron localization: a comparison between $d_2$ and co," *Chem. Phys.*, vol. 366, p. 139, 2009.

[72] I. Znakovskaya, P. von den Hoff, S. Zherebtsov, A. Wirth, O. Herrwerth, M. Vrakking, R. de Vivie-Riedle, and M. Kling, "Attosecond control of electron dynamics in carbon monoxide," *Phys. Rev. Lett.*, vol. 103, p. 103002, 2009.

[73] Y. Liu, X. Liu, Y. Deng, C. Wu, H. Jiang, and Q. Gong, "Selective steering of molecular multiple dissociative channels with strong few-cycle laser pulses," *Phys. Rev. Lett.*, vol. 106, p. 073004, 2011.

[74] K. Betsch, N. G. Johnson, B. Bergues, M. Kübel, O. Herrwerth, A. Senftleben, I. Ben-Itzhak, G. Paulus, R. Moshammer, J. Ullrich, M. Kling, and R. Jones, "Controlled directional ion emission from several fragmentation channels of co driven by a few-cycle laser field," *Phys. Rev. A*, vol. 86, p. 063403, 2012.

[75] X. Xie, K. Doblhoff-Dier, S. Roither, M. Schöffler, D. Kartashov, H. Xu, T. Rathje, G. Paulus, A. Baltuka, S. Gräfe, and M. Kitzler, "Attosecond-recollision-controlled selective fragmentation of polyatomic molecules," *Phys. Rev. Lett.*, vol. 109, p. 243001, 2012.

[76] A. Alnaser, M. Kübel, R. Siemering, B. Bergues, N. G. Kling, K. Betsch, Y. Deng, J. Schmidt, Z. Alahmed, A. Azzeer, J. Ullrich, I. Ben-Itzhzk, R. Moshammer, U. Kleineberg, F. Krausz, R. de Vivie-Riedle, and M. Kling, "Subfemtosecond steering of hydrocarbon deprotonation through superposition of vibrational modes," *Nature Communications*, vol. 5, p. 3800, 2014.

[77] H. Xu, T. Okino, and K. Yamanouchi, "Ultrafast hydrogen migration in allene in intense laser fields: Evidence of two-body coulomb explosion," *Chem. Phys. Lett.*, vol. 469, p. 255, 2009.

[78] H. Xu, T. Okino, and K. Yamanouchi, "Tracing ultrafast hydrogen migration in allene in intense laser fields by triple-ion coincidence momentum imaging," *J. Chem. Phys.*, vol. 131, p. 151102, 2009.

[79] H. Xu, T. Okino, T. Kudou, K. Yamanouchi, S. Roither, M. Kitzler, A. Baltuska, and S. Chin, "Effect of laser parameters on ultrafast hydrogen migration in methanol studied by coincidence momentum imaging," *J. Phys. Chem. A*, vol. 116, p. 2686, 2012.

[80] H. Xu, C. Marceau, K. Nakai, T. Okino, S.-L. Chin, and K. Yamanouchi, "Communication: Two stages of ultrafast hydrogen migration in methanol driven by intense laser fields," *J. Chem. Phys.*, vol. 133, p. 071103, 2010.

[81] H. Akagi, T. Otobe, A. Staudte, A. Shiner, F. Turner, R. Dörner, D. Villeneuve, and P. Corkum, "Laser tunnel ionization from multiple orbitals in hcl," *Science*, vol. 325, p. 1364, 2009.

[82] M. Kübel, R. Siemering, C. Burger, N. G. Kling, H. Li, A. Alnaser, B. Bergues, S. Zherebtsov, A. Azzeer, I. Ben-Itzhak, R. Moshammer, R. de Vivie-Riedle, and M. Kling, "Steering proton migration in hydrocarbons using intense few-cycle laser fields," *Phys. Rev. Lett.*, 2016 in press.

[83] M. Kübel, R. Siemering, C. Burger, N. G. Kling, H. Li, A. Alnaser, B. Bergues, S. Zherebtsov, A. Azzeer, I. Ben-Itzhak, R. Moshammer, R. de Vivie-Riedle, and M. Kling, "Simultaneous phase- and intensity-tagging of strong-fieled dynamics in hydrocarbons," *in preparation*.

[84] H. Li, N. G. Kling, B. Förg, J. Stierle, A. Kessel, S. A. Trushin, M. F. Kling, and S. Kaziannis, "Carrier-envelope phase dependence of the directional fragmentation and hydrogen migration in toluene in few-cycle laser fields," *Structural Dynamics*, vol. 3, p. 043206, 2016.

[85] N. G. Kling, K. Betsch, M. Zohrabi, S. Zeng, F. Anis, U. Ablikim, B. Jochim, Z. Wang, M. Kübel, M. Kling, K. Carnes, B. Esry, and I. Ben-Itzhak, "Carrier-envelope phase control over pathway interference in strong-field dissociation of $h_2^+$," *Phys. Rev. Lett.*, vol. 111, p. 163004, 2013.

[86] T. Rathje, A. Sayler, S. Zeng, P. Wustelt, H. Figger, B. Esry, and G. Paulus, "Coherent control at its most fundamental: Carrier-envelope-phase-dependent electron localization in photodissociation of a $h_2^+$ molecular ion beam target," *Phys. Rev. Lett.*, vol. 111, p. 093002, 2013.

[87] V. Roudnev, B. Esry, and I. Ben-Itzhak, "Controlling $hd^+$ and $h_2^+$ dissociation with the carrier-envelope phase difference of an intense ultrashort laser pulse," *Phys. Rev. Lett.*, vol. 93, p. 163601, 2004.

[88] X. Tong and C. Lin, "Dynamics of light-field control of molecular dissociation at the few-cycle limit," *Phys. Rev. Lett.*, vol. 98, p. 123002, 2007.

[89] Y.-J. Jin, X.-M. Tong, and N. Toshima, "Enhanced ionization of hydrogen molecular ions in an intense laser field via a multiphoton resonance," *Phys. Rev. A*, vol. 81, p. 013408, 2010.

[90] X. Tong, Z. Zhao, and C. Lin, "Correlation dynamics between electrons and ions in the fragmentation of d2 molecules by short laser pulses," *Phys. Rev. A*, vol. 68, p. 043412, 2003.

[91] X. Tong and C. Lin, "Empirical formula for static field ionization rates of atoms and molecules by lasers in the barrier-suppression regime," *J. Phys. B: At. Mol. Opt. Phys.*, vol. 38, p. 2593, 2005.

[92] P. Bucksbaum, A. Zavriyev, H. Muller, and D. Schumacher, "Softening of the $h_2^+$ molecular bond in intense laser fields," *Phys. Rev. Lett.*, vol. 64, p. 1883, 1990.

[93] T. Ergler, A. Rudenko, B. Feuerstein, K. Zrost, C. Schröter, R. Moshammer, and J. Ullrich, "Spatiotemporal imaging of ultrafast molecular motion: Collapse and revival of the $d_2^+$ nuclear wave packet," *Phys. Rev. Lett.*, vol. 97, p. 193001, 2006.

[94] A. Alnaser, X. Tong, T. Osipov, S. Voss, M. Maharjan, P. Ranitovic, B. Ulrich, B. Shan, Z. Chang, C. Lin, and C. Cocke, "Routes to control of $h_2$ coulomb explosion in few-cycle laser pulses," *Phys. Rev. Lett.*, vol. 93, p. 183202, 2004.

[95] V. Roudnev and B. Esry, "General theory of carrier-envelope phase effects," *Phys. Rev. Lett.*, vol. 99, p. 220406, 2007.

[96] X. Tong, P. Ranitovic, C. Hogle, M. Murnane, H. Kapteyn, and N. Toshima, "Theory and experiment on laser-enabled inner-valence auger decay of rare-gas atoms," *Phys. Rev. A*, vol. 84, p. 013405, 2011.

[97] X. Tong and C. Lin, "Carrier-envelope phase dependence of nonsequential double ionization of $h_2$ by few-cycle laser pulses," *J. Phys. B: At. Mol. Opt. Phys.*, vol. 40, p. 641, 2007.

[98] K. Sasaki, X. Tong, and N. Toshima, "Coulomb focusing effect on the space distribution of the rescattering electron wavepacket in the laserâatom interaction," *J. Phys. B: At. Mol. Opt. Phys.*, vol. 42, p. 165603, 2009.

[99] T. Ishikawa, X. Tong, and N. Toshima, "Double ionization of he in an intense laser field via a rescattering process," *Phys. Rev. A*, vol. 82, p. 033411, 2010.

[100] H. Abou-Rachid, T. Nguyen-Dang, and O. Atabek, "Dynamical quenching of laser-induced dissociations of heteronuclear diatomic molecules in intense infrared fields," *J. Chem. Phys.*, vol. 110, p. 4737, 1999.

[101] M. V. Korolkov and K.-M. Weitzel, "Laser pulse control of photofragmentation in $dcl^+$: The effect of carrier envelope phase," *Chemical Physics*, vol. 338, p. 1277, 2007.

[102] H. Li, X. Tong, N. Schirmel, G. Urbasch, K. Betsch, S. Zherebtsov, F. Süßmann, A. Kessel, S. Trushin, G. Paulus, K.-M. Weitzel, and M. Kling, "Intensity dependence of the dissociative ionization of dcl in few-cycle laser fields," *J. Phys. B: At. Mol. Opt. Phys.*, vol. 49, p. 015601, 2016.

[103] P. Natalis, P. Pennetreau, L. Longton, and J. Collin, "Ionisation energy values for the vibronic transitions from hcl $x_1$ $\sigma_+(\nu" = 0)$ to hcl$^+$ ionic states $x^2$ $\pi(\nu\hat{a} = o-13)$ $and$ $a^2$ $\sigma^+(\nu\hat{a} = o - 12)$, determined by photoelectron spectroscopy," *Journal of Electron Spectroscopy and Related Phenomena*, vol. 27, p. 267, 1982.

[104] P. Pennetreau, P. Natalis, L. Longton, and J. Collin, "Ionisation energy values for the vibronic transitions from dcl $x_1$ $\sigma_+(\nu" = 0)$ to dcl$^+$ $x^2$ $\pi(\nu\hat{a} = o - 18)$ $and$ $a^2$ $\sigma^+(\nu\hat{a} = o - 17)$ determined by photoelectron spectroscopy," *Journal of Electron Spectroscopy and Related Phenomena*, vol. 28, p. 295, 1983.

[105] X.-M. Tong and S.-I. Chu, "Density-functional theory with optimized effective potential and self-interaction correction for ground states and autoionizing resonances," *Phys. Rev. A*, vol. 55, p. 3406, 1997.

[106] X. Chu and S.-I. Chu, "Self-interaction-free time-dependent density-functional theory for molecular processes in strong fields: High-order harmonic generation of $h_2$ in intense laser fields," *Phys. Rev. A*, vol. 63, p. 023411, 2001.

[107] Y.-J. Jin, X.-M. Tong, and N. Toshima, "Anomalous alignment dependence of the third-order harmonic of $h_2^+$ ions in intense laser fields," *Phys. Rev. A*, vol. 86, p. 053418, 2012.

[108] M. Kübel, A. Alnaser, B. Bergues, T. Pischke, J. Schmidt, Y. Deng, C. Jendrzejewski, J. Ullrich, G. Paulus, A. Azzeer, U. Kleineberg, R. Moshammer, and M. Kling, "Strong-field control of the dissociative ionization of n2o with near-single-cycle pulses," *New J. Phys.*, vol. 16, p. 065017, 2014.

[109] B. Bergues, M. Kübel, N. G. Johnson, B. Fischer, N. Camus, K. Betsch, O. Herrwerth, A. Senftleben, A. Sayler, T. Rathje, T. Pfeifer, I. Ben-Itzhak, R. Jones, G. Paulus, F. Krausz, R. Moshammer, J. Ullrich, and M. Kling, "Attosecond tracing of correlated electron-emission in non-sequential double ionization," *Nature Communications*, vol. 3, p. 813, 2012.

[110] M. Kübel, N. G. Kling, K. Betsch, N. Camus, A. Kaldun, U. Kleineberg, I. Ben-Itzhak, R. Jones, G. Paulus, T. Pfeifer, J. Ullrich, R. Moshammer, M. Kling, and B. Bergues, "Nonsequential double ionization of n2 in a near-single-cycle laser pulse," *Phys. Rev. A*, vol. 88, p. 023418, 2013.

[111] K. Hoshina, Y. Furukawa, T. Okino, and K. Yamanouchi, "Efficient ejection of $h_3^+$ from hydrocarbon molecules induced by ultrashort intense laser fields," *J. Chem. Phys.*, vol. 129, p. 104302, 2008.

[112] T. Okino, A. Watanabe, H. Xu, and K. Yamanouchi, "Two-body coulomb explosion in methylacetylene in intense laser fields: double proton migration and proton/deuteron exchange," *Phys. Chem. Chem. Phys.*, vol. 14, p. 4230, 2012.

[113] T. Okino, A. Watanabe, H. Xu, and K. Yamanouchi, "Ultrafast hydrogen scrambling in methylacetylene and methyl-$d_3$-acetylene ions induced by intense laser fields," *Phys. Chem. Chem. Phys.*, vol. 14, p. 10640, 2012.

[114] J. Ullrich, R. Moshammer, R. Dörner, O. Jagutzki, V. Mergel, H. Schmidt-Böcking, and L. Spielberger, "Recoil-ion momentum spectroscopy," *J. Phys. B: At. Mol. Opt. Phys.*, vol. 30, p. 2917, 1997.

[115] R. Dörner, V. Mergel, O. Jagutzki, L. Spielberger, J. Ullrich, R. Moshammer, and H. Schmidt-Böcking, "Cold target recoil ion momentum spectroscopy: a 'momentum microscope' to view atomic collision dynamics," *Physics Reports*, vol. 330, p. 95, 2000.

[116] M. Rabrenovic, A. Brenton, and T. Ast, "A study of $[c_7h_8]^+$ and $[c_7h_8]^{2+}$ ions formed from different precursor molecules," *Org. Mass Spectrosc.*, vol. 18, p. 587, 1983.

[117] S. Kaziannis, N. Kotsina, and C. Kosmidis, "Interaction of toluene with two-color asymmetric laser fields: Controlling the directional emission of molecular hydrogen fragments," *J. Chem. Phys.*, vol. 141, p. 104319, 2014.

[118] P. Colosimo, G. Doumy, C. Glaga, J. Wheeler, C. Hauri, F. Catoire, J. Tate, R. Chirla, A. March, G. Paulus, H. Muller, P. Agostini, and L. Dimauro, "Scaling strong-field interactions towards the classical limit," *Nature Physics*, vol. 4, p. 386, 2008.

[119] J. Tate, T. Auguste, H. Muller, P. Salires, P. Agostini, and L. DiMauro, "Scaling of wave-packet dynamics in an intense midinfrared field," *Physical Review Letters*, vol. 98, p. 013901, 2007.

[120] F. Lepine, M. Y. Ivanov, and M. J. Vrakking, "Attosecond molecular dynamics: fact or friction?," *Nature Photonics*, vol. 8, p. 195, 2014.

[121] B. Mignolet, R. Levine, and F. Remacle, "Control of electronic dynamics visualized by angularly resolved photoelectron spectra: A dynamical simulation with an ir pump and xuv attosecond-pulse-train probe," *Phys. Rev. A*, vol. 89, p. 021403(R), 2014.

[122] K. Ohmori, "Wave-packet and coherent control dynamics," *Annu. Rev. Phys. Chem.*, vol. 60, p. 487, 2009.

[123] A. Ballard, K. Bonin, and J. Louderback, "Absolute measurement of the optical polarizability of $c_{60}$," *J. Chem. Phys.*, vol. 113, p. 5732, 2000.

[124] Y. Huismans, E. Cormier, C. Cauchy, P.-A. Hervieux, G. Gademann, A. Gijsbertsen, O. Ghafur, P. Johnsson, P. Logman, T. Barillot, C. Bordas, F. Lpine, and M. Vrakking, "Macro-atom versus many-electron effects in ultrafast ionization of $c_{60}$," *Phys. Rev. A*, vol. 88, p. 013201, 2013.

[125] B. Mignolet, J. O. Johansson, E. E. Campbell, and F. Remacle, "Probing rapidly-ionizing super-atom molecular orbitals in $c_{60}$: A computational and femtosecond photoelectron spectroscopy study," *Chem. Phys. Chem.*, vol. 14, p. 3332, 2013.

[126] R. Völpel, G. Hofmann, M. Steidl, M. Stenke, M. Schlapp, R. Trassl, and E. Salzborn, "Ionization and fragmentation of fullerene ions by electron impact," *Phys. Rev. Lett.*, vol. 71, p. 3439, 1993.

[127] M. Boyle, T. Laarmann, K. Hoffmann, M. Heden, E. Campbell, C. Schulz, and I. Hertel, "Excitation dynamics of rydberg states in $c_{60}$," *Eur. Phys. J. D*, vol. 36, p. 339, 2005.

[128] M. Feng, J. Zhao, and H. Petek, "Atomlike, hollow-core-bound molecular orbitals of $c_{60}$," *Science*, vol. 320, p. 359, 2008.

[129] J. O. Johansson, G. G. Henderson, F. Remacle, and E. E. Campbell, "Angular-resolved photoelectron spectroscopy of superatom orbitals of fullerenes," *Phys. Rev. Lett.*, vol. 108, p. 173401, 2012.

[130] M. Boyle, K. Hoffmann, C. Schulz, and I. Hertel, "Excitation of rydberg series in $c_{60}$," *Phys. Rev. Lett.*, vol. 87, p. 273401, 2001.

[131] E. Campbell, G. Ulmer, and I. Hertel, "Delayed ionization of $c_{60}$ and $c_{70}$," *Phys. Rev. Lett.*, vol. 67, p. 1986, 1991.

[132] J. Johansson, J. Fedor, M. Goto, M. Kjellberg, J. Stenfalk, G. Henderson, E. Campbell, and K. Hansen, "Anisotropic hot electron emission from fullerenes," *J. Chem. Phys.*, vol. 136, p. 164301, 2012.

[133] J. O. Johansson and E. E. Campbell, "Probing excited electronic states and ionisation mechanisms of fullerenes," *Chem. Soc. Rev.*, vol. 42, p. 5661, 2013.

[134] M. Tchaplyguine, K. Hoffmann, O. Duehr, H. Hohmann, G. Korn, H. Rottke, M. Wittmann, I. Hertel, and E. Campbell, "Ionization and fragmentation of $c_{60}$ with sub-50 fs laser pulses," *J. Chem. Phys.*, vol. 112, p. 2781, 2000.

[135] B. Mignolet, R. Levine, and F. Remacle, "Charge migration in the bifunctional penna cation induced and probed by ultrafast ionization: a dynamical study," *J. Phys. B: At. Mol. Opt. Phys.*, vol. 47, p. 124011, 2014.

[136] H. Feshbach *Ann. Phys.*, vol. 19, p. 287, 1962.

[137] R. Levine, "Quantum mechanics of molecular rate processes," 1969.

[138] T. Yanai, D. P. Tew, and N. C. Handy, "A new hybrid exchangeâcorrelation functional using the coulomb-attenuating method (cam-b3lyp)," *Chem. Phys. Lett.*, vol. 393, p. 51, 2004.

[139] G. Seabra, I. Kaplan, V. Zakrzewski, and J. Ortiz, "Electron propagator theory calculations of molecular photoionization cross sections: The first-row hydrides," *J. Chem. Phys.*, vol. 121, p. 4143, 2004.

[140] B. Mignolet, R. Levine, and F. Remacle, "Localized electron dynamics in attosecond-pulse-excited molecular systems: Probing the time-dependent electron density by sudden photoionization," *Phys. Rev. A*, vol. 86, p. 053429, 2012.

[141] G. Wachter, C. Lemell, and J. Burgdöfer, "Electron rescattering at metal nanotips induced by ultrashort laser pulses," *Phys. Rev. B*, vol. 86, p. 035402, 2012.

[142] N. Delone and V. Krainov, "Multiphoton processes in atoms," *Springer*, 1994.

[143] F. Salvat, A. Jablonski, and C. J. Powell, "Dirac partial-wave calculation of elastic scattering of electrons and positrons by atoms, positive ions and molecules," *Computer Physics Communications*, vol. 165, p. 157, 2005.

[144] A. N. Pfeiffer, C. Cirelli, M. Smolarski, D. Dimitrovski, M. Abu-samha, L. B. Madsen, and U. Keller, "Attoclock reveals natural coordinates of the laser-induced tunnelling current flow in atoms," *Nature Physics*, vol. 8, p. 76, 2012.

[145] A. Pfeiffer, C. Cirelli, A. Landsman, M. Smolarski, D. Dimitrovski, L. Madsen, and U. Keller, "Probing the longitudinal momentum spread of the electron wave packet at the tunnel exit," *Phys. Rev. Lett.*, vol. 109, p. 083002, 2012.

[146] A. Bandrauk and H. Lu, "Controlling harmonic generation in molecules with intense laser and static magnetic fields: Orientation effects," *Phys. Rev. A*, vol. 68, p. 043408, 2003.

[147] M. Magrakvelidze, D. M. Anstine, G. Dixit, M. E.-A. Madjet, and H. S. Chakraborty, "Attosecond structures from the molecular cavity in fullerene photoemission time delay," *Phys. Rev. A*, vol. 91, p. 053407, 2015.

[148] A. Zewail and J. Thomas, "4d electron microscopy: Imaging in space and time," *Imperial College Press*, 2010.

[149] H. Chapman, "X-ray imaging beyond the limits," *Nat. Mater.*, vol. 8, p. 299, 2009.

[150] M. Chergui and A. Zewail, "Electron and x-ray methods of ultrafast structural dynamics: advances and applications," *Chem. Phys. Chem.*, vol. 10, p. 28, 2009.

[151] C. I. Blaga, J. Xu, A. D. Dichiara, E. Sistrunk, K. Zhang, P. Agostini, T. A. Miller, L. F. DiMauro, and C. Lin, "Imaging ultrafast molecular dynamics with laser-induced electron diffraction," *Nature*, vol. 483, p. 194, 2012.

[152] J. Xu, C. I. Blaga, A. D. DiChiara, E. Sistrunk, K. Zhang, Z. Chen, A.-T. Le, T. Morishita, C. Lin, P. Agostini, and L. F. Dimauro, "Laser-induced electron diffraction for probing rare gas atoms," *Phys. Rev. Lett.*, vol. 109, p. 233002, 2012.

[153] J. Xu, C. I. Blaga, K. Zhang, Y. Lai, C. Lin, T. A. Miller, P. Agostini, and L. F. DiMauro, "Diffraction using laser-driven broadband electron wave packets," *Nature Communications*, vol. 5, p. 4635, 2014.

[154] T. Fennel, K.-H. Meiwes-Broer, and J. Tiggesbäumker, "Laser-driven nonlinear cluster dynamics," *Rev. Mod. Phys.*, vol. 82, p. 1793, 2010.

[155] T. Zuo and A. Bandrauk, "Charge-resonance-enhanced ionization of diatomic molecular ions by intense lasers," *Phys. Rev. A*, vol. 52, p. R2511, 1995.

[156] I. Last and J. Jortner, "Quasiresonance ionization of large multicharged clusters in a strong laser field," *Phys. Rev. A*, vol. 60, p. 2215, 1999.

[157] T. Fennel, T. Döppner, J. Passig, C. Schaal, J. Tiggesbäumker, and K.-H. Meiwes-Broer, "Plasmon-enhanced electron acceleration in intense laser metal-cluster interactions," *Phys. Rev. Lett.*, vol. 98, p. 143401, 2007.

[158] U. Saalmann and J.-M. Rost, "Ionization of clusters in intense laser pulses through collective electron dynamics," *Phys. Rev. Lett.*, vol. 91, p. 223401, 2003.

[159] T. Döppner, T. Fennel, T. Diederich, J. Tiggesbäumker, and K. Meiwes-Broer, "Controlling the coulomb explosion of silver clusters by femtosecond dual-pulse laser excitation," *Phys. Rev. Lett.*, vol. 94, p. 013401, 2005.

[160] V. Kumarappan, M. Krishnamurthy, and D. Mathur, "Asymmetric emission of high-energy electrons in the two-dimensional hydrodynamic expansion of large xenon clusters irradiated by intense laser fields," *Phys. Rev. A*, vol. 67, p. 043204, 2003.

[161] J. Passig, R. Irsig, N. Truong, T. Fennel, J. Tiggesbäumker, and K. Meiwes-Broer, "Nanoplasmonic electron acceleration in silver clusters studied by angular-resolved electron spectroscopy," *New J. Phys.*, vol. 14, p. 085020, 2012.

[162] J. Jackson, *Classical electrodynamics*. New York: Wiley, 1999.

[163] G. Mie, "Beiträge zur optik trüber medien, speziell kolloidaler metallösungen," *Annalen der Physik*, vol. 25, p. 377, 1908.

[164] H. Fröhlich and H. Pelzer, "Plasma oscillations and energy loss of charged particles in solids," *Proc. Phys. Soc.*, vol. A68, p. 525, 1955.

[165] B. Schütte, M. Arbeiter, T. Fennel, G. Jabbari, A. Kuleff, M. Vrakking, and A. Rouze, "Observation of correlated electronic decay in expanding clusters triggered by near-infrared fields," *Nature Communications*, vol. 6, p. 8596, 2015.

[166] K. Gokhberg and L. Cederbaum, "Environment assisted electron capture," *J. Phys. B: At. Mol. Opt. Phys.*, vol. 42, p. 231001, 2009.

[167] J. Passig, "Steuerung der elektronenemission aus silberclustern in intensiven, geformten laserfeldern," *PhD Thesis*, 2012.

[168] I. Georgescu, U. Saalmann, and J. Rost, "Attosecond resolved charging of ions in a rare-gas cluster," *Phys. Rev. Lett.*, vol. 99, p. 183002, 2007.

# Acknowledgements

It would be a right moment now to thank all the people who made me go through this long journey.

First and foremost, I would like to show my deepest gratitude to my supervisor, Prof. Matthias Kling, who has provided me with so much support and valuable guidance through my PhD years. I am greatly benefited from all the promising projects he assigned to me. And his consistent encouragement keep me move forward all the time. His vigorous academic insight enlightens me not only in the past years but also in my future career. I would also like to thank Prof. Ferenc Krausz for giving me the opportunity to finish my PhD projects within his group at MPQ and LMU.

I am so honored to be part of a great team. I want to thank all the Kling group members, Dr. Sergey Zherebtsov, Qingcao(Max) Liu, Johannes Stierle, Dr. Nora Kling, Johannes Schötz, Benjamin Förg, Christian Burger, Philipp Rupp, Harald Fuest, Dr. William Okell, Dr. Pawel Wnuk, Dr. Hirofumi Yanagisawa, as well as the former members Dr. Matthias Kübel and Dr. Frederik Süßmann. My special appreciation goes to Sergey, Max and Johannes Stierle. It was amazing experience working with you.

During these years, I was lucky to be involved in a lot of worldwide collaborations. I would like to thank Dr. Benoit Mignolet, Dr. Georg Wachter, Prof. Francoise Remacle, Prof. Joachim Burgdörfer for conducting the theoretical simulations on the $C_{60}$ project. The experimental part also greatly attributed to Dr. Sergy Zherebtsov and Dr. Slawomir Skruszewicz. For the cooperation on molecular projects, I would like to appreciate Dr. Ali Alnaser, Dr. Nora Kling, Dr. Spyros Kaziannis, Robert Siemering, Prof. Xiaoming Tong, and Prof. Regina de Vivie-Riedle. I also thank the Rostock group for sharing with us their rich knowledge and experiences on building and operating the nanocluster source. And I will never forget the summer spent in the Nisoli group at Politecnico de Milano with Dr. Francesca Calegari, Dr. Mattea Castrovilli, Dr. Erik Mansson and Mara Galli.

Without the support and help from the technicians, my work would have never been accomplished. I would like to thank Mr. Harald Haas, Mr. Anton Horn, Mr. Alois Böswald, Mr. Manuel Fischer and the MPQ workshop team. I would like to thank the technicians in the EDV department at MPQ and Mr. Felix Rauscher at LMU, who helped me deal

# Curriculum Vitae

**Personal Data**

| | |
|---|---|
| Name: | Hui Li |
| Date of birth: | April 10th, 1985 |
| Place of birth: | Tianjin, China |
| Citizenship: | China |

**Education**

| | |
|---|---|
| SINCE 2013 | PhD student, **Ludwig-Maximilians-Universität München** <br> PhD student at the International Max Planck Research School for Advanced Photon Science (IMPRS-APS), Germany <br> Advisor: Prof. Matthias KLING |
| 2010-2013 | Master of Science, **Kansas State University**, USA <br> Thesis: Study on Molecular Photoionization in Femtosecond Laser Field <br> Advisor: Prof. Lew COCKE and Prof. Matthias KLING |
| 2007-2010 | Master of Science, **Nankai University**, China <br> Thesis: Optical Modulation Properties in Different Liquid Crystal Systems <br> Advisor: Prof. Xinzheng ZHANG |
| 2003-2007 | Bachelor of Science, **Nankai University**, China <br> Thesis: Study on Coherent Properties of Weak Light |

**List of publications with relevance to the work presented in this thesis**

[1] M. Kübel, R. Siemering, C. Burger, N.G. Kling, <u>H. Li</u>, A.S. Alnaser, B. Bergues, S. Zherebtsov, A.M. Azzeer, I. Ben-Itzhak, R. Moshammer, R. de Vivie-Riedle, M. F. Kling, "Steering proton migration in hydrocarbons using intense few-cycle laser fields", *Phys. Rev. Lett.* **116**, 193001 (2016).

[2] <u>H. Li</u>, N.G. Kling, B. Förg, J. Stierle, A. Kessel, S.A. Trushin, M. F. Kling, "Carrier-envelope phase dependence of the directional fragmentation and hydrogen migration in toluene in few-cycle laser fields ", *Structural Dynamics* **3**, 043206 (2016).

[3] <u>H. Li</u>, X.M. Tong, N. Schirmel, G. Urbasch, K.J. Betsch, S. Zherebtsov, F. Süßmann, A. Kessel, S.A. Trushin, G.G. Paulus, K.-M. Weitzel, M. F. Kling, "Intensity dependence of the dissociative ionization of DCl in few-cycle laser fields ", *J. Phys. B: At. Mol. Opt. Phys.* **49**, 015601 (2016).

[4] <u>H. Li</u>, B. Mignolet, G. Wachter, S. Skruszewicz, S. Zherebtsov, F. Süßmann, A. Kessel, S.A. Trushin, N.G. Kling, M. Kübel, B. Ahn, D. Kim, I. Ben-Itzhak, C.L. Cocke, T. Fennel, J. Tiggesbäumker, K.-H. Meiwes-Broer, C. Lemell, J. Burgdörfer, R.D. Levine, F. Remacle, M. F. Kling, "Coherent Electronic Wave Packet Motion in $C_{60}$ Controlled by the Waveform and Polarization of Few-Cycle Laser Fields ", *Phys. Rev. Lett.* **114**, 123004 (2015).

[5] <u>H. Li</u>, A.S. Alnaser, X.M. Tong, K.J. Betsch, M. Kübel, T. Pischke, B. Förg, J. Schötz, F. Süßmann, S. Zherebtsov, B. Bergues, A. Kessel, S.A. Trushin, A.M. Azzeer, M. F. Kling, "Intensity dependence of the attosecond control of the dissociative ionization of $D_2$ ", *J. Phys. B: At. Mol. Opt. Phys.* **47**, 124020 (2014).

**Other publications**

[6] <u>H. Li</u>, B. Mignolet, Z. Wang, I. Ben-Itzhak, C.L. Cocke, F. Remacle, M.F. Kling "Transition of photoionization between SAMO and Rydberg states in $C_{60}$ ", *in preparation.*

[6] X. Ren, V. Makhija, <u>H. Li</u>, M. F. Kling, and V. Kumarappan, "Alignment-assisted field-free orientation of rotationally cold CO molecules", *Phys. Rev. A* **90**, 013419 (2014).

[7] N.G. Kling, D. Paul, A. Gura, G. Laurent, S. De, <u>H. Li</u>, Z. Wang, B. Ahn, C.H. Kim, T.K. Kim, I.V. Litvinyuk, C.L. Cocke, I. Ben-Itzhak, D. Kim and M. F. Kling,

"Thick-lens velocity-map imaging spectrometer with high resolution for high-energy charged particles", *JINST* **9**, P05005 (2014).

[**8**]  I. Znakovskaya, M. Spanner, S. De, <u>H. Li</u>, D. Ray, P. Corkum, I.V. Litvinyuk, C.L. Cocke and M. F. Kling, "Transition between Mechanisms of Laser-Induced Field-Free Molecular Orientation ", *Phys. Rev. Lett.* **112**, 113005 (2014).

| | |
|---|---|
| 2D | two-dimensional |
| 3D | three-dimensional |
| ADK | Ammosov-Delone-Krainov (tunneling ionization model) |
| APT | attosecond pulse train |
| ATD | above threshold dissociation |
| ATI | above threshold ionization |
| BS | bond-softening |
| CED | correlated electron decay |
| CEP | carrier envelope phase |
| CMOS | complementary metal-oxide semiconductor |
| COLTRIMS | COLd-Target Recoil-Ion-Momentum Spectroscopy |
| CREI | charge resonance enhanced ionization |
| DCS | differential cross section |
| DI | direct ionization |
| EI | enhanced ionization |
| EL | enzel lens |
| FABLES | fixed-angle broadband laser-driven electron scattering |
| FTL | Fourier transform limited |
| FWHM | full width at half maximum |
| GDD | group-delay dispersion |
| GS | ground state |
| HCF | hollow core fiber |
| HDM | high-dispersive mirror |
| HHG | high-order harmonic generation |
| HOMO | highest occupied molecular orbital |
| HPC | hybrid pulse compressor |
| HWP | half wave plate |
| ICEC | interatomic Coulombic electron capture |
| IP | ionization potential |
| LIED | laser-induced electron diffraction |
| MC | Monte Carlo |
| MCP | micro-channel plate |
| mIR | mid-infrared |
| MO-ADK | molecular-orbital Ammosov-Delone-Krainov model |
| NIR | near-infrared |
| NSDI | non-sequential double ionization |
| NWP | nuclear wave packet |
| PAP | parametric asymmetry plot |
| PES | potential energy surface |
| PFS | Petawatt-Field Synthesizer |
| QD | quantum dynamical |
| QMS | quadrupole mass spectrometer |
| QWP | quarter wave plate |
| RABBIT | reconstruction of attosecond beating by interference of two-photon transitions |
| RCE | recollisional excitation |
| REMI | reaction microscope |
| RI | refractive index |

| | |
|---|---|
| RIDI | rescattering induced double ionization |
| RISI | rescattering induced single ionization |
| SAE | single-active-electron |
| SAMO | super atomic molecular orbital |
| SAP | single attosecond pulse |
| SFA | strong-field approximation |
| SPARC | surface-plasmon-assisted rescattering in clusters |
| TBR | three-body recombination |
| TDDFT | time-dependent density functional theory |
| TDHF | time-dependent Hartree-Fock |
| TDSE | time-dependent Schrödinger equation |
| TOF | time of flight |
| TTL | transistor-transistor logic |
| VMI | velocity map imaging |
| XUV | extreme ultraviolet |

This thesis is dedicated to my family. To my dearest parents **Hongliang Li** and **Boli Sun** who have been continuous encouraging and supportive in my pursuit of academic life. To my beloved husband **Zhenhua Wang** and my daughter **Wendy (Jingwen) Wang** who gave me the most happiness in my life.